NASA
Technical
Paper
3047

December 1990

Effect of Location of Aft-Mounted Nacelles on Longitudinal Aerodynamic Characteristics of a High-Wing Transport Airplane

William K. Abeyounis
and James C. Patterson, Jr.

NASA

NASA Technical Paper 3047

1990

Effect of Location of Aft-Mounted Nacelles on Longitudinal Aerodynamic Characteristics of a High-Wing Transport Airplane

William K. Abeyounis
Langley Research Center
Hampton, Virginia

James C. Patterson, Jr.
Vigyan Research Associates, Inc.
Hampton, Virginia

NASA
National Aeronautics and Space Administration
Office of Management
Scientific and Technical Information Division

Summary

As part of a propulsion/airframe integration program at Langley Research Center, tests have been conducted in the Langley 16-Foot Transonic Tunnel to determine the longitudinal aerodynamic effects of installing flow-through, mixed-flow engine nacelles at several aft underwing positions on a high-wing transport airplane. Nacelles with D-shaped inlets were used in the tests. Some configurations with antishock bodies and with nacelle toe-in were also tested. Data were obtained for a free-stream Mach number range from 0.70 to 0.85 and for a model angle-of-attack range from −2.5° to 4.0°. Data were analyzed primarily at the design cruise conditions—a free-stream Mach number of 0.80 and a lift coefficient of 0.43 (at an angle of attack of approximately 1°).

Installation of nacelles in the aft underwing position produced lift increases, as opposed to the loss in lift typical of forward underwing pylon-mounted nacelle configurations. At the 0.370 semispan position, the more aft nacelle configuration had the lower installed drag increment. Along a spanwise line at a constant distance forward of the wing trailing edge, the 0.328 and 0.370 semispan nacelle positions generated the lowest installed drags; the installed drag of the 0.328 nacelle configuration was slightly lower. Toeing-in the nacelles at this position to better align with the local flow reduced the installed drag increment to a value below the calculated skin-friction drag of the isolated nacelle/pylon combinations (nacelle/pylons). The addition of antishock bodies to this toed-in configuration only increased the installed drag coefficient 0.0006, still 0.0003 below the calculated skin-friction drag of the isolated nacelle/pylons.

Introduction

The installation of engine nacelles on the wing, fuselage, or tail of an airplane has a decided effect on the aerodynamic performance of the airplane. The difficulties of reducing interference drag for conventional, forward, underwing pylon-mounted nacelles on supercritical wings have been shown (ref. 1). Consequently, a propulsion/airframe integration program for transport aircraft has been conducted at Langley Research Center (refs. 2 to 13). As part of this program, alternate nacelle arrangements with the potential for reducing unfavorable installation drag were explored. One of these is the aft underwing configuration. Reference 3 showed that, unlike the conventional, forward, underwing pylon-mounted nacelles, which cause a loss in lift characterized by a deficit in the wing span load, aft underwing nacelles generate a lift increase by pressurizing a portion of the lower wing surface. It also showed that antishock bodies, which could be configured as pylons to provide adequate structure for attaching the engine nacelles in an aft underwing position, could be added with little drag penalty.

To further study the aerodynamic effects of this unconventional nacelle installation, nacelles with D-shaped inlets (referred to herein and in ref. 3 as "D-nacelles") were tested in a wind-tunnel investigation. The D-nacelles were mounted at several spanwise and chordwise positions to ascertain if additional performance gains could be realized by increasing the pressurized area of the lower wing surface. Configurations with the antishock bodies of reference 3 and with nacelle toe-in were also tested.

Symbols and Abbreviations

A	cross-sectional area, in^2
A_0	capture area, in^2
BL	butt line of model (lateral dimension), in.
b	wing span, 63.121 in.
C_D	drag coefficient, $\frac{\text{Drag}}{q_\infty S}$
$C_{D,f,\text{nac}}$	isolated nacelle/pylon skin-friction drag coefficient
ΔC_D	nacelle installation drag coefficient
$\Delta C_{D,f}$	difference in skin-friction drag coefficient due to nacelle/pylon installation
C_L	lift coefficient, $\frac{\text{Lift}}{q_\infty S}$
℄	centerline
C_m	pitching-moment coefficient, $\frac{\text{Pitching moment}}{q_\infty S\bar{c}}$
C_p	pressure coefficient, $\frac{p-p_\infty}{q_\infty}$
c	chord measured in wing reference plane, in.
$\bar{c}$	mean geometric chord, $\frac{2}{3}\left(c_T + c_R - \frac{c_T c_R}{c_T + c_R}\right)$, in.
c_{av}	average wing chord, $\frac{c_R + c_T}{2}$, in.
c_R	reference root chord at model centerline, 12.639 in.
c_T	reference tip chord, 4.142 in.
D_{exit}	nacelle-exit diameter, 3.182 in.
FS	fuselage station (axial dimension from nose of model), in.

L	length, in.
L/D	lift-drag ratio
M_∞	free-stream Mach number
MHB	maximum half-breadth, in.
NBL	D-nacelle butt line (fig. 5(a)), in.
NS	nacelle station, in.
NWL	D-nacelle waterline (fig. 5(a)), WL + 7.0089, in.
p	pressure, lb/in^2
p_∞	free-stream static pressure, lb/in^2
q_∞	free-stream dynamic pressure, lb/in^2
R	D-nacelle radial distance from top (fig. 5(a)), in. (script R in ref. 3)
r_m	radius from model local centerline, in.
S	wing reference area, 529.59 in^2
SB	antishock body
WL	waterline of model (vertical dimension), in.
WRP	wing reference plane (WL 3.25), in.
x	local axial dimension, in.
y	local lateral dimension, in.
z	local vertical dimension, in.
α	angle of attack, deg
η	semispan location, $2y/b$
θ	circumferential angular dimension for D-nacelle (fig. 5(a)), deg
τ	nacelle forebody thickness, in.
ψ	circumferential angular dimension from vertical axis through nacelle centerline (fig. 5(a)), deg

Subscripts:

HL	highlight (start of inlet lip)
lip	inlet-forebody lip
max	maximum cross section

Experimental Apparatus and Procedure

Wind Tunnel

The experimental investigation was conducted in the Langley 16-Foot Transonic Tunnel (refs. 14 and 15). This facility is a single-return, continuous-flow, atmospheric wind tunnel. It has a 47-ft-long octagonal test section with eight longitudinal slots and a throat cross-sectional area of 199.15 ft^2. The tunnel has continuous air exchange for cooling. The wall divergence in the test section is adjusted as a function of the airstream dew point and Mach number to minimize any longitudinal static-pressure gradients in the test section. The free-stream Mach number is continuously variable to a maximum of 1.30 with an accuracy of ± 0.005. The average Reynolds number per foot varies from approximately 1.46×10^6 at a free-stream Mach number of 0.20 to approximately 4.10×10^6 at a free-stream Mach number of 1.30.

Model and Support System

General arrangement. The experimental apparatus used in this investigation is shown in figure 1. The 1/24-scale model was representative of a wide-body transport. The complete model was sting supported on a six-component strain-gauge balance. It had a high wing consisting of supercritical airfoil sections and a T-shaped tail (T-tail) described in reference 3. The T-tail was tested on only two baseline configurations during this investigation. The D-nacelles were tested in the aft underwing position at several chordwise and spanwise locations. A sketch showing the general arrangement of the basic transport model without nacelles is given in figure 2. The model blockage was only 0.36 percent of the test-section cross section; therefore, no corrections for tunnel blockage were needed.

Model support system. The transport model was sting mounted in the test section of the tunnel. The centerline of the model was aligned with the test-section centerline when the model was level. The moment center of the balance was at a fuselage station of 30.203 in. (FS 30.203). The model moment center was at FS 29.733 with the model nose located at tunnel station 129.99 ft.

Fuselage. The fuselage geometry is shown in figure 3. This fuselage was 62.0 in. in length with circular cross sections and a maximum diameter of 9.0 in. The model had an ellipsoidal nose, a cylindrical centerbody, and an upswept aft section. A cylindrical base fairing (fig. 1) was added to the fuselage to make test data less sensitive to base pressure corrections. The wall of the fairing was approximately 1/8 in. thick. The fairing was 5.50 in. high and 3.25 in. wide (fig. 3) and had four equally spaced, rearward-facing pressure orifices for measuring base pressure. Wing-fuselage fairings, described in reference 3, filled the gap between the fuselage and the wing lower surface.

Wing. The wing planform geometry is presented in figure 4. The wing reference plane was located 3.250 in. above the fuselage centerline. The wing was defined by specifying supercritical airfoil sections at three spanwise stations. The wing-tip leading edges were faired and rounded. A more complete wing description is presented in reference 3.

D-nacelle and pylon. The flow-through, long-duct, mixed-flow D-nacelle shown in figure 5(a) was tested. The nacelle was designed to have a mass flow ratio A_0/A_{HL} of 0.70 at the free-stream Mach number of 0.80. It had a maximum diameter of 4.500 in. and a length of 15.750 in. with smooth exterior and interior surfaces (continuous first and second derivatives in the axial direction). For the configuration shown in figure 5(a), the pylons originated at FS 30.5615, approximately at the wing crest. They had symmetric, elliptical cross sections and faired smoothly into the axisymmetric nacelle afterbodies. A more detailed description of the D-nacelles and pylons is presented in reference 3.

The D-nacelles were tested at several chordwise and spanwise locations (fig. 5(b)). These included the configuration presented in reference 3 with the nacelle centerline at $\eta = 0.370$ and the inlet face at FS 33.65 ($x/c = 0.714$). The nacelles were also tested 1 in. forward chordwise (FS 32.65, $x/c = 0.614$). Because the wing was thicker at this location, this configuration required additional fairing between the nacelle, pylon, and wing as shown in figure 5(c). The nacelles were also tested at FS 33.65 at the nominal semispan positions of $\eta = 0.328$ ($x/c = 0.736$) and $\eta = 0.255$ ($x/c = 0.768$). The change in wing shape at $\eta = 0.255$ resulted in a nacelle incidence of approximately 2° for that configuration. The nacelles were also tested with 2° toe-in at the $\eta = 0.328$ position.

Antishock bodies. The antishock bodies were tested only on the D-nacelles with 2° toe-in at $\eta = 0.328$ (fig. 6). The antishock bodies had semiconical forebodies and streamlined boattail afterbodies. The long-cone antishock bodies described in reference 3 were mounted on the pylons with the cone apexes at FS 31.2, approximately the wing maximum thickness location. They were also tested at a 1-in-forward location (FS 30.2) and at the 1-in-forward location with the afterbodies faired to the nacelle exits. All the bodies were tested at 0° cant angle. The antishock bodies were intended to be aerodynamic fairings for the structure required to install nacelles in this extreme aft position. The bodies were originally designed to relieve the shock formation on the wing upper surface and thus reduce the wave drag due to shock losses (ref. 16).

Instrumentation

The model aerodynamic force and moment data were obtained by an internally mounted, six-component strain-gauge balance (balance 838). Sting cavity and base pressures were measured by individual electrical strain-gauge transducers and were used to correct the cavity and base static pressures to the free-stream static pressure for force coefficients. The support-strut angle was measured by a helical potentiometer geared to the strut. Instruments were calibrated to an accuracy of at least ±0.5 percent of their maximum load. The drag-coefficient accuracy based on repeatability was approximately ±0.0003. The free-stream Mach number accuracy was ±0.005.

Tests

This experimental wind-tunnel investigation was conducted in the Langley 16-Foot Transonic Tunnel at free-stream Mach numbers from 0.70 to 0.85. The model angle of attack was varied from −2.5° to 4.0° at zero sideslip. The Reynolds number based on the mean geometric chord varied from approximately 2.5×10^6 to 3.0×10^6. Boundary-layer transition on the model was fixed by using a grit transition-strip procedure (ref. 17). Transition was fixed on the fuselage nose, wing, nacelles, vertical-tail bullet fairing, and horizontal and vertical tails as detailed in reference 3. Transition strips on the wing were applied in an aft location (fig. 7) to match the boundary-layer thickness at the trailing edge (ref. 18). Boundary-layer transition at the strips was verified by flow-visualization tests during the tunnel entry for reference 3. (See fig. 1 of ref. 3.) Because large pressure gradients in the fuselage cavity, found during the tunnel entry for reference 3, made base pressure corrections difficult, a cylindrical base fairing was added to make base pressure corrections simpler and more accurate. Except for two baseline runs, tests were conducted in this investigation with the T-tail removed, because it was difficult to accurately set the tail incidence angle to 0°. A second tunnel entry in this investigation was conducted to verify the large difference in ΔC_D for the configuration shown in figure 5(a) between this investigation and that of reference 3. (This difference was an indication of nacelle/tail interference.)

Data Reduction

All wind-tunnel parameters and model data were recorded simultaneously on magnetic tape. Averaged values were used to compute all parameters. The model angle of attack was computed by correcting the support-strut angle for sting deflections based on balance loads and for wind-tunnel upflow determined from inverted model runs in a previous wind-tunnel entry (ref. 2). Sting cavity and fuselage base pressures were used to correct the longitudinal balance components for pressure forces on the fuselage base and in the sting cavity. Force coefficients were standardly corrected to values that corresponded to free-stream static pressure acting on the base and sting cavity. This was done because model geometry modifications necessary to support the model caused unrealistic pressures in the base area. The nacelle internal drag corrections of reference 3 for the configuration shown in figure 5(a) were used for all configurations with nacelles. These corrections were computed by using nacelle internal static pressures to determine the mass flow for a one-dimensional flow calculation, and then by integrating the computed internal pressure and friction forces. Skin-friction drag was calculated by using the method of Frankl and Voishel (ref. 19). No corrections were made for model blockage since it was only 0.36 percent of the test-section cross section with the model level. Forces and moments were transferred to the model moment center, the quarter-chord point of the mean geometric chord on the model waterline (WL 0.0).

Presentation of Results

Results and Discussion

Basic Longitudinal Aerodynamic Data

The basic longitudinal aerodynamic data for the clean wing-body configuration, with and without the T-tail, and the various underwing aft-mounted D-nacelle configurations are presented in figures 8 to 17. All D-nacelle configurations were tested with the T-tail removed. Plots of lift coefficient versus angle of attack and plots of drag coefficient, pitching-moment coefficient, and lift-drag ratio versus lift coefficient are shown for free-stream Mach numbers from 0.70 to 0.85. Data are presented for the clean wing-body/tail configuration in figure 8, for the clean wing-body configuration in figure 9, for the configurations with D-nacelles in various chordwise and spanwise locations in figures 10 to 14, and for the configurations with antishock bodies in figures 15 to 17. The analysis of these data was made primarily at the design cruise conditions of $M_\infty = 0.80$ and $C_L = 0.43$ (at $\alpha \approx 1°$). To aid in the analysis, data were interpolated to account for small free-stream Mach number variations.

Aft-Mounted Nacelle Characteristics

As discussed in reference 3, installation of the D-nacelles resulted in an expected total drag increase throughout the angle-of-attack range as a result of the skin-friction drag and form drag associated with the additional nacelle wetted area. However, there was an almost constant lift increase throughout the angle-of-attack range that resulted from the favorable interference caused by the pressurization of the wing lower surface by the D-nacelles. This constant lift increase resulted in rotated drag polars for the D-nacelle configurations. A portion of this lift increase may also have been a result of the nacelle acting as an underwing fence, retarding the strong spanwise flow in the cusp region of the supercritical wing.

The pressurizing effect of the D-nacelles is evident in the chordwise pressure-coefficient distributions presented in figure 18 (extracted from ref. 3) for the D-nacelle configuration shown in figure 5(a). Wing chordwise distributions at span stations inboard, along the centerline, and outboard of the nacelles are presented. The pressurizing effect extended from the nacelle inlet at $x/c = 0.714$ forward to the wing leading edge. Just outboard of the nacelle, a large acceleration of the flow around the nacelle inlet lip is indicated (fig. 18(c)). This acceleration may be due to the large flow angles negotiated by the strong spanwise flow in the cusp of the supercritical wing lower surface.

The D-nacelle pylon on the wing upper surface caused a small lift loss that was indicated by the pressure-coefficient increase just aft of the wing upper surface shock wave (at $x/c \approx 0.45$ in fig. 18(c)). The primary purpose of this investigation was to test the D-nacelles at various spanwise and chordwise locations to ascertain whether additional performance gains could be realized by increasing the wing lower surface area pressurized by the D-nacelles.

Effect of Chordwise Location

The D-nacelles were tested at two chordwise locations in the $\eta = 0.370$ semispan plane ($x/c = 0.714$ and $x/c = 0.614$). The nacelle configuration with the inlet face at $x/c = 0.714$ (fig. 5(a)) was the same nacelle configuration tested in reference 3. However, a new base was added to the fuselage, and the T-tail was removed. The $x/c = 0.614$ configuration is shown in figure 5(c). The extra wing thickness at this location forced the D-nacelle and pylon farther apart vertically, and therefore required additional fairing.

The effect of the D-nacelle chordwise location is shown in figure 19. Both D-nacelle configurations had higher lift and drag than the wing-body configuration. The $x/c = 0.714$ configuration had a 0.05 higher lift coefficient over almost all the angle-of-attack range. This lift increase of the D-nacelle configurations resulted in rotated drag polars relative to that of the wing-body configuration. The polar of the $x/c = 0.614$ configuration crossed over the polar of the wing-body at $C_L = 0.825$ and over the polar of the $x/c = 0.714$ configuration at $C_L = 0.785$. The $x/c = 0.714$ configuration had a 0.0020 lower installation drag coefficient at cruise ($C_L = 0.43$) than did the $x/c = 0.614$ configuration. The $x/c = 0.714$ configuration had an installation drag coefficient of 0.0025. This was 0.0002 below the computed isolated nacelle/pylon skin-friction drag coefficient $C_{D,f,\text{nac}}$ of 0.0027 and only 0.0005 above $\Delta C_{D,f} = 0.0020$. ($\Delta C_{D,f}$ is less than $C_{D,f,\text{nac}}$ because the D-nacelle and pylon covered portions of the wing.) Both D-nacelle configurations had higher pitching-moment coefficients than the wing-body configuration; those for the $x/c = 0.614$ configuration were higher. The lift-drag ratios for both configurations were lower than those for the wing-body configuration (fig. 19(d)). The difference in L/D for the $x/c = 0.714$ configuration was approximately half that for the $x/c = 0.614$ configuration at cruise. It was concluded that moving the D-nacelles more aft increases the pressurized wing lower surface area, which improves the aerodynamic performance. However, the structural problem of mounting the nacelles may become more difficult.

Effect of Spanwise Location

The D-nacelles were tested at three semispan locations—$\eta = 0.370$, 0.328, and 0.255. The inlet faces for these configurations were all located at a constant distance forward of the wing trailing edge at FS 33.65. The change in wing twist and airfoil shape at $\eta = 0.255$ resulted in a nacelle incidence change of approximately 2°.

The effect of the D-nacelle spanwise location is shown in figure 20. All three configurations had lift-coefficient increases relative to that of the wing-body configuration, and the increments increased as the nacelles were moved inboard (fig. 20(a)). This may be the result of the pressurization of a larger wing lower surface area as the nacelles were moved inboard. The pitching-moment coefficient in general varied only 0.01 between the three configurations, and the coefficients decreased as the nacelles were moved inboard (fig. 20(c)). This was not surprising since the nacelle axial location was the same for all three configurations. While the lift increased as the nacelles were moved inboard, the C_D versus C_L plots (fig. 20(b)) and the L/D versus C_L plots (fig. 20(d)) show that the drag increased also. The installed drag coefficients for the $\eta = 0.370$ and $\eta = 0.328$ configurations were almost identical; however, the installed drag coefficient for the $\eta = 0.255$ configuration was about 0.0010 higher. While this difference may be partly caused by the nacelle incidence change for the $\eta = 0.255$ configuration, the increasing nacelle/fuselage interference drag as the nacelles were moved inboard nearer the fuselage was probably the biggest factor. The installed drag coefficient for the $\eta = 0.328$ configuration was the lowest at $\Delta C_D = 0.0024$. This value was 0.0003 below $C_{D,f,\text{nac}}$ and only 0.0004 above $\Delta C_{D,f}$.

Effect of Nacelle Toe-In

The D-nacelles were toed-in 2° in an effort to reduce the negative pressure-coefficient peak that occurred near the outboard inlet lip of the D-nacelles (fig. 18(c)) by better aligning the nacelles with the local flow. This peak reduced the increment in C_L caused by the D-nacelles. Since the $\eta = 0.328$ configuration had the best performance tested, the nacelles were toed-in at this location. The results are shown in figure 21. The lift coefficient was increased by 0.02 at the cruise angle of attack of 1°. The pitching-moment coefficient was essentially unchanged. The installed drag coefficient was reduced 0.0003 to $\Delta C_D = 0.0021$—this was 0.0006 below $C_{D,f,\mathrm{nac}}$ and only 0.0001 above $\Delta C_{D,f}$.

Antishock Bodies

Structurally, the installation of nacelles in an aft position is an extremely difficult task, since the forward attachment points would be located well behind the aft structural member of the wing. Pylons of sufficient size to provide adequate structural volume have an associated installation drag. This structural volume might be acquired with a minimum installed drag penalty by employing antishock bodies similar to those reported in reference 16.

Three antishock-body configurations were tested on the 2° toed-in D-nacelles at $\eta = 0.328$ (fig. 6). The long-cone antishock bodies of reference 3 were tested at the same axial location (FS 31.2). The antishock bodies were also tested at a location 1 in. forward (FS 30.2) and at the 1-in-forward location with the antishock bodies faired to the nacelle exits. The results are shown in figure 22. The performances of all the antishock-body configurations were about the same; the antishock bodies located at FS 30.2 performed slightly better. The antishock bodies cut the lift-coefficient increase of the D-nacelles from 0.10 to 0.05. The pitching-moment coefficients changed little. The installed drag coefficient at cruise ($C_L = 0.43$) increased by 0.0006 to $\Delta C_D = 0.0027$. This was still 0.003 below the isolated skin-friction drag coefficient of the nacelles, pylons, and antishock bodies of 0.0030.

Nacelle/Tail Interference

The configuration with the D-nacelles located at $x/c = 0.714$ and $\eta = 0.370$ and with the tail on in reference 3 was tested in this investigation with the tail off. The resulting installed drag coefficients were surprisingly different, 0.0043 for reference 3 and 0.0025 for the present investigation. There were differences between the configurations of the two wind-tunnel investigations. In addition to having the T-tail removed, the baseline wing-body and D-nacelle configurations of this investigation had a new fuselage base fairing for reasons cited previously. To determine whether the interference between the T-tail and the D-nacelles was really this large, a second wind-tunnel entry was conducted during this investigation. Four configurations were tested: the wing-body, the wing-body with D-nacelles, the wing-body with T-tail, and the wing-body with T-tail and D-nacelles. All configurations had the new base fairing. The basic longitudinal data for each configuration are presented in figures 23 to 26. A comparison of the drag coefficient versus lift coefficient for these configurations at $M_\infty = 0.80$ is shown in figure 27. At cruise ($C_L = 0.43$), $\Delta C_D = 0.0049$ for the configurations with the T-tail, and $\Delta C_D = 0.0033$ for the configurations with the T-tail removed. This indicates the nacelle/tail interference was 0.0016. This value might be unrealistically high for a real airplane configuration, since the wings and nacelles would probably be located more forward for weight and balance considerations. The nacelles also would probably be shorter. Therefore, the nacelles and tail would be farther apart and would probably have less interference.

The drag-coefficient differences at cruise ($C_L =$ 0.43) for the three configurations tested in both wind-tunnel entries were surprisingly large. It was 0.0008 for the wing-body configuration, 0.0014 for the wing-body with D-nacelles, and 0.0002 for the wing-body with T-tail. It was felt that the 0.0008 difference for the wing-body was understandable because of the added nacelle mounting holes in the wing and because of general model wear from wind-tunnel testing. The additional 0.0006 difference for the wing-body/D-nacelle configuration could be caused by wear on the nacelles and differences in nacelle alignment, since holes were elongated in order to toe-in the nacelles. The 0.0006 difference for the wing-body/T-tail configuration $(0.0008 - 0.0002)$ could be due to differences in mounting the T-tail and setting the incidence exactly the same for the two entries.

Conclusions

An investigation to determine the longitudinal aerodynamic effects of installing engine nacelles in aft underwing positions on a high-wing transonic transport airplane model has been conducted. Flow-through, mixed-flow nacelles with D-shaped inlets were tested over a free-stream Mach number range from 0.70 to 0.85 and an angle-of-attack range from −2.5° to 4.0°. A comparison of installed drag coefficients at cruise conditions (free-stream Mach number = 0.80; lift coefficient = 0.43) for the various configurations tested is presented in the following figure:

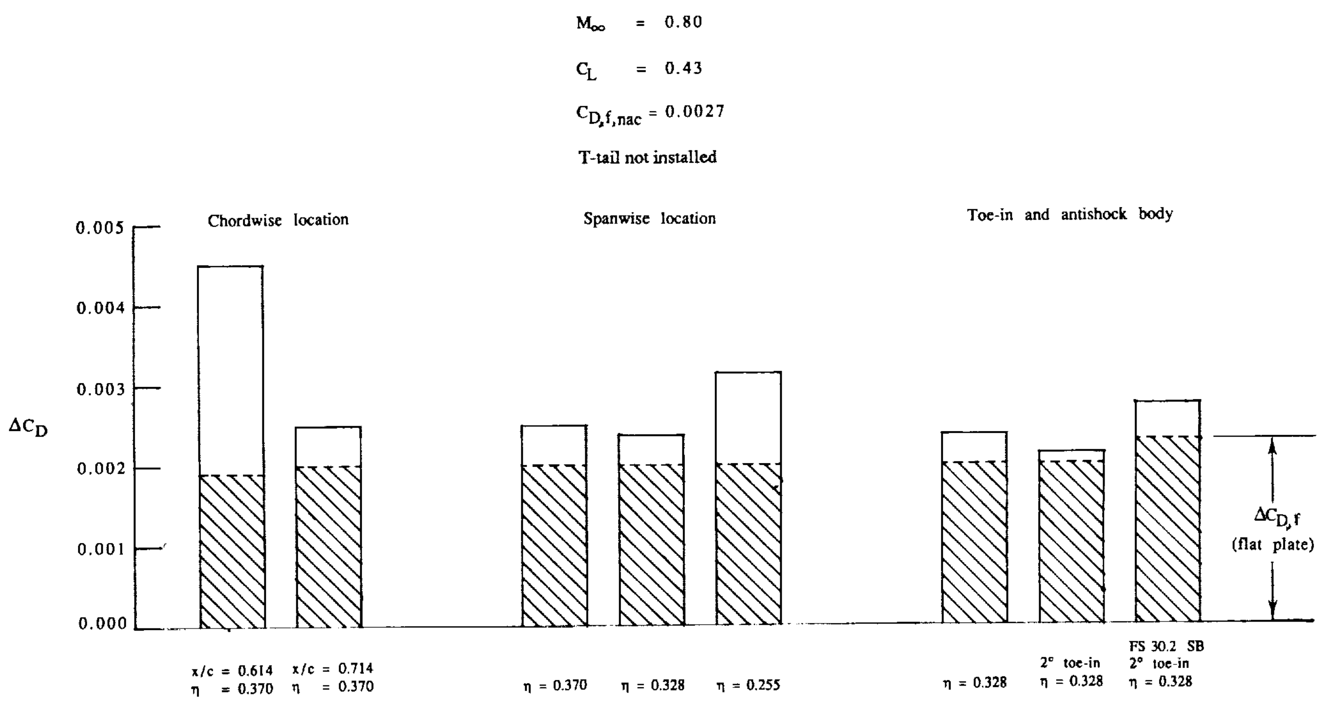

The following conclusions are presented:

1. At the 0.370 semispan location η, the configuration with the more aft nacelle position had the lesser installed drag coefficient.

2. Variation of the nacelle spanwise position revealed that the configuration with the $\eta = 0.328$ nacelle position, the middle nacelle position, was slightly more favorable in nacelle installation drag ΔC_D than the configuration with the nacelles at $\eta = 0.370$ because of the larger wing area affected. While the nacelles at the $\eta = 0.255$ position affected the largest wing area, the proximity of the nacelles and fuselage probably caused enough nacelle/fuselage interference drag to result in the largest ΔC_D.

3. Toeing-in the nacelles at the $\eta = 0.328$ position to better align the nacelles with the local flow resulted in the lowest value of ΔC_D, 0.0021, which is 0.0006 below the isolated skin friction of the D-nacelles and pylons and only 0.0001 above the difference in skin-friction drag coefficient due to nacelle/pylon installation.

4. The long-cone antishock body located with the apex at fuselage station 30.2 (at the local pressure-coefficient peak) had the lowest additional ΔC_D, 0.0006. This ΔC_D was still 0.0003 below the isolated skin-friction drag coefficient for this configuration.

5. The interference drag coefficient between the T-tail and D-nacelles was approximately 0.0016. This value would probably be much lower for configurations in which the nacelles and tail are more realistically farther apart for weight and balance considerations.

NASA Langley Research Center
Hampton, VA 23665-5225
October 5, 1990

References

1. Henderson, William P.; and Patterson, James C., Jr.: Propulsion Installation Characteristics for Turbofan Transports. AIAA-83-0087, Jan. 1983.
2. Lee, Edwin E., Jr.; and Pendergraft, Odis C., Jr.: *Installation Effects of Long-Duct Pylon-Mounted Nacelles on a Twin-Jet Transport Model With Swept Supercritical Wing.* NASA TP-2457, 1985.
3. Abeyounis, William K.; and Patterson, James C., Jr.: *Effect of Underwing Aft-Mounted Nacelles on the Longitudinal Aerodynamic Characteristics of a High-Wing Transport Airplane.* NASA TP-2447, 1985.
4. Lamb, Milton; Abeyounis, William K.; and Patterson, James C., Jr.: *Nacelle/Pylon/Wing Integration on a Transport Model With a Natural Laminar Flow Nacelle.* NASA TP-2439, 1985.
5. Henderson, William P.; and Abeyounis, William K.: *Aerodynamic Characteristics of a High-Wing Transport Configuration With an Over-the-Wing Nacelle-Pylon Arrangement.* NASA TP-2497, 1985.
6. Lamb, Milton; and Abeyounis, William K.: *Integration Effects of Underwing Forward- and Rearward-Mounted*

Separate-Flow, Flow-Through Nacelles on a High-Wing Transport. NASA TM-87627, 1986.

7. Lamb, Milton; Carlson, John R.; and Pendergraft, Odis C., Jr.: *Integration Effects of D-Shaped, Underwing, Aft-Mounted, Separate-Flow, Flow-Through Nacelles on a High-Wing Transport.* NASA TM-4018, 1987.
8. Carlson, John R.; and Lamb, Milton: *Integration Effects of Pylon Geometry on a High-Wing Transport Airplane.* NASA TP-2877, 1989.
9. Patterson, James C., Jr.; and Bartlett, Glynn R.: *Evaluation of Installed Performance of a Wing-Tip-Mounted Pusher Turboprop on a Semispan Wing.* NASA TP-2739, 1987.
10. Patterson, James C., Jr.: Wind-Tunnel Studies of Nacelle Interference Drag at High Subsonic Speeds Including the Effect of Powered Jets. *Conference on Aircraft Aerodynamics,* NASA SP-124, 1966, pp. 259–270.
11. Patterson, James C., Jr.: *A Wind-Tunnel Investigation of Jet-Wake Effect of a High-Bypass Engine on Wing-Nacelle Interference Drag of a Subsonic Transport.* NASA TN D-4693, 1968.
12. Patterson, James C., Jr.; and Flechner, Stuart G.: *An Exploratory Wind-Tunnel Investigation of the Wake Effect of a Panel Tip-Mounted Fan-Jet Engine on the Lift-Induced Vortex.* NASA TN D-5729, 1970.
13. Patterson, James C., Jr.; and Flechner, Stuart G.: *Jet-Wake Effect of a High-Bypass Engine on Wing-Nacelle Interference Drag of a Subsonic Transport Airplane.* NASA TN D-6067, 1970.
14. Corson, Blake W., Jr.; Runckel, Jack F.; and Igoe, William B.: *Calibration of the Langley 16-Foot Transonic Tunnel With Test Section Air Removal.* NASA TR R-423, 1974.
15. Peddrew, Kathryn H., compiler: *A User's Guide to the Langley 16-Foot Transonic Tunnel.* NASA TM-83186, 1981.
16. Whitcomb, Richard T.: *Special Bodies Added on a Wing To Reduce Shock-Induced Boundary-Layer Separation at High Subsonic Speeds.* NACA TN 4293, 1958.
17. Braslow, Albert L.; Hicks, Raymond M.; and Harris, Roy V., Jr.: *Use of Grit-Type Boundary-Layer-Transition Trips on Wind-Tunnel Models.* NASA TN D-3579, 1966.
18. Blackwell, James A., Jr.: *Preliminary Study of Effects of Reynolds Number and Boundary-Layer Transition Location on Shock-Induced Separation.* NASA TN D-5003, 1969.
19. Frankl, F.; and Voishel, V.: *Turbulent Friction in the Boundary Layer of a Flat Plate in a Two-Dimensional Compressible Flow at High Speeds.* NACA TM 1053, 1943.

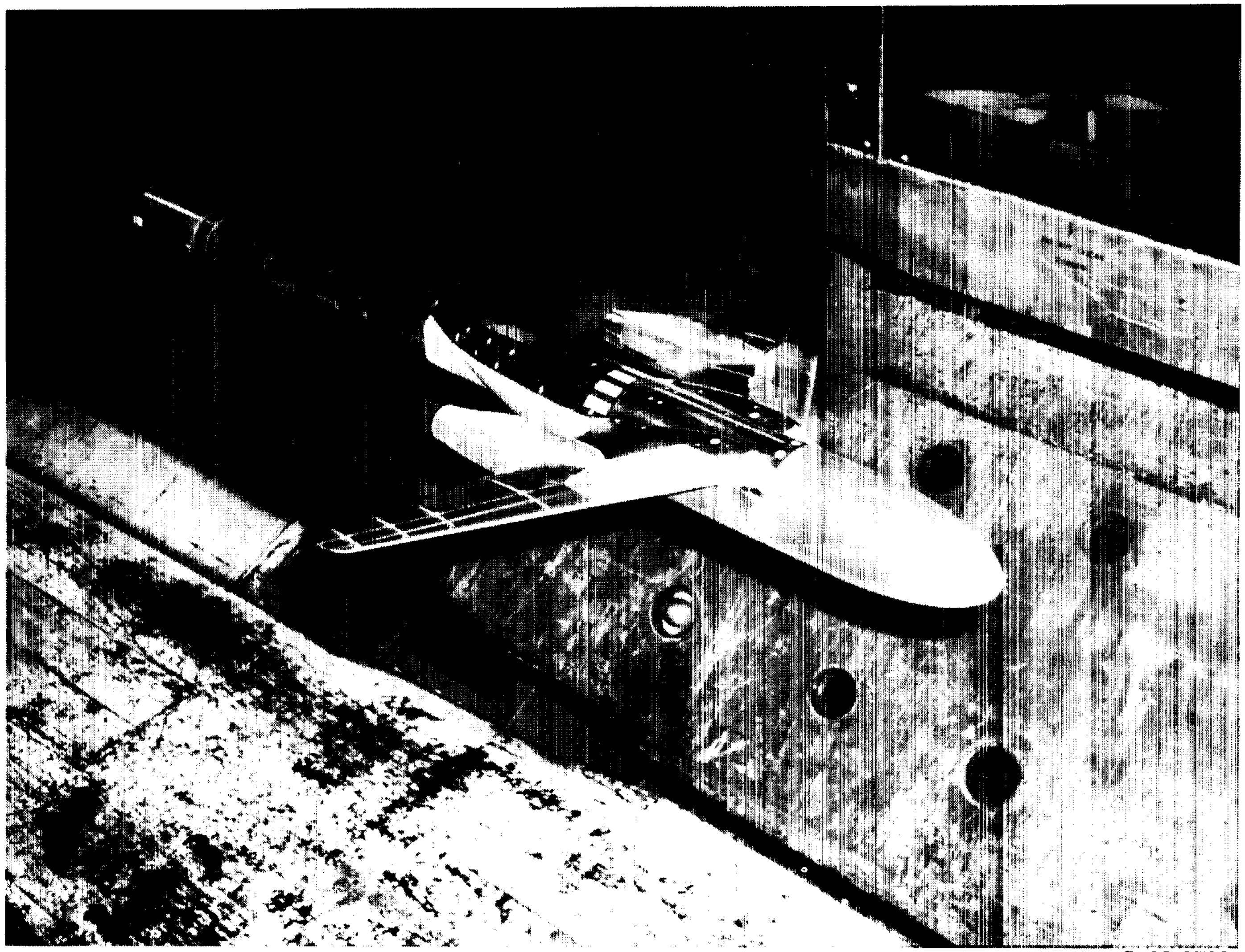

L-83-9702

Figure 1. Transonic transport airplane with aft-mounted D-nacelles and antishock bodies.

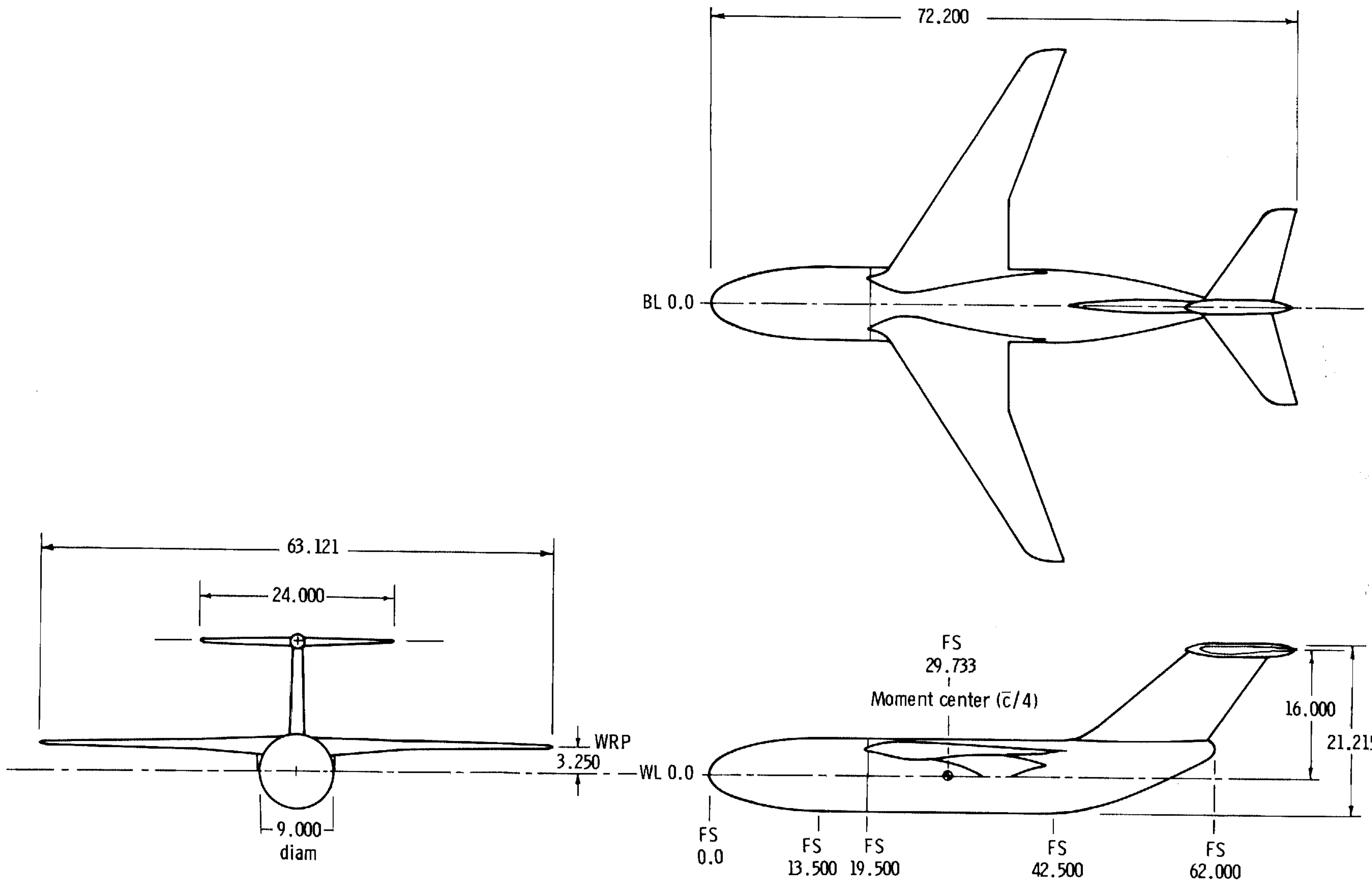

Figure 2. General arrangement of transport model. All dimensions are in inches.

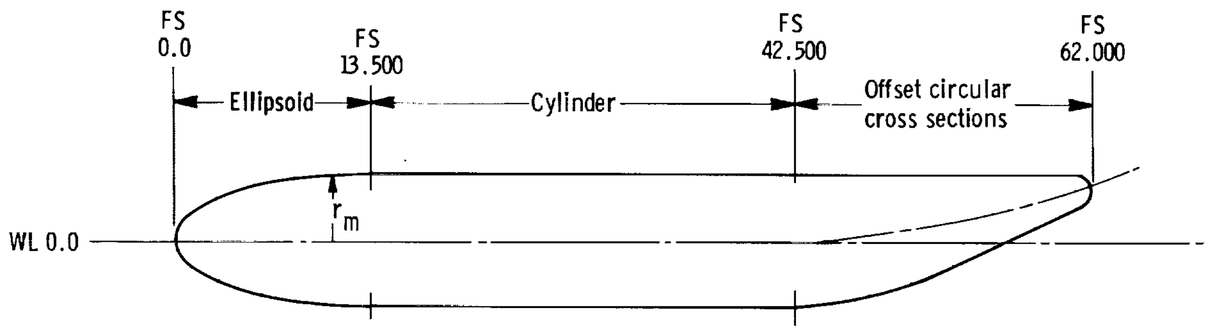

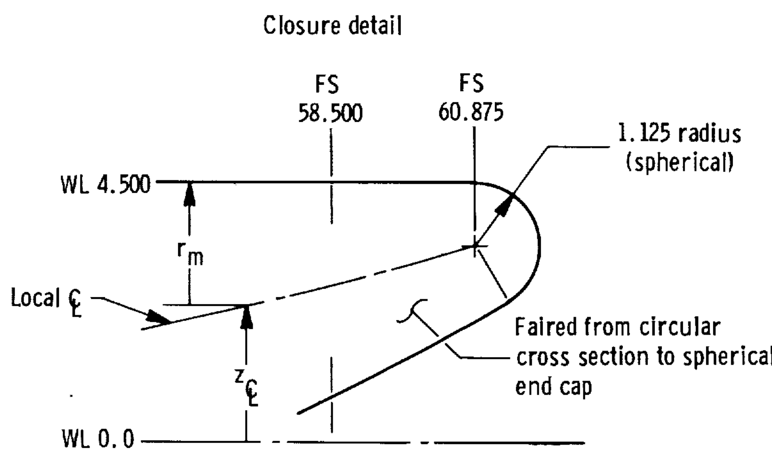

Ellipsoidal-nose coordinates	
FS	r_m
0	0
.100	.547
.200	.772
.250	.862
.375	1.053
.500	1.213
.750	1.479
1.000	1.700
1.250	1.891
1.500	2.062
2.000	2.357
2.500	2.609
3.500	3.023
4.500	3.354
5.500	3.625
6.500	3.848
7.500	4.031
9.500	4.298
11.500	4.450
13.500	4.500

Afterbody coordinates		
FS	$z_{℄}$	r_m
42.500	0	4.500
44.500	.100	4.400
46.500	.280	4.220
48.500	.550	3.950
50.500	.860	3.640
52.500	1.225	3.275
54.500	1.660	2.840
56.500	2.130	2.370
58.500	2.650	1.850
60.875	3.375	1.125

(a) General description.

Figure 3. Fuselage geometry. All dimensions are in inches.

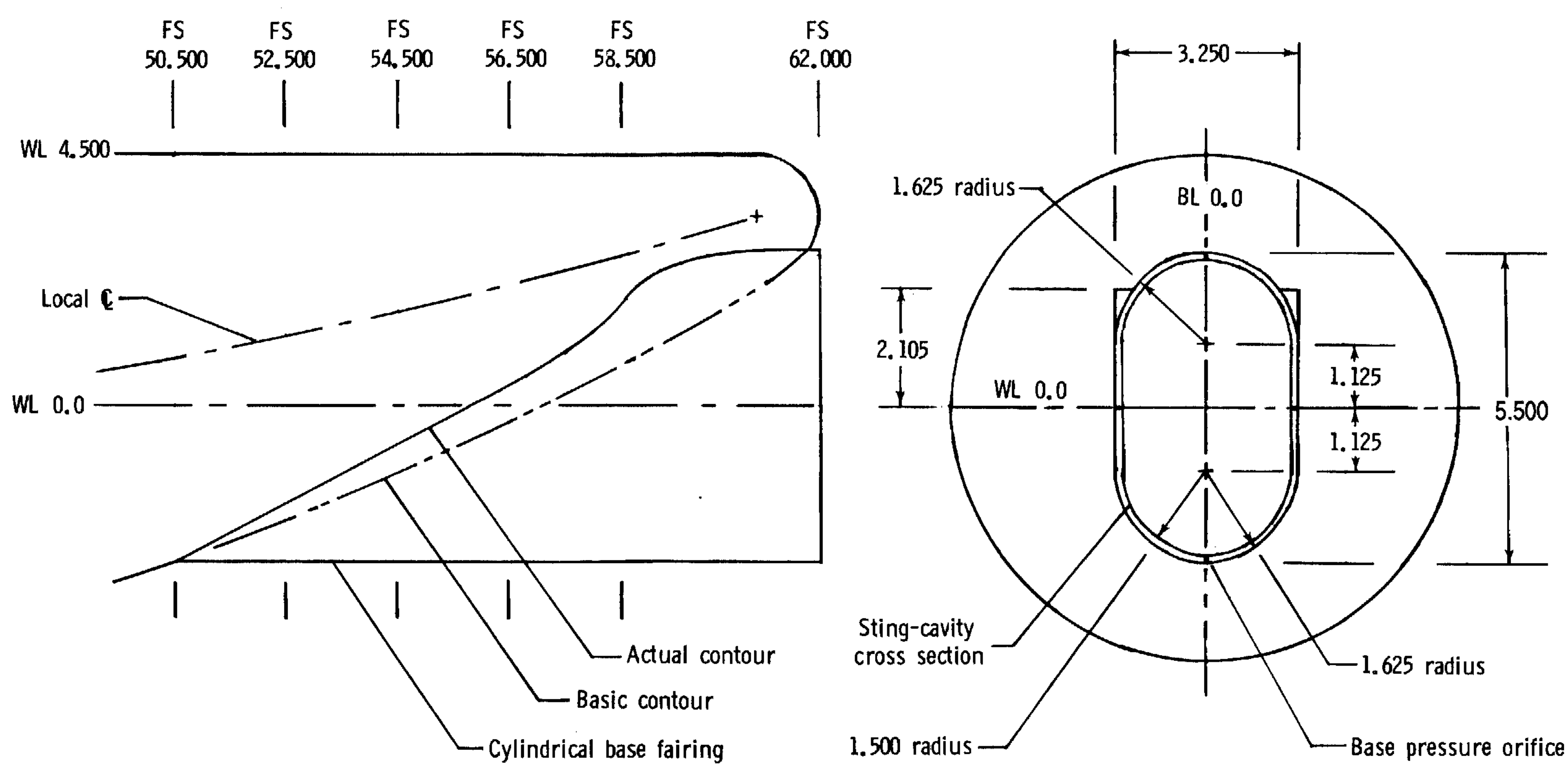

(b) Sting-cavity detail.

Figure 3. Concluded.

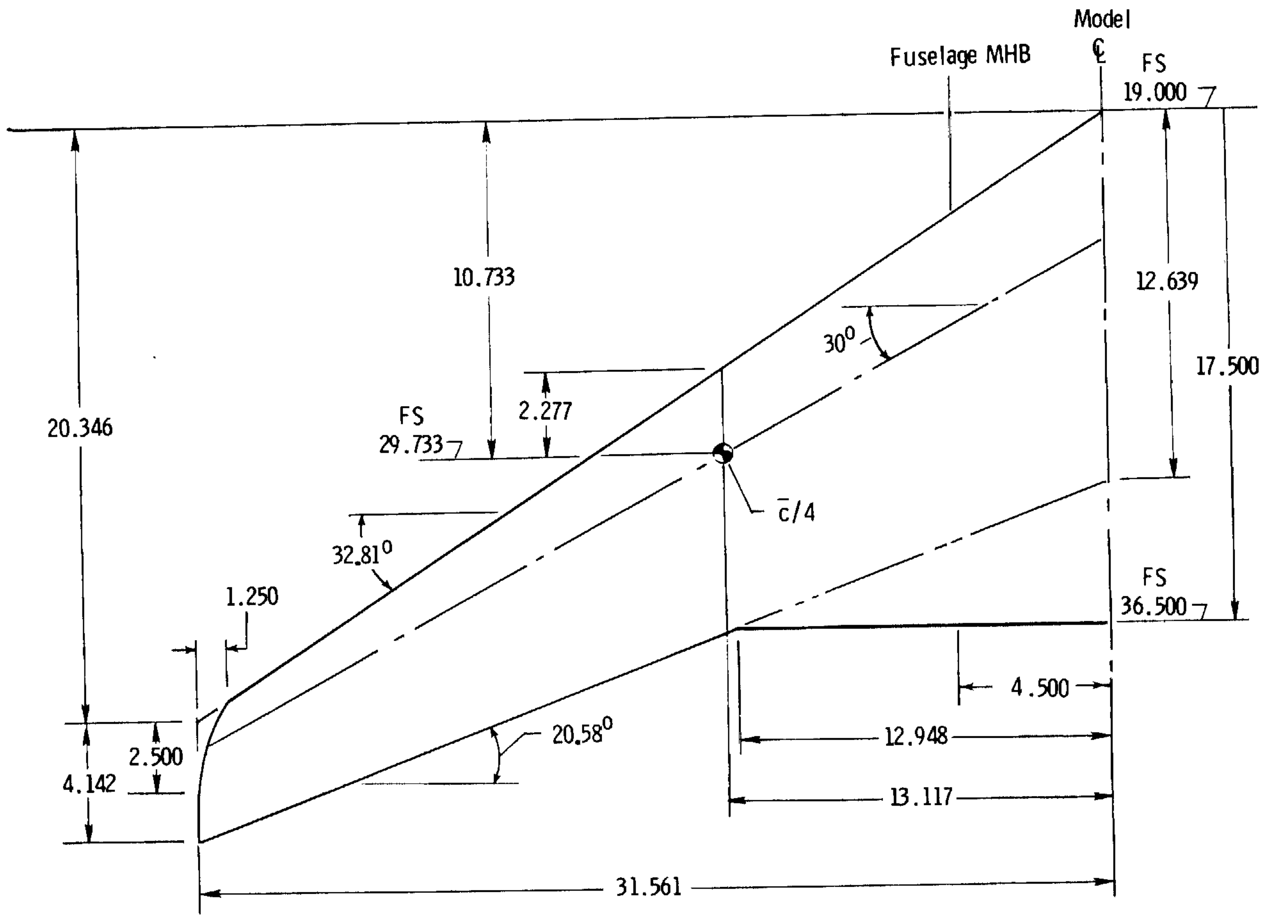

Aspect ratio	7.52
Taper ratio	0.328
Area (trapezoid), in^2 ..	529.590
$\bar{c}$, in.	9.107
c_{av}, in.	8.390
Incidence, deg........	0
Dihedral, deg.........	0

Figure 4. Wing planform. All dimensions are in inches unless otherwise specified.

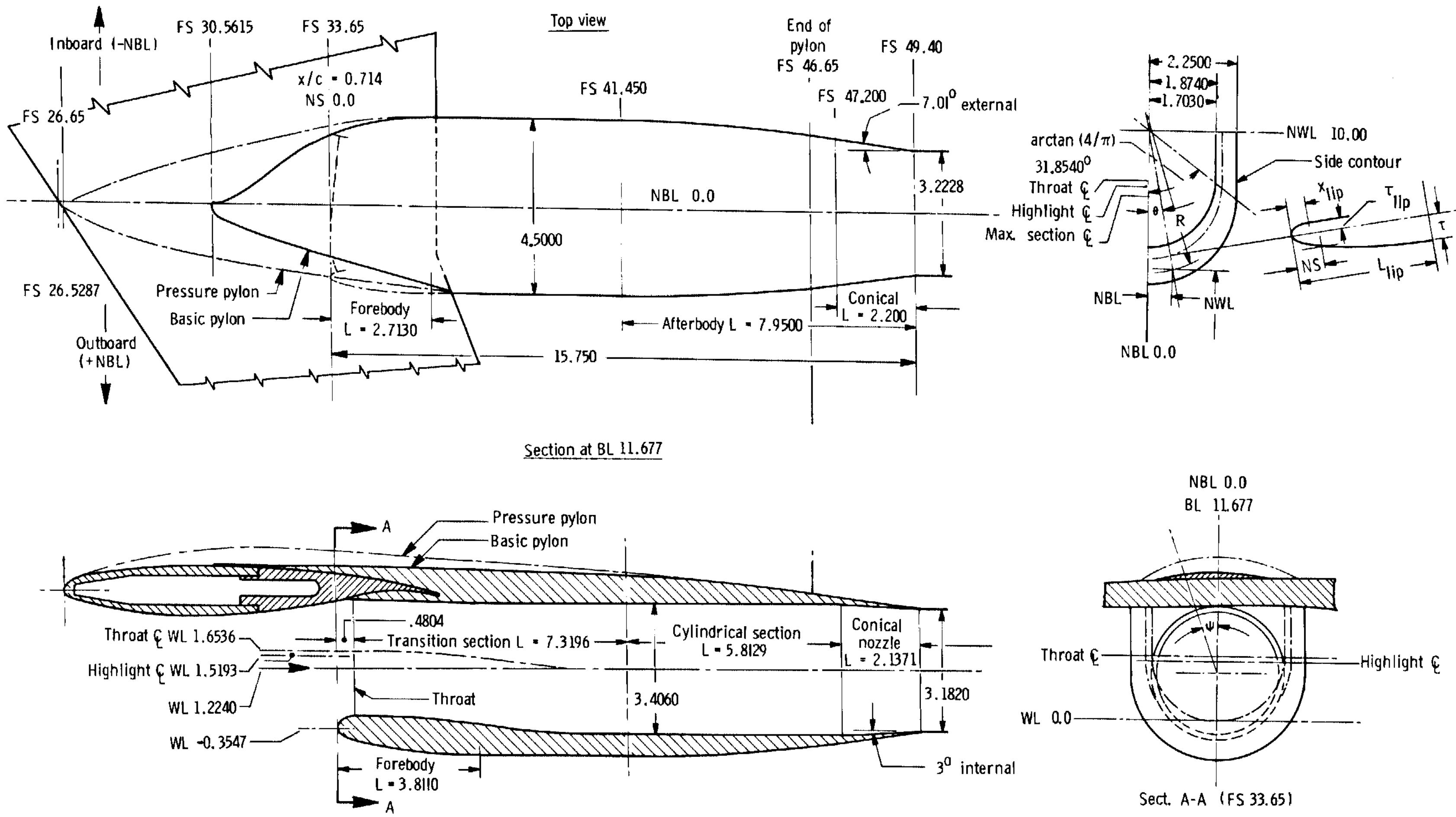

(a) Aft wing-mounted D-nacelle at $x/c = 0.714$ and $\eta = 0.370$. ($A_0/A_{HL} = 0.70$; $A_{HL} = 11.03$ in^2; $A_{max} = 15.90$ in^2; $D_{exit} = 3.182$ in.). All dimensions are in inches unless otherwise specified.

Figure 5. Aft wing-mounted D-nacelle.

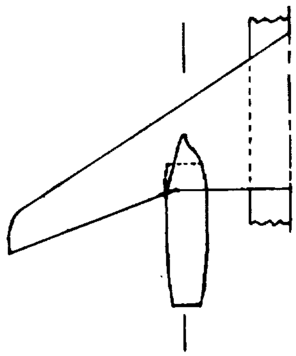

x/c = 0.714
η = 0.370

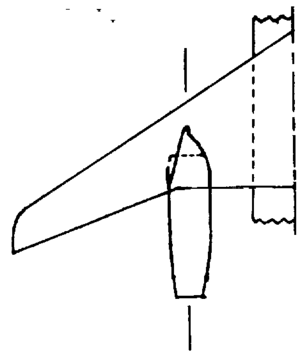

x/c = 0.614
η = 0.370

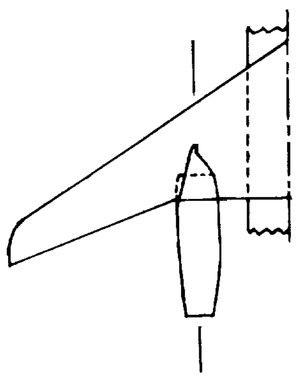

x/c = 0.736
η = 0.328

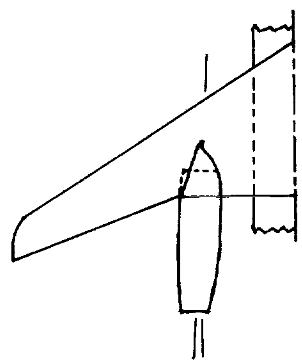

2° toe-in
x/c = 0.736
η = 0.328

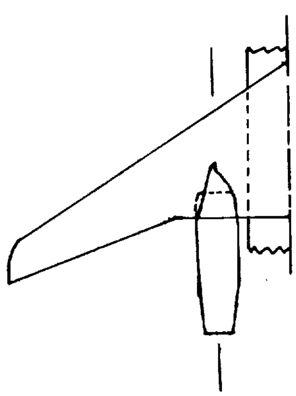

x/c = 0.768
η = 0.255

(b) D-nacelle positions.

Figure 5. Continued.

ORIGINAL PAGE
BLACK AND WHITE PHOTOGRAPH

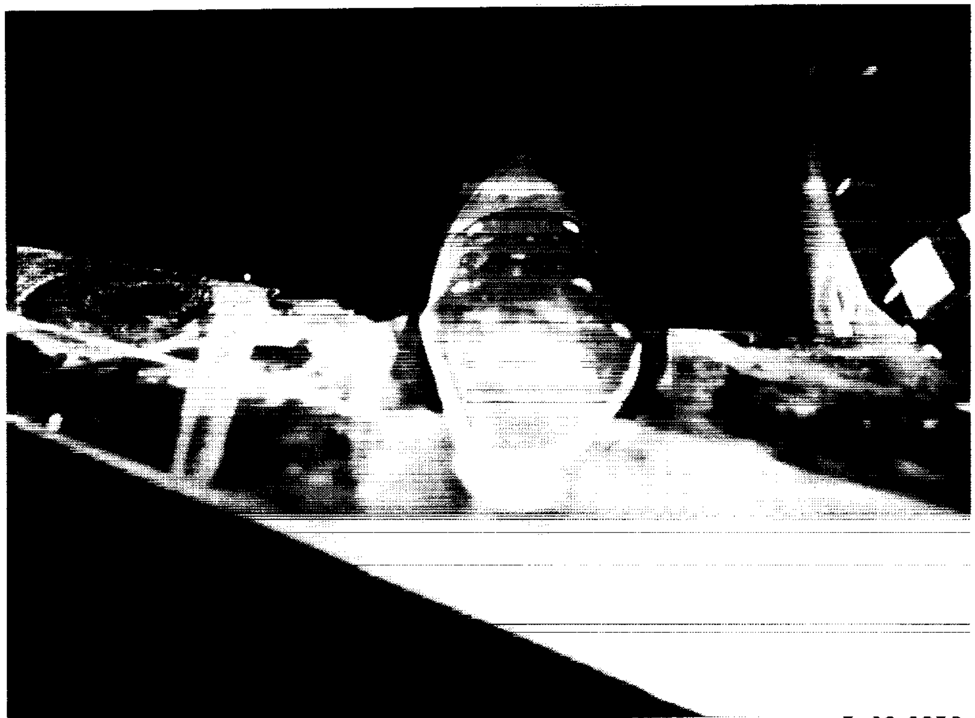

L-83-9356

L-83-9357

(c) Aft-wing-mounted D-nacelle at $x/c = 0.614$ and $\eta = 0.370$.

Figure 5. Concluded.

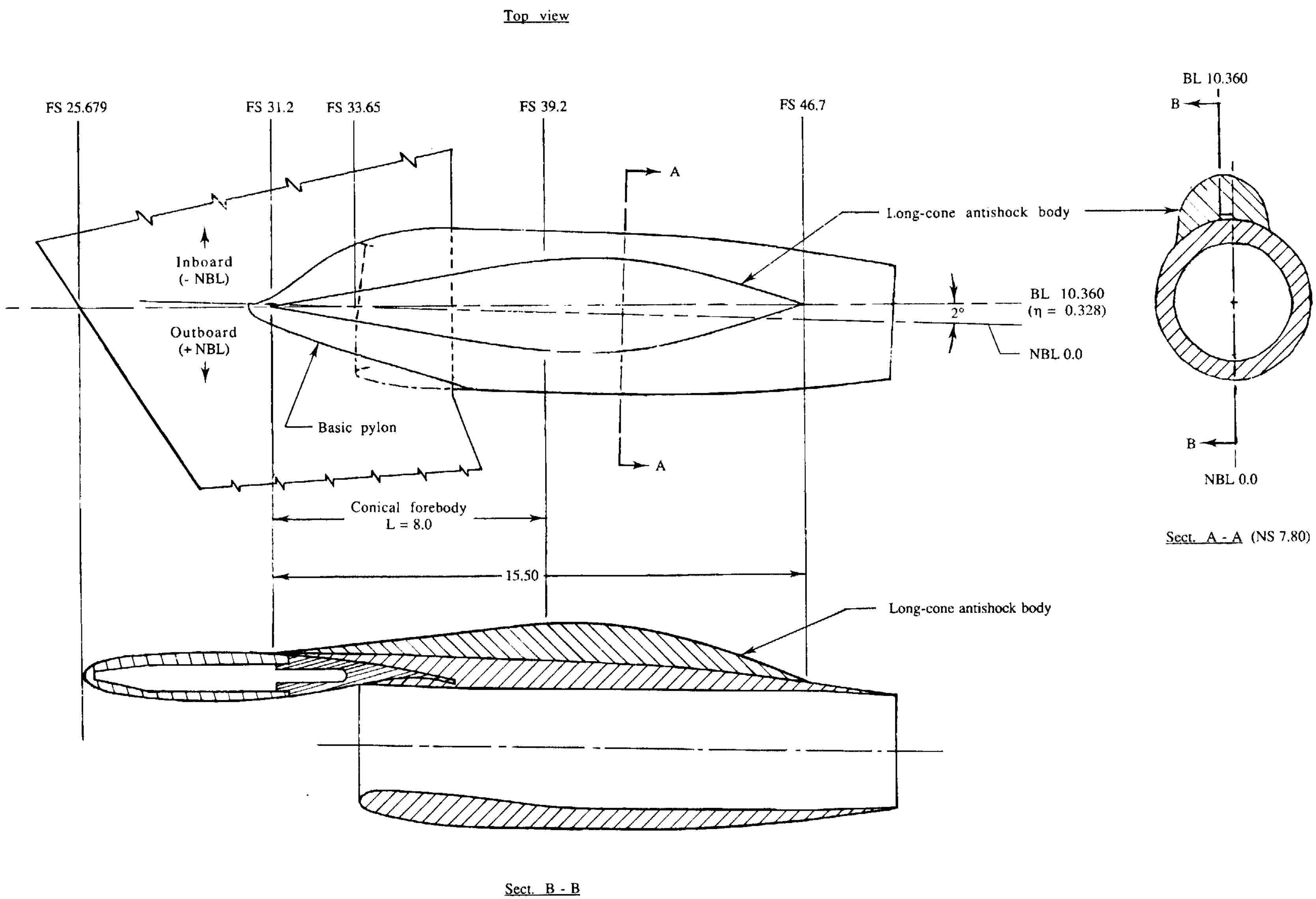

Figure 6. The FS 31.2 long-cone antishock body installed on 2° toed-in D-nacelle at $x/c = 0.736$ and $\eta = 0.328$.

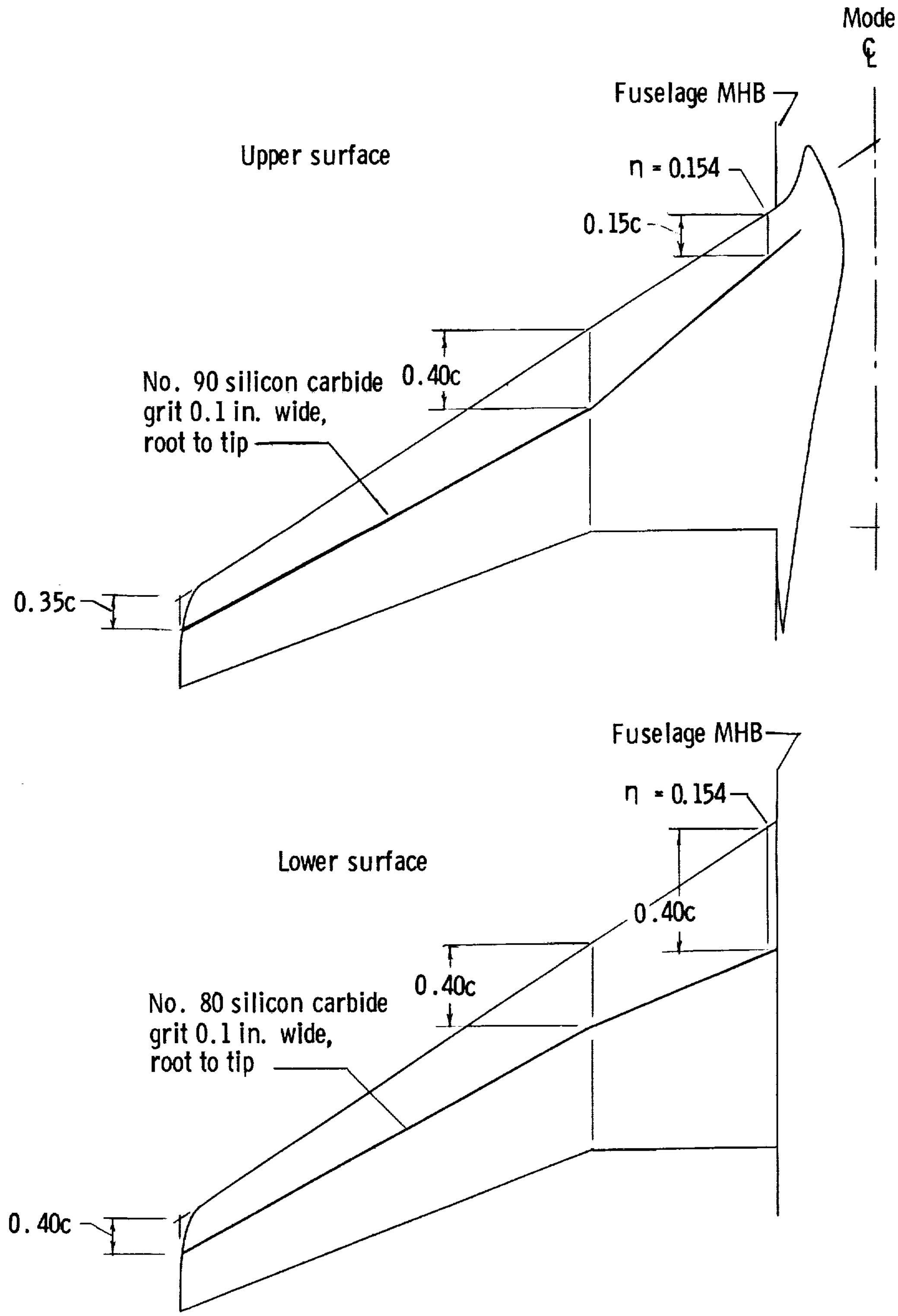

Figure 7. Wing transition-strip locations.

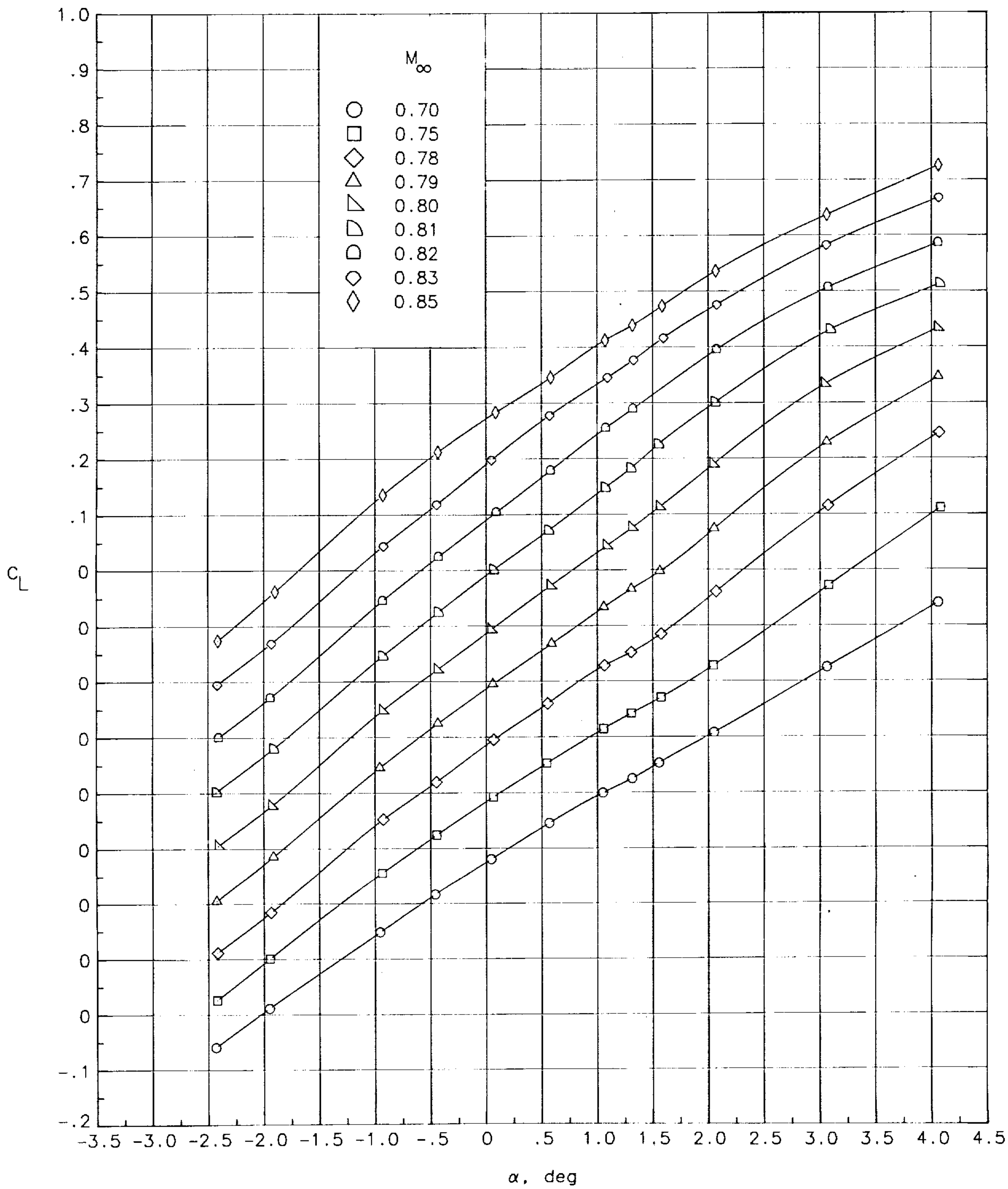

(a) Variation of lift coefficient with angle of attack.

Figure 8. Longitudinal aerodynamic characteristics for wing-body/tail configuration.

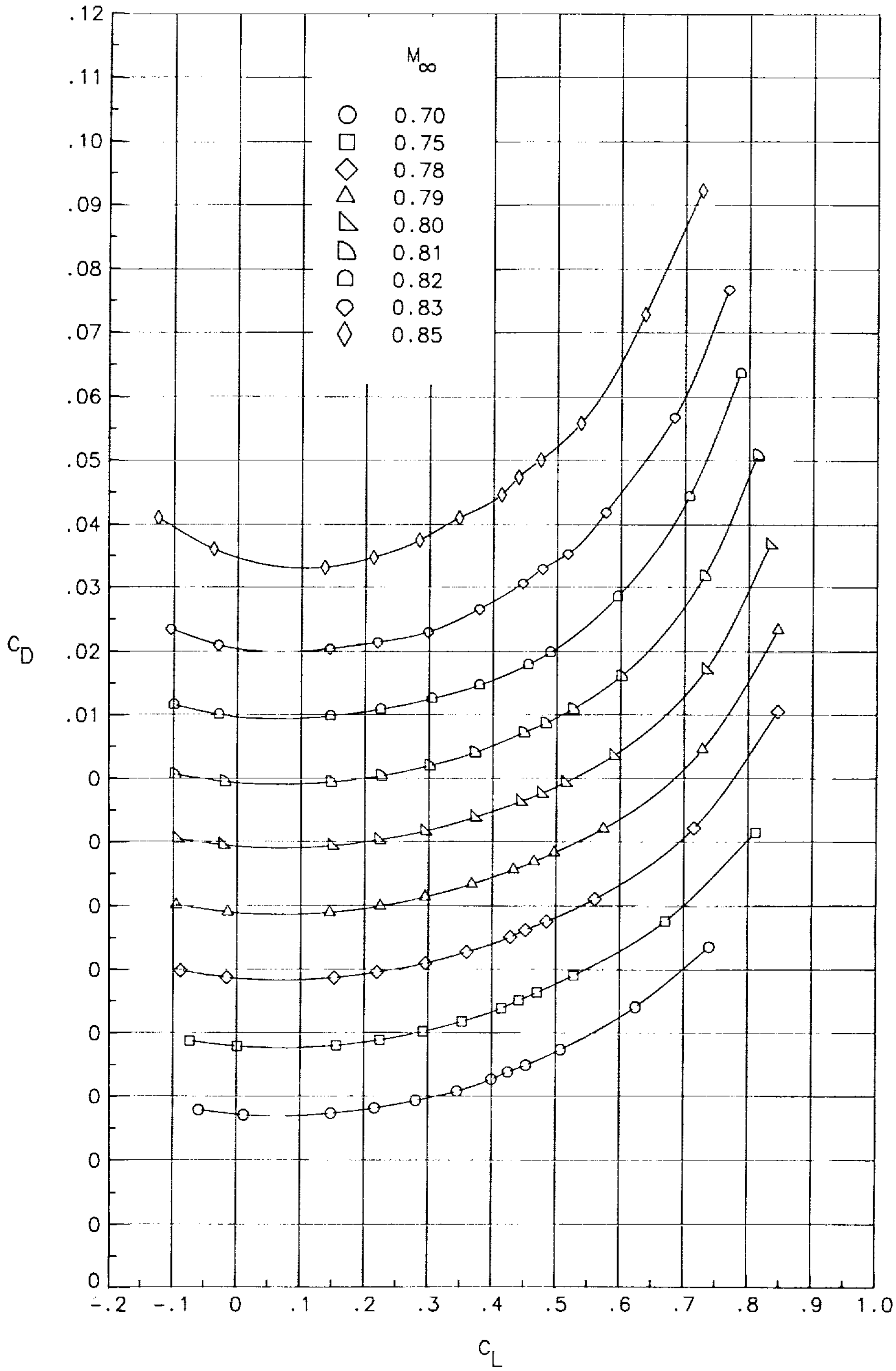

(b) Variation of drag coefficient with lift coefficient.

Figure 8. Continued.

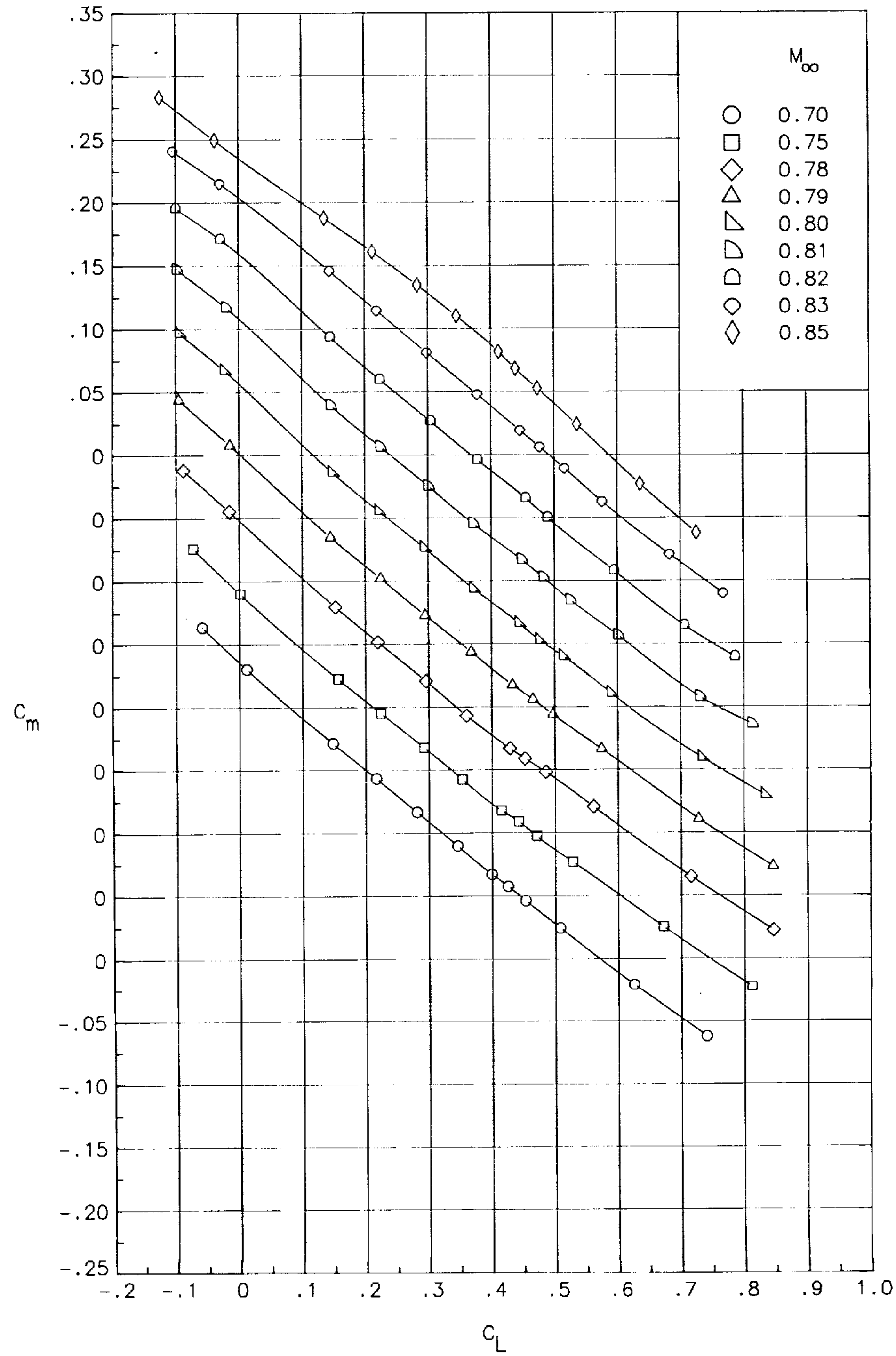

(c) Variation of pitching-moment coefficient with lift coefficient.

Figure 8. Continued.

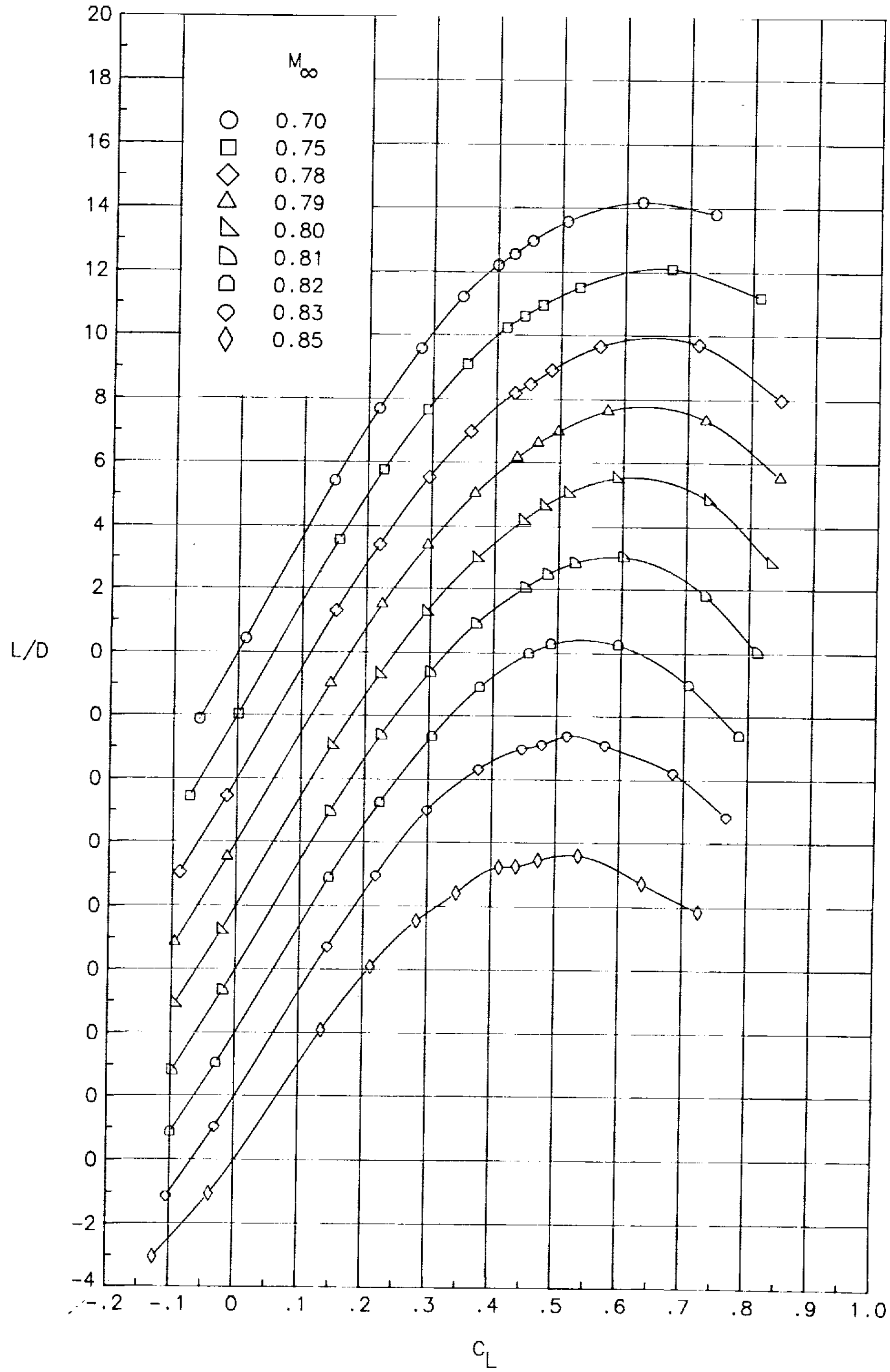

(d) Variation of lift-drag ratio with lift coefficient.

Figure 8. Concluded.

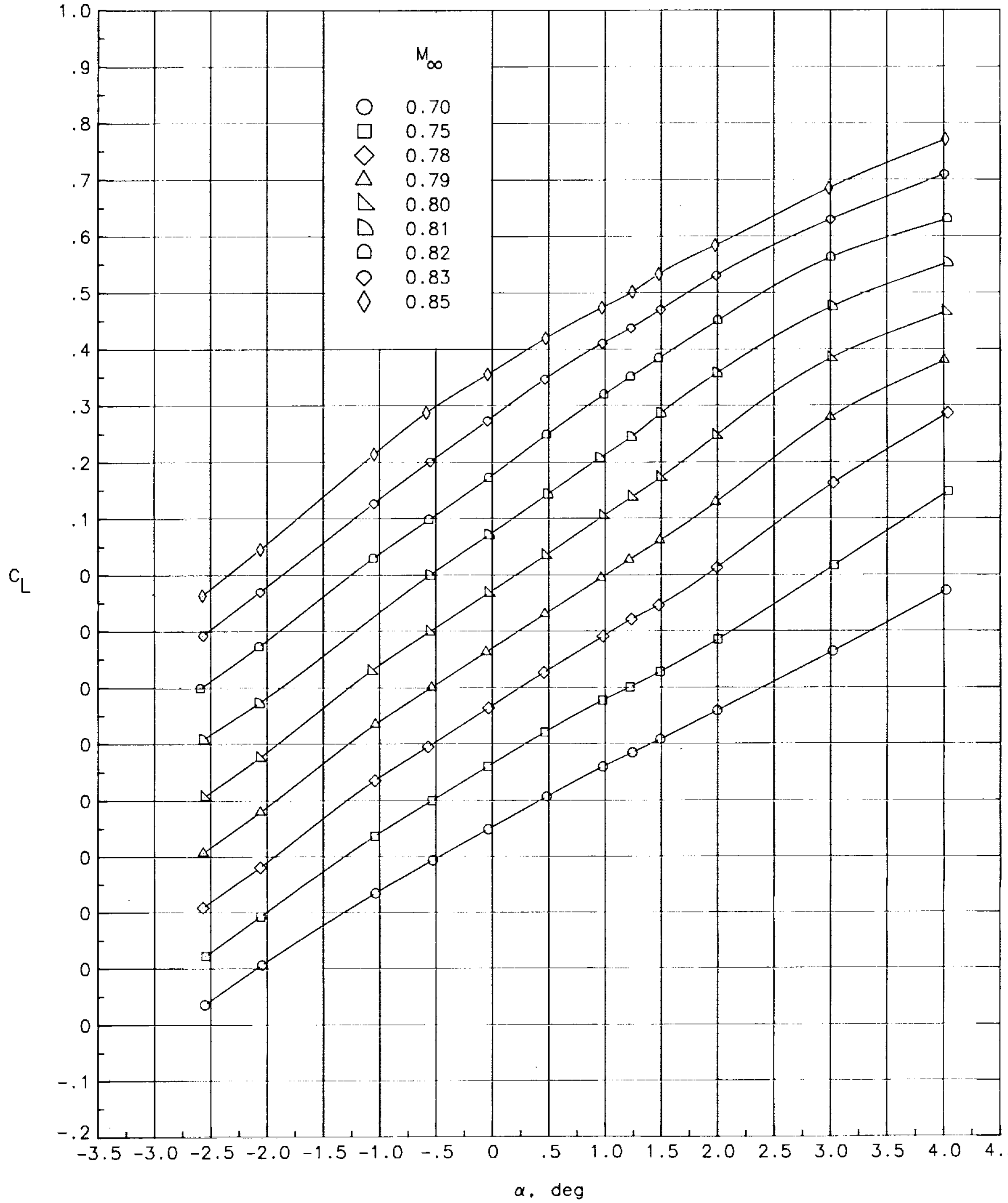

(a) Variation of lift coefficient with angle of attack.

Figure 9. Longitudinal aerodynamic characteristics for wing-body configuration.

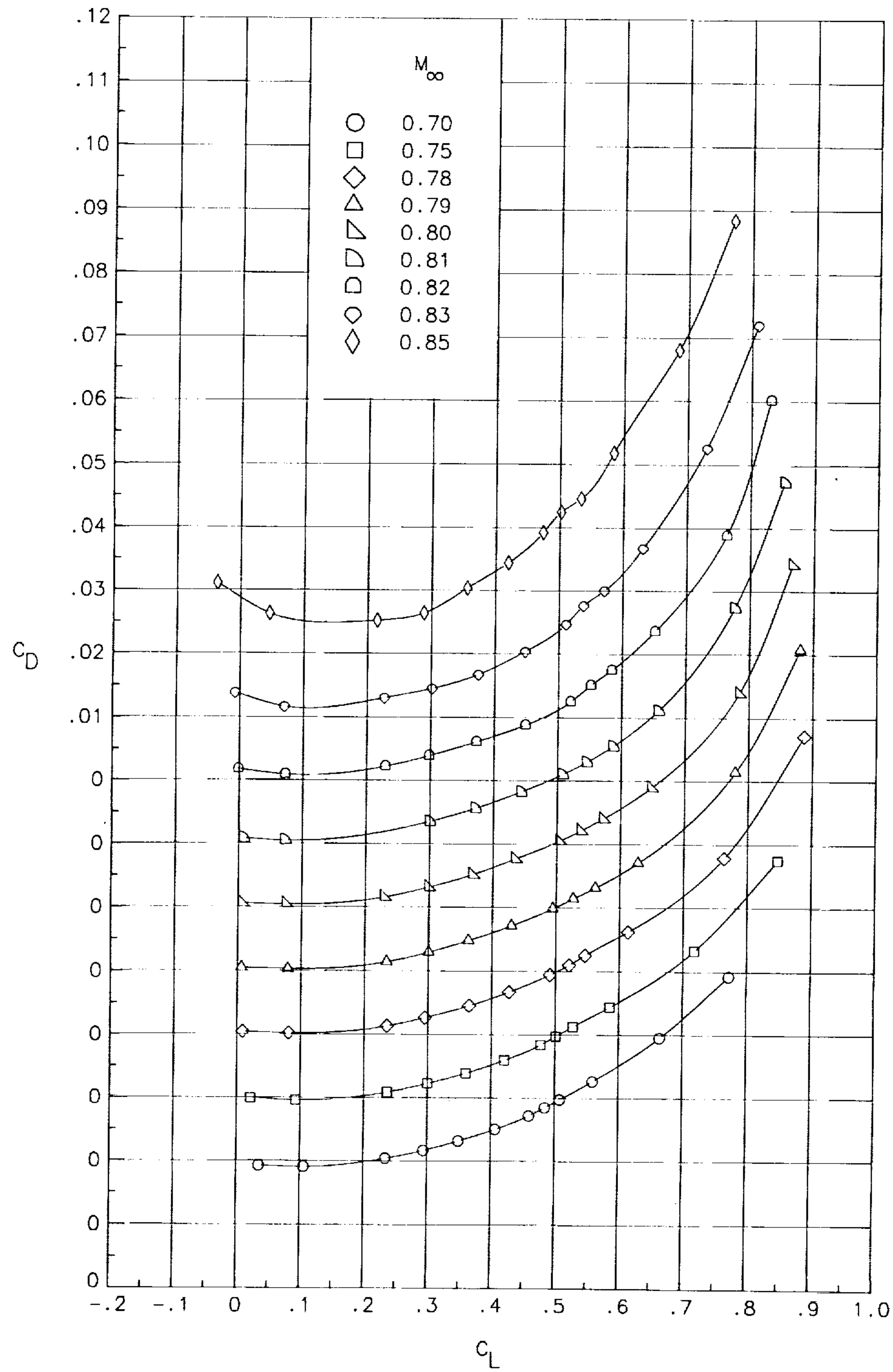

(b) Variation of drag coefficient with lift coefficient.

Figure 9. Continued.

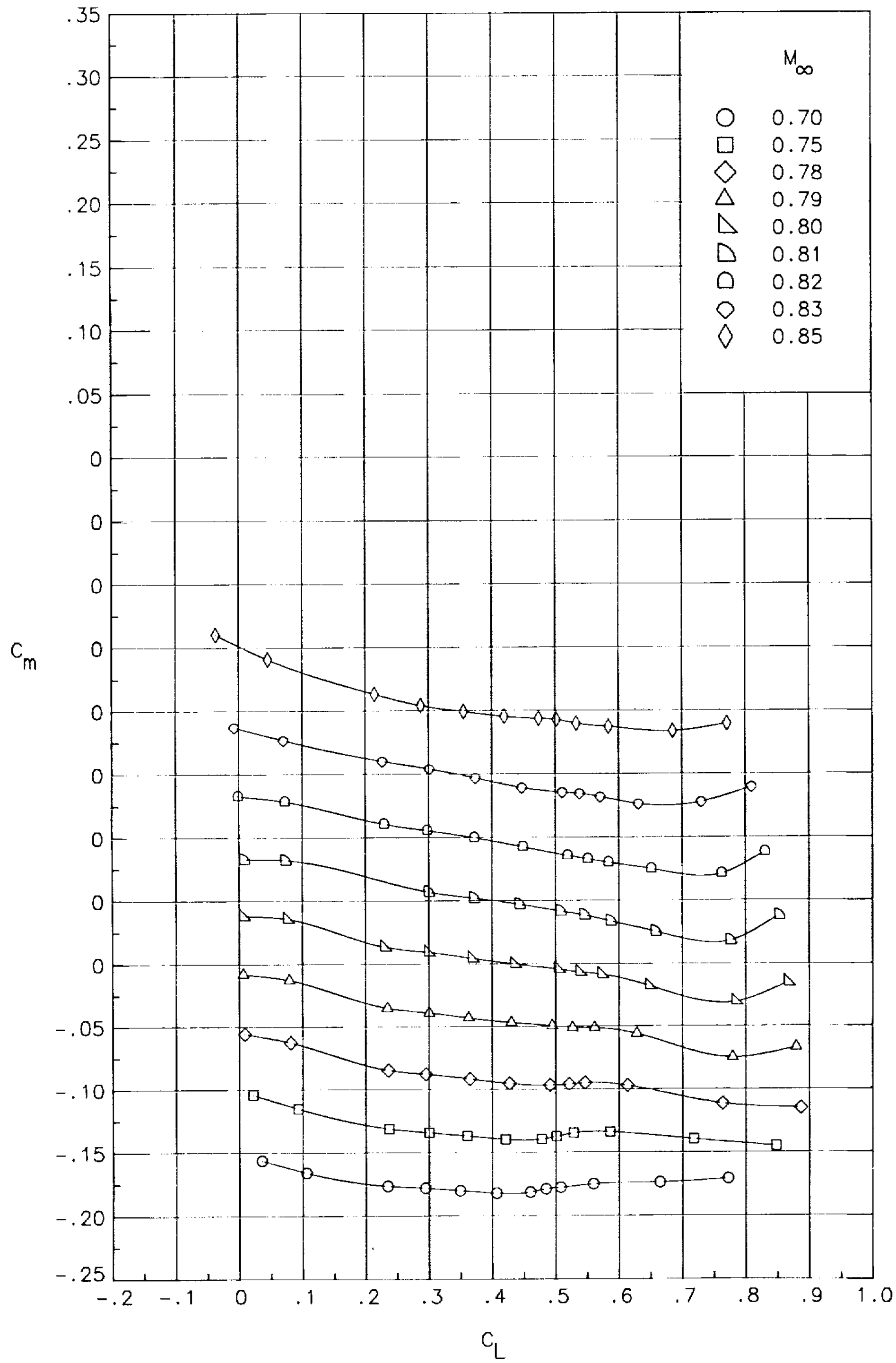

(c) Variation of pitching-moment coefficient with lift coefficient.

Figure 9. Continued.

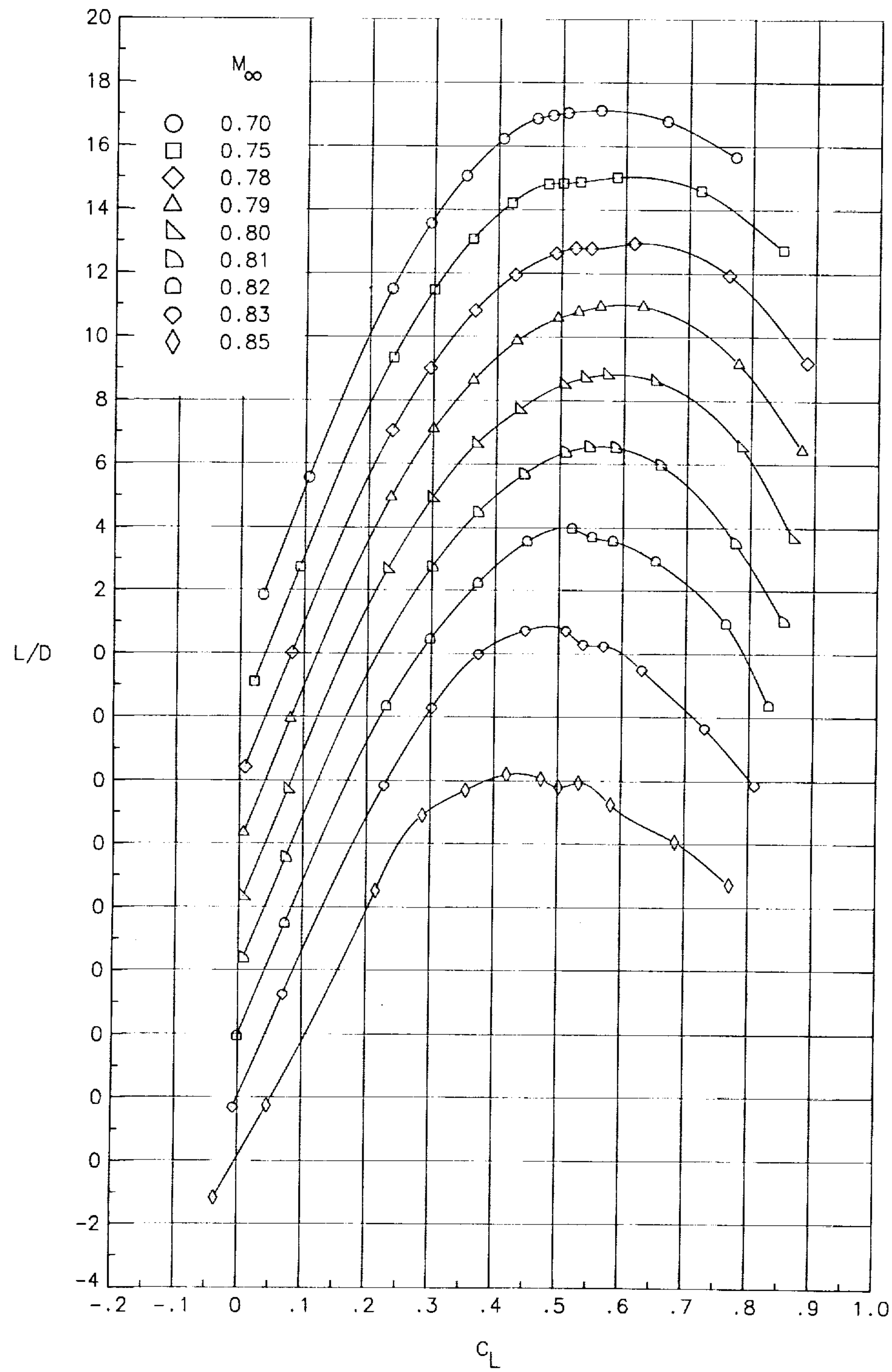

(d) Variation of lift-drag ratio with lift coefficient.

Figure 9. Concluded.

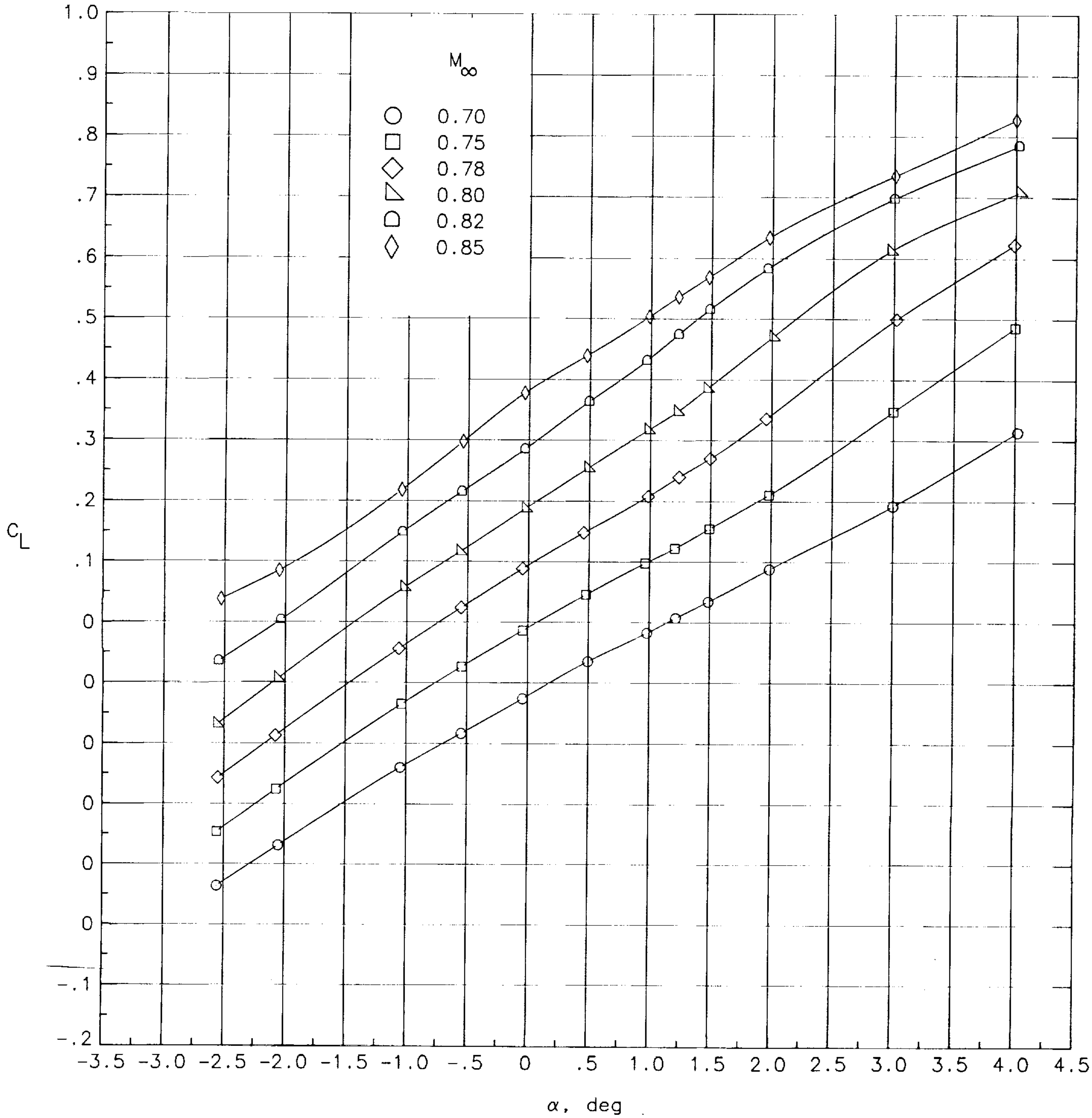

(a) Variation of lift coefficient with angle of attack.

Figure 10. Longitudinal aerodynamic characteristics for wing-body configuration with D-nacelles at $x/c = 0.614$ and $\eta = 0.370$.

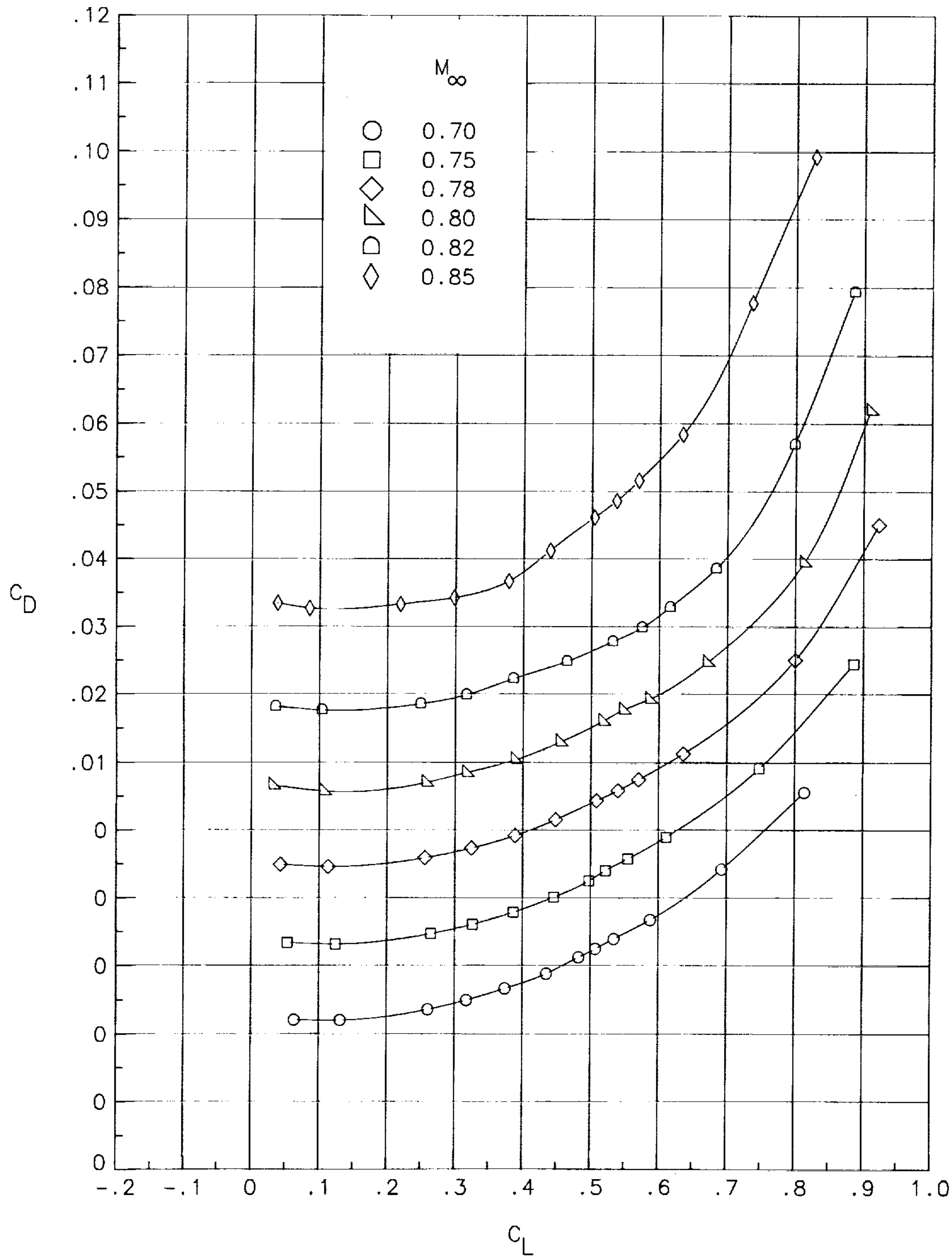

(b) Variation of drag coefficient with lift coefficient.

Figure 10. Continued.

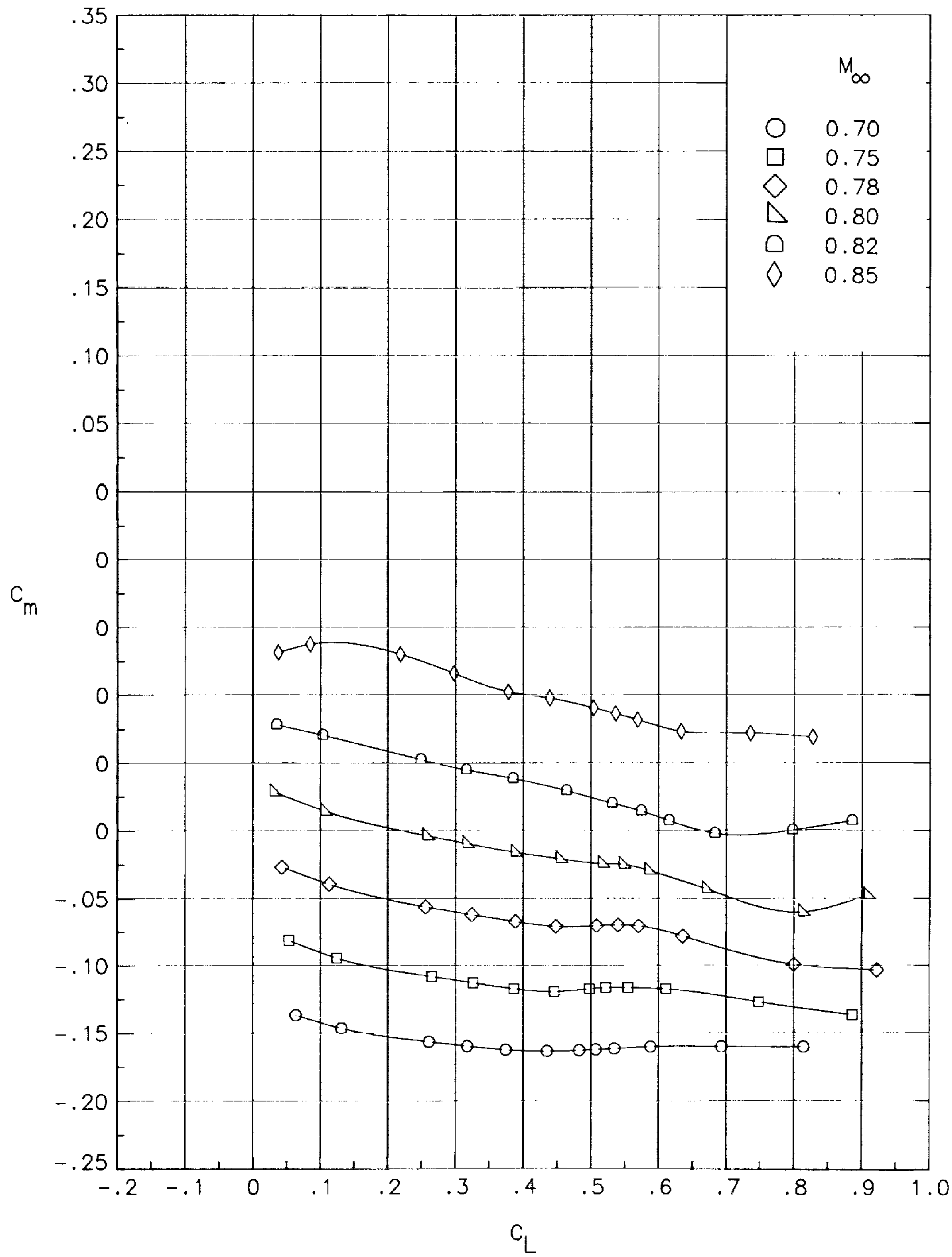

(c) Variation of pitching-moment coefficient with lift coefficient.

Figure 10. Continued.

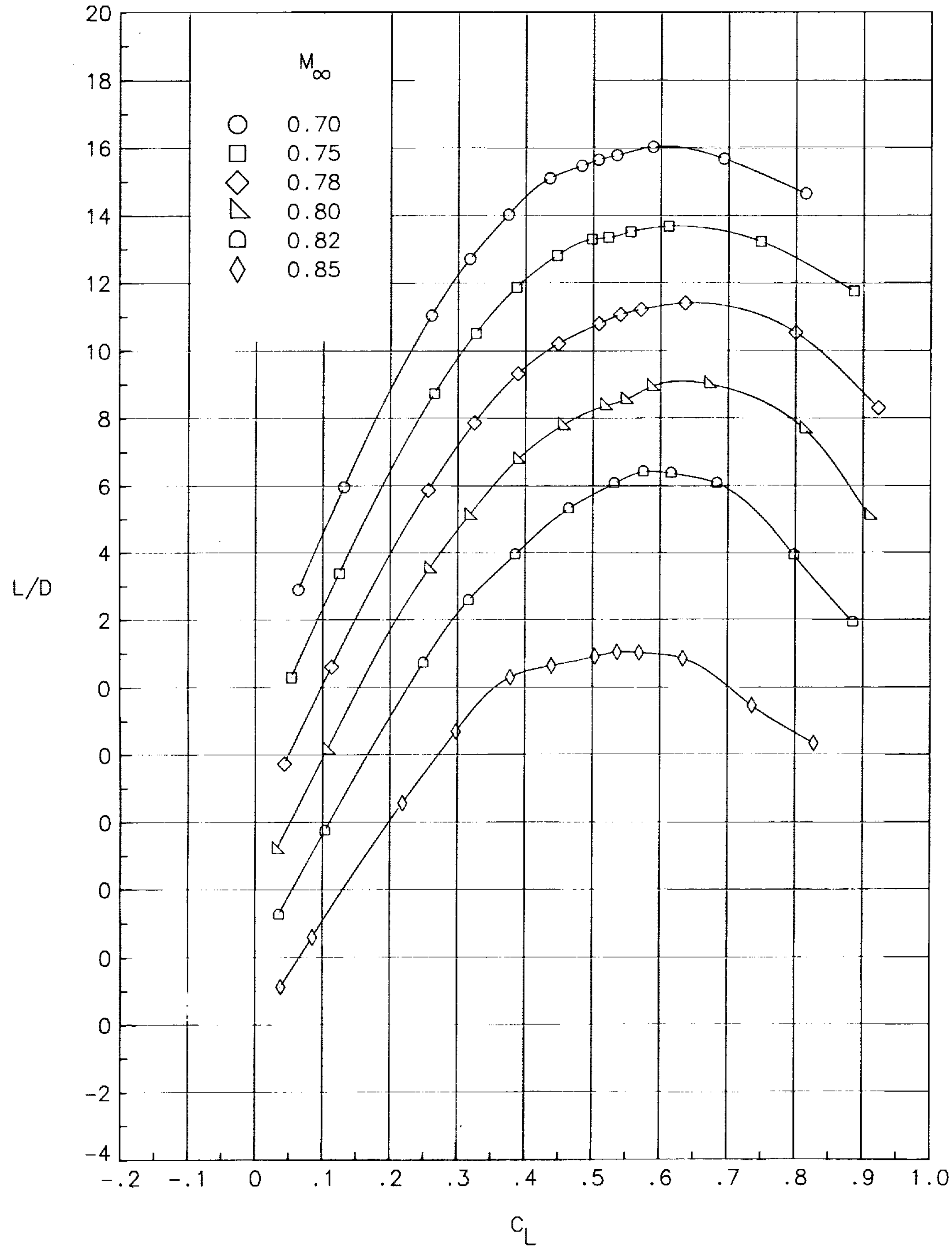

(d) Variation of lift-drag ratio with lift coefficient.

Figure 10. Concluded.

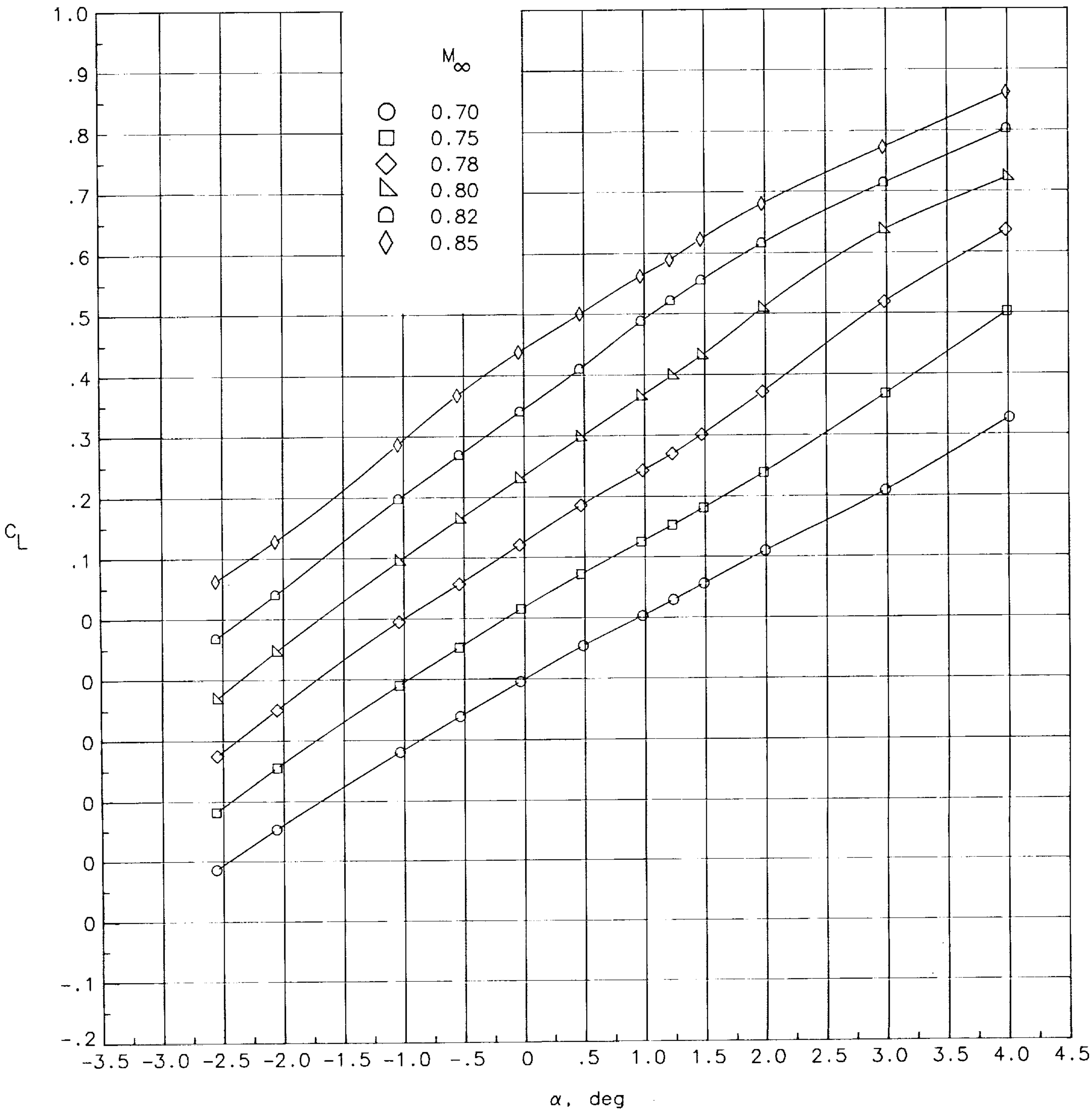

(a) Variation of lift coefficient with angle of attack.

Figure 11. Longitudinal aerodynamic characteristics for wing-body configuration with D-nacelles at $x/c = 0.714$ and $\eta = 0.370$.

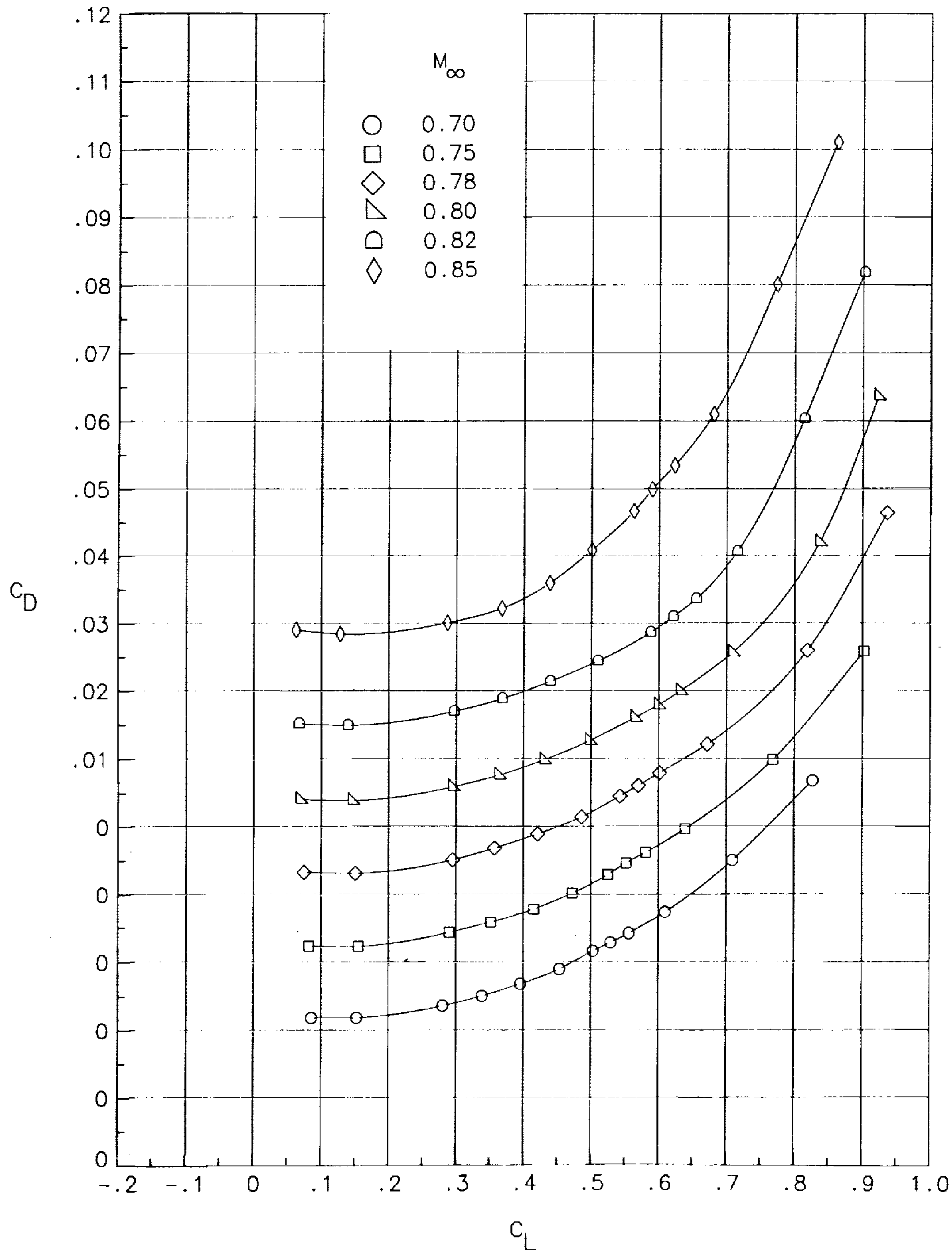

(b) Variation of drag coefficient with lift coefficient.

Figure 11. Continued.

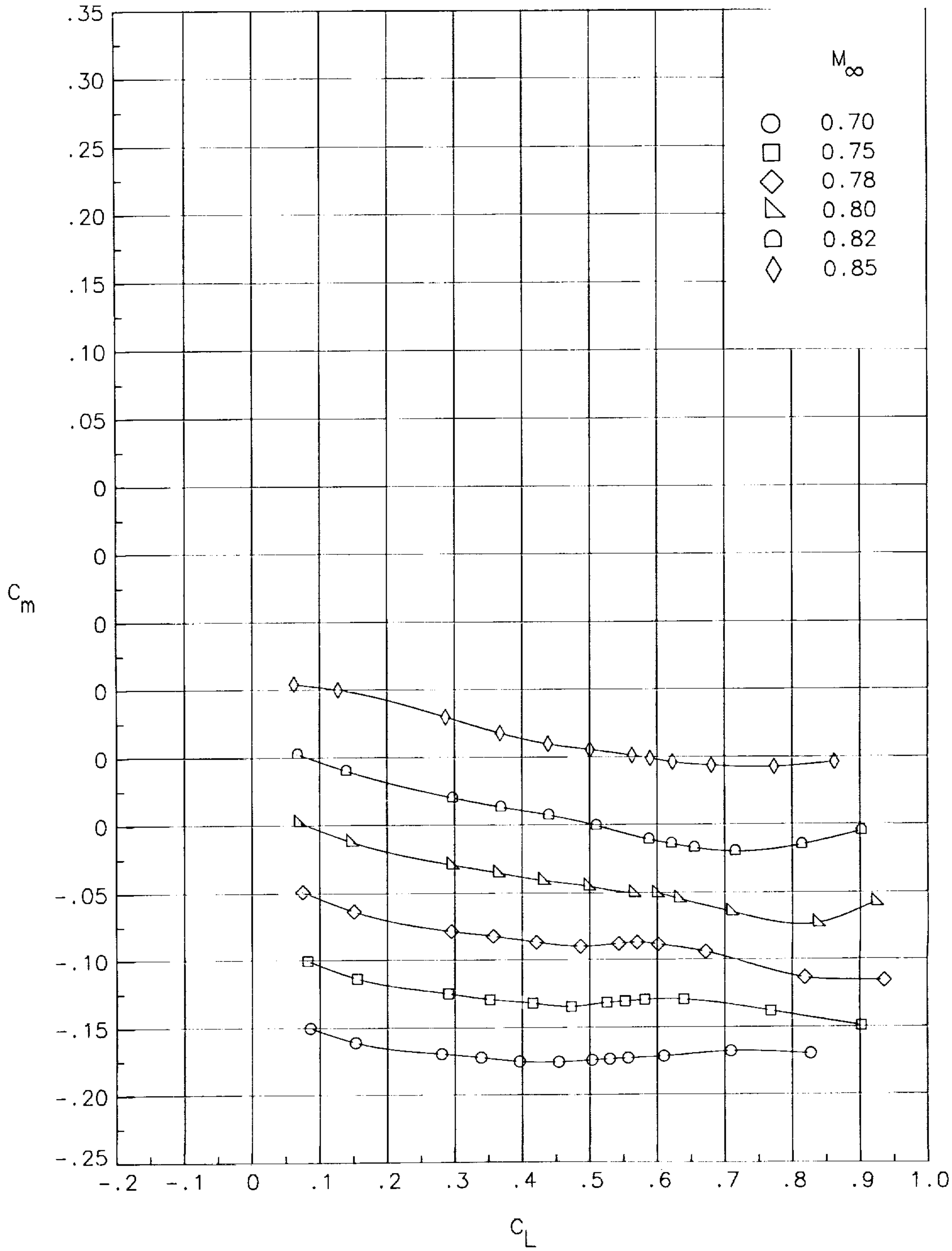

(c) Variation of pitching-moment coefficient with lift coefficient.

Figure 11. Continued.

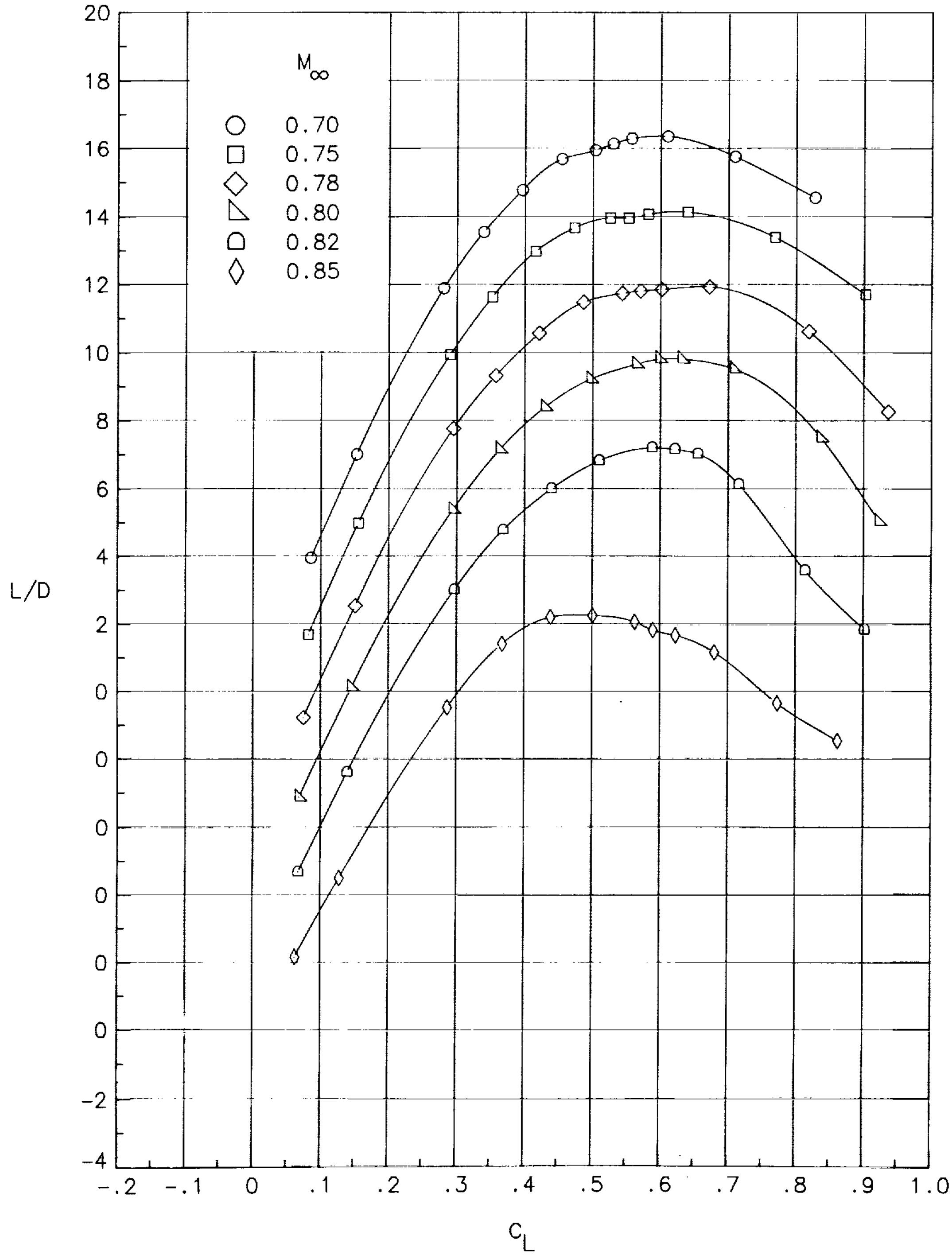

(d) Variation of lift-drag ratio with lift coefficient.

Figure 11. Concluded.

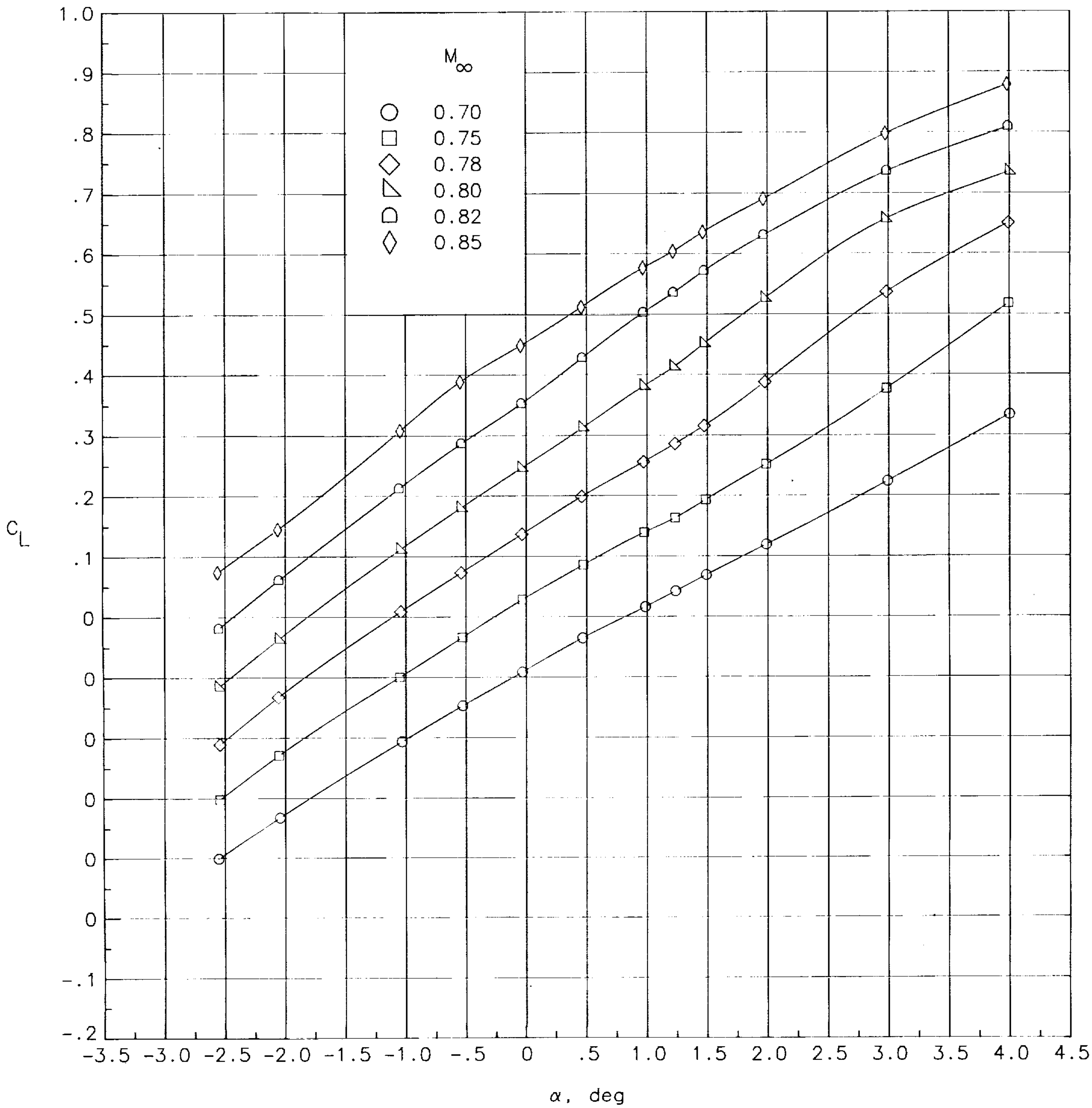

(a) Variation of lift coefficient with angle of attack.

Figure 12. Longitudinal aerodynamic characteristics for wing-body configuration with D-nacelles at $x/c = 0.736$ and $\eta = 0.328$.

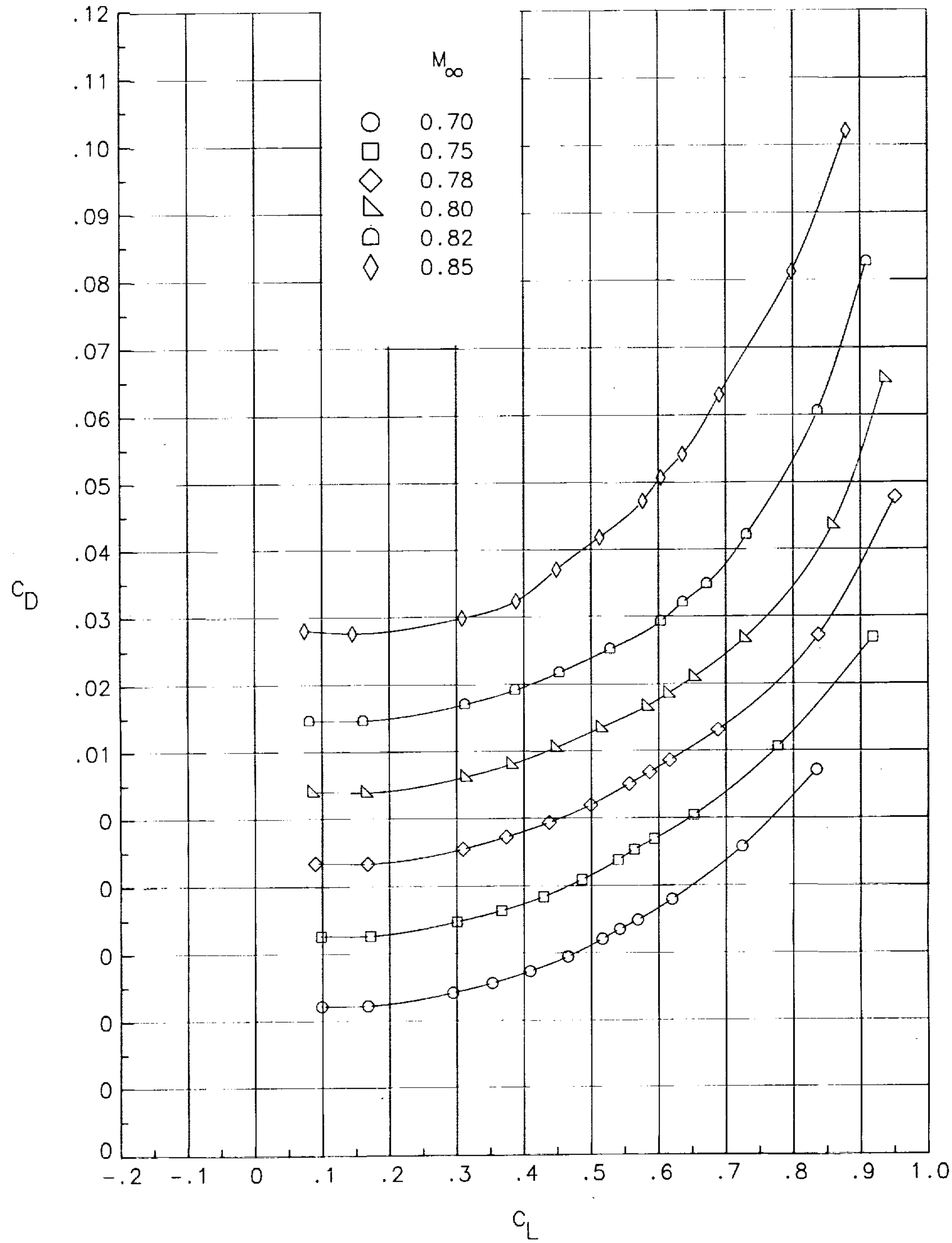

(b) Variation of drag coefficient with lift coefficient.

Figure 12. Continued.

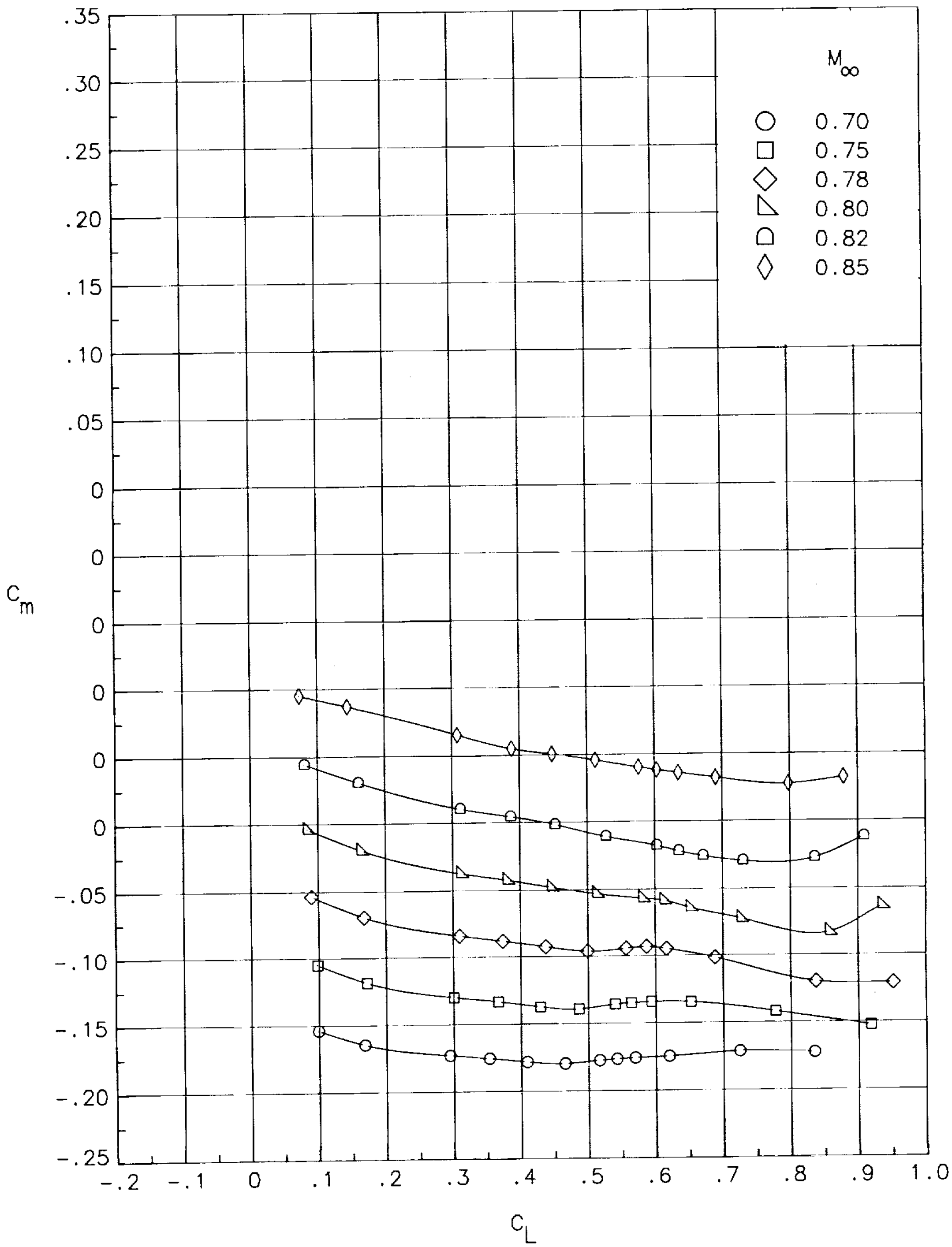

(c) Variation of pitching-moment coefficient with lift coefficient.

Figure 12. Continued.

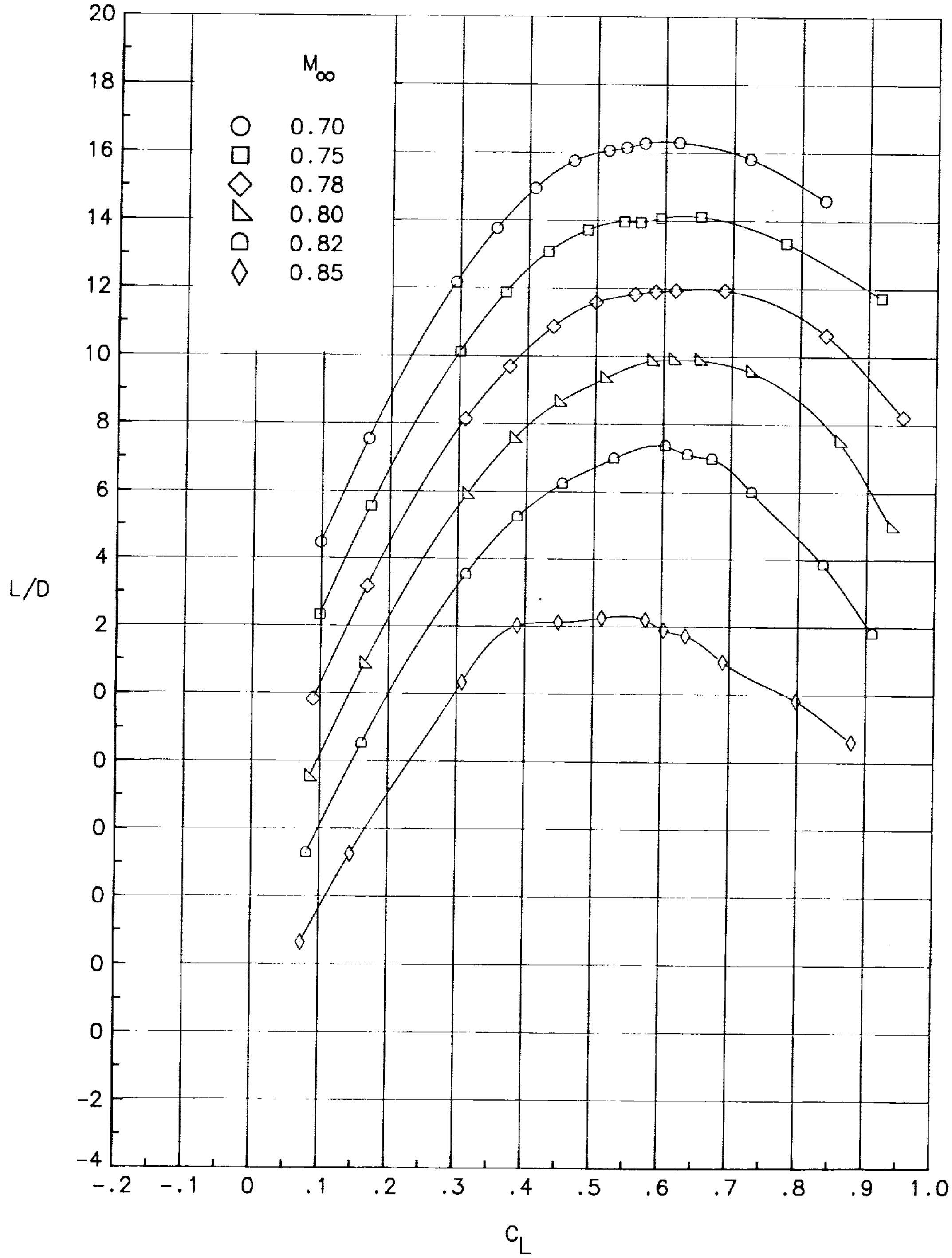

(d) Variation of lift-drag ratio with lift coefficient.

Figure 12. Concluded.

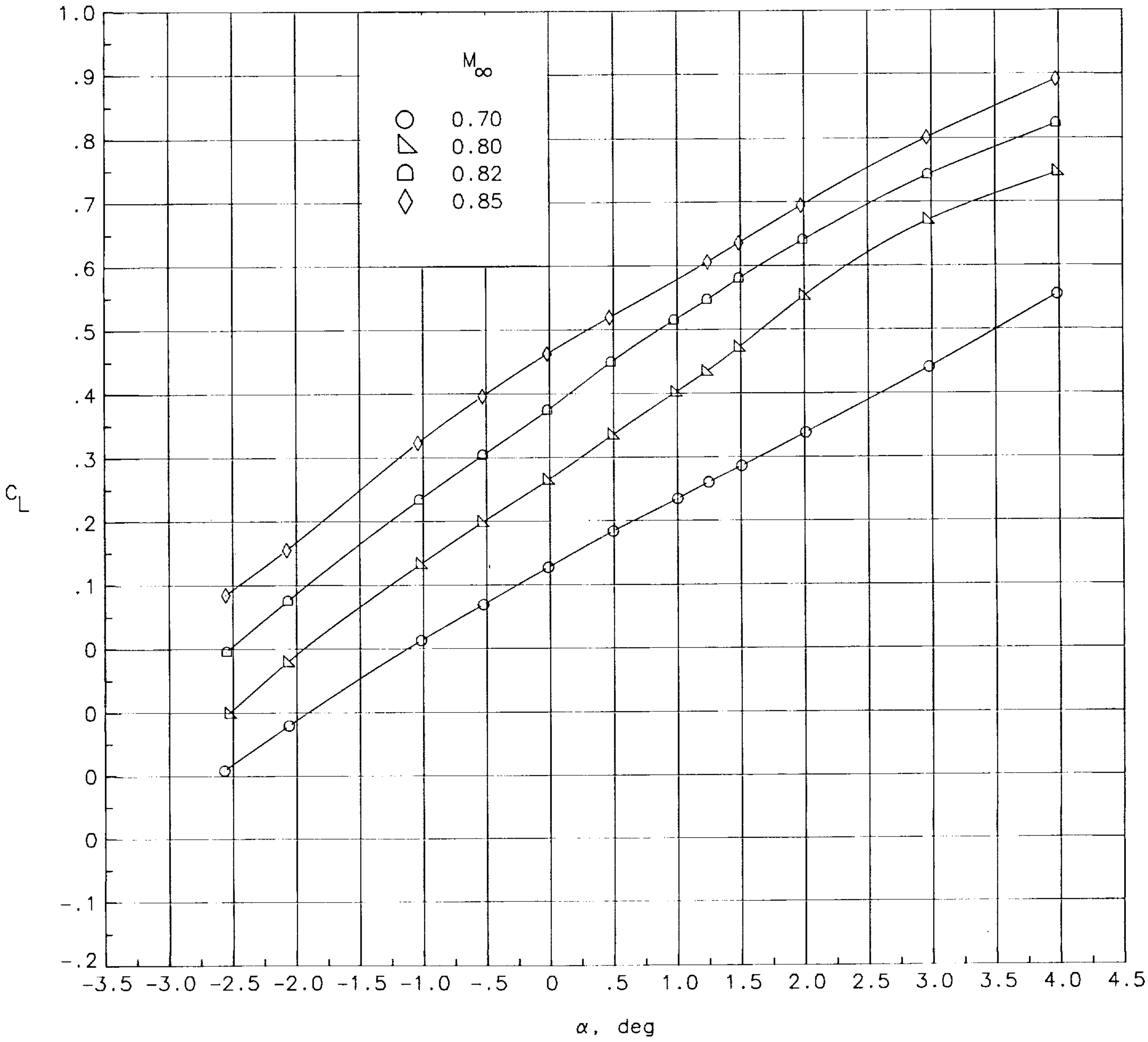

(a) Variation of lift coefficient with angle of attack.

Figure 13. Longitudinal aerodynamic characteristics for wing-body configuration with D-nacelles at $x/c = 0.768$ and $\eta = 0.255$.

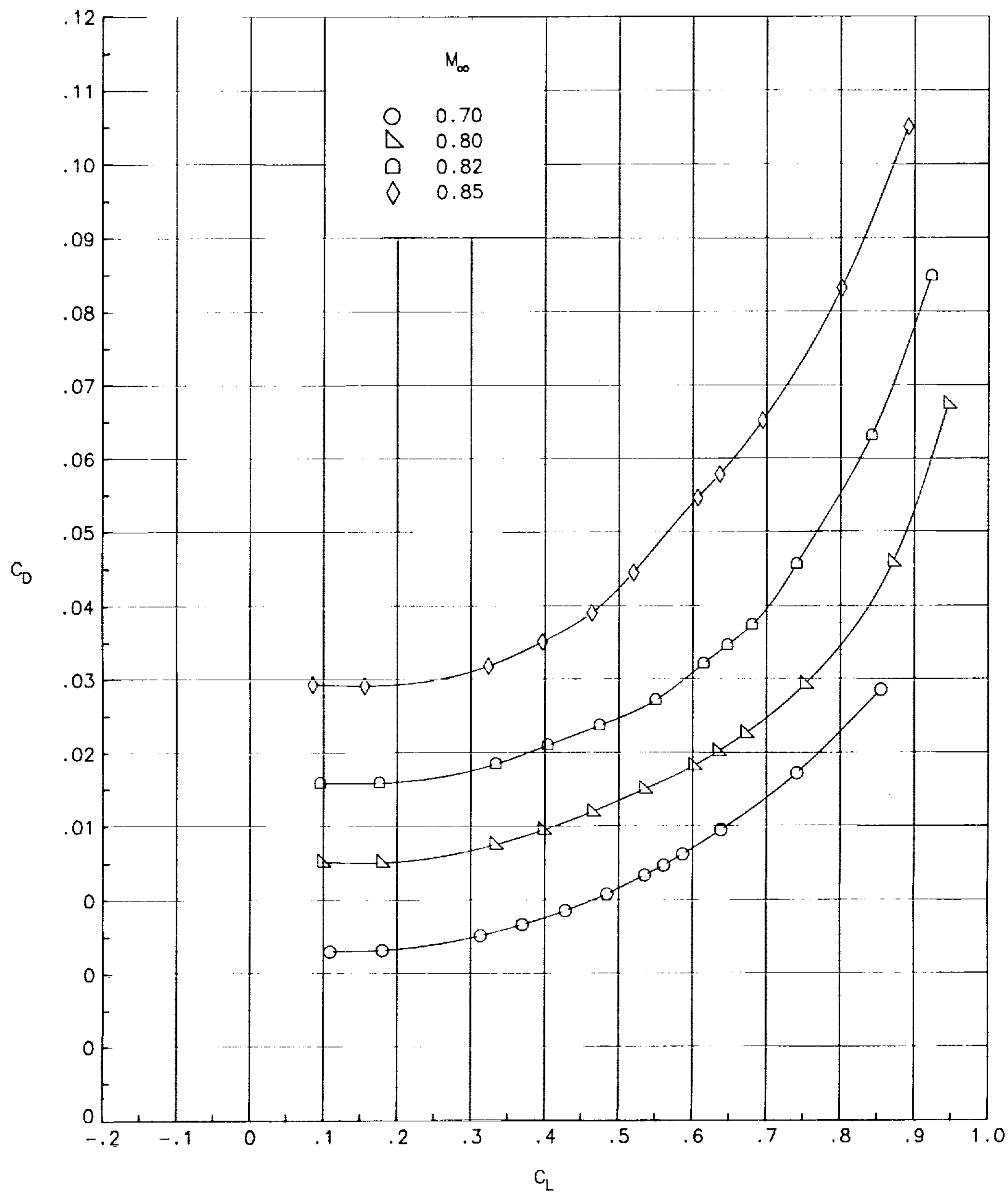

(b) Variation of drag coefficient with lift coefficient.

Figure 13. Continued.

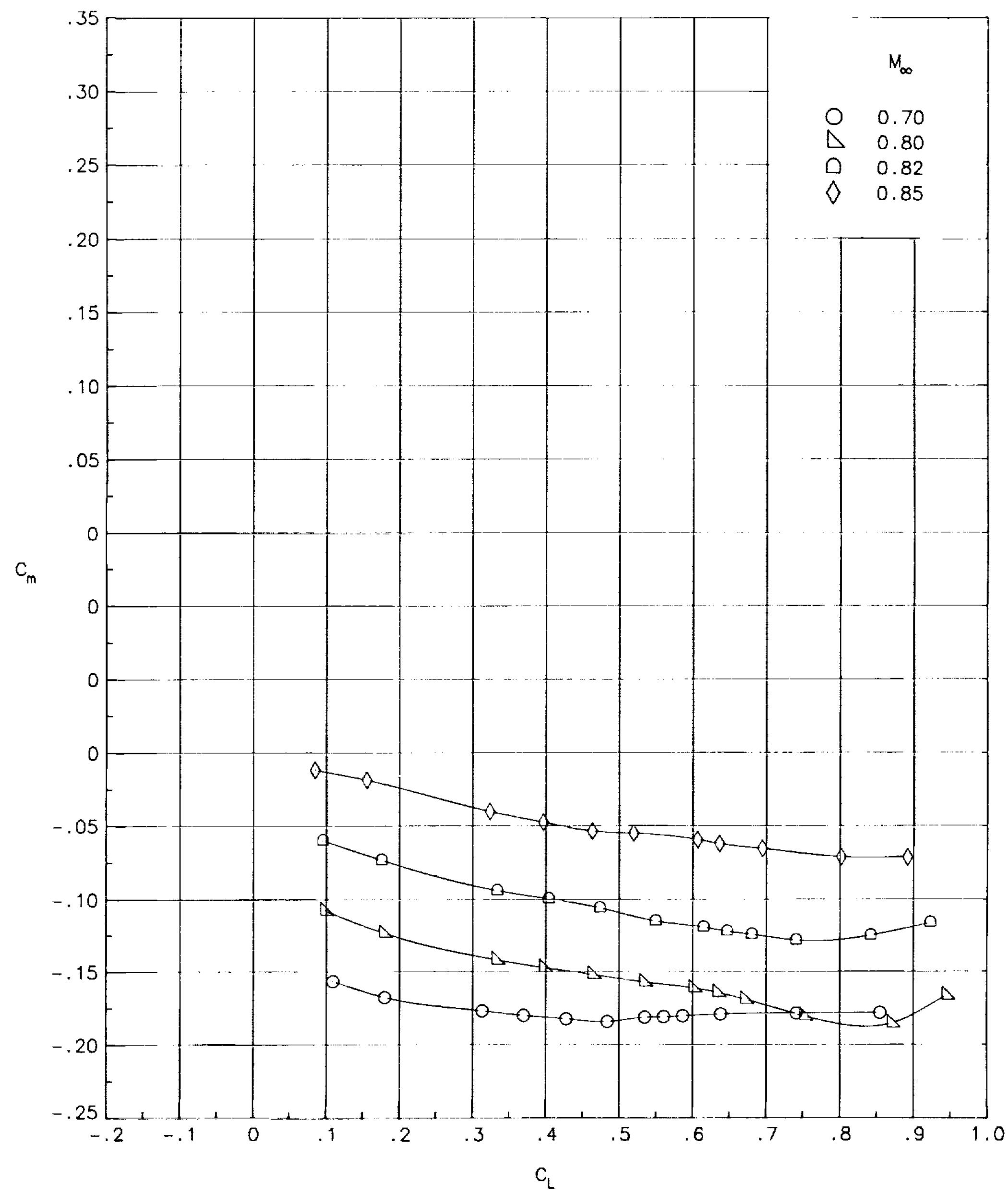

(c) Variation of pitching-moment coefficient with lift coefficient.

Figure 13. Continued.

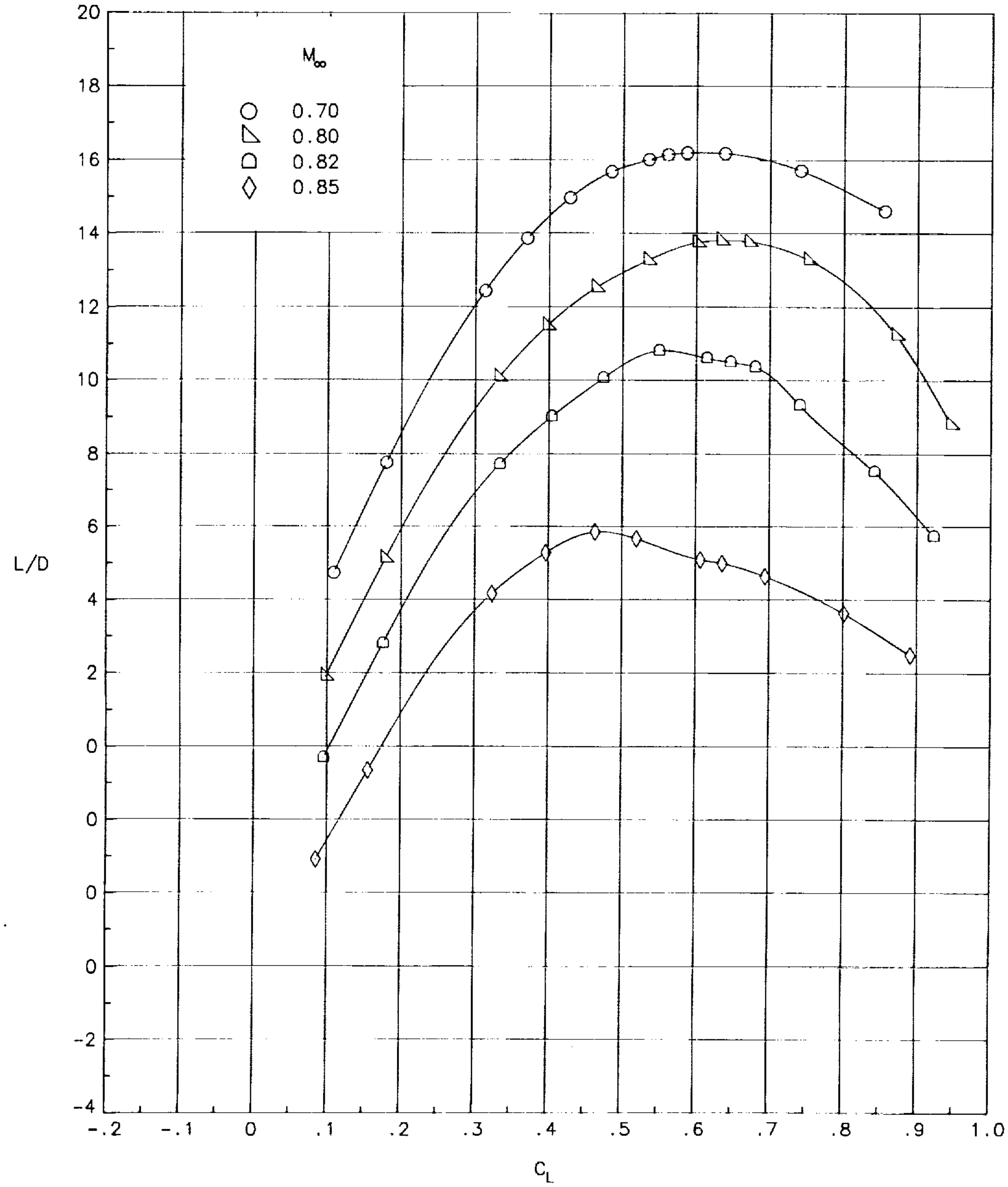

(d) Variation of lift-drag ratio with lift coefficient.

Figure 13. Concluded.

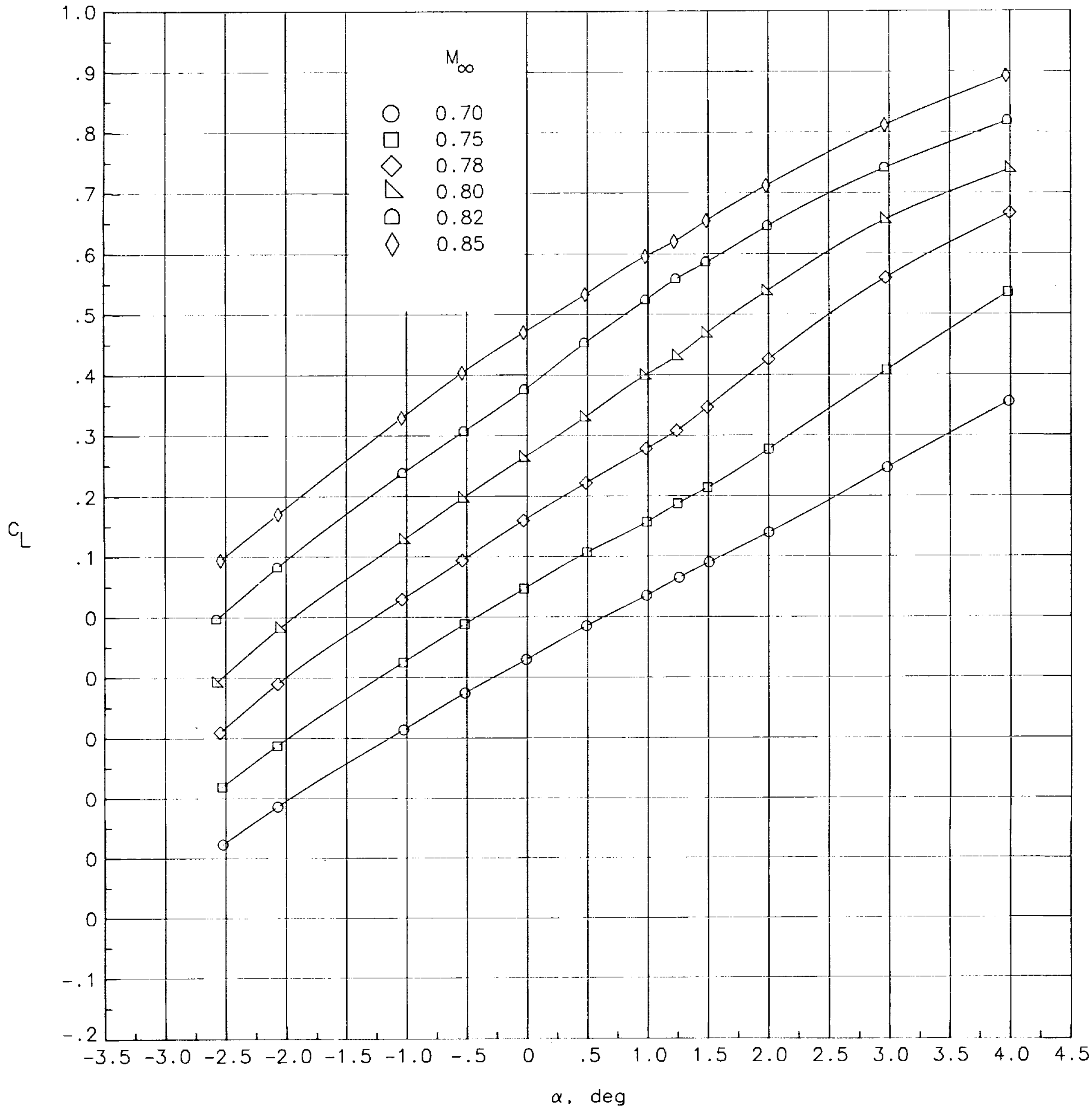

(a) Variation of lift coefficient with angle of attack.

Figure 14. Longitudinal aerodynamic characteristics for wing-body configuration with 2° toed-in D-nacelles at $x/c = 0.736$ and $\eta = 0.328$.

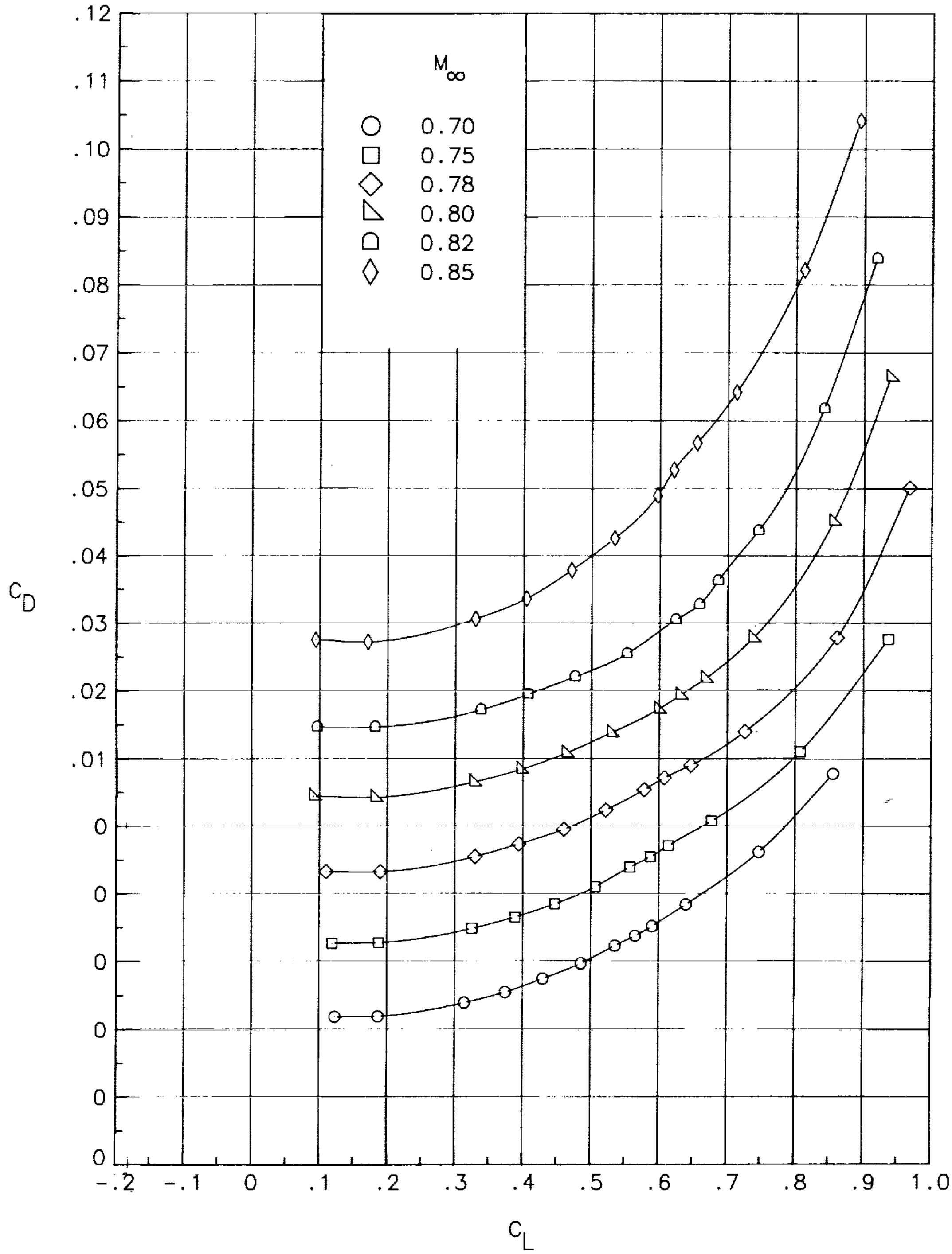

(b) Variation of drag coefficient with lift coefficient.

Figure 14. Continued.

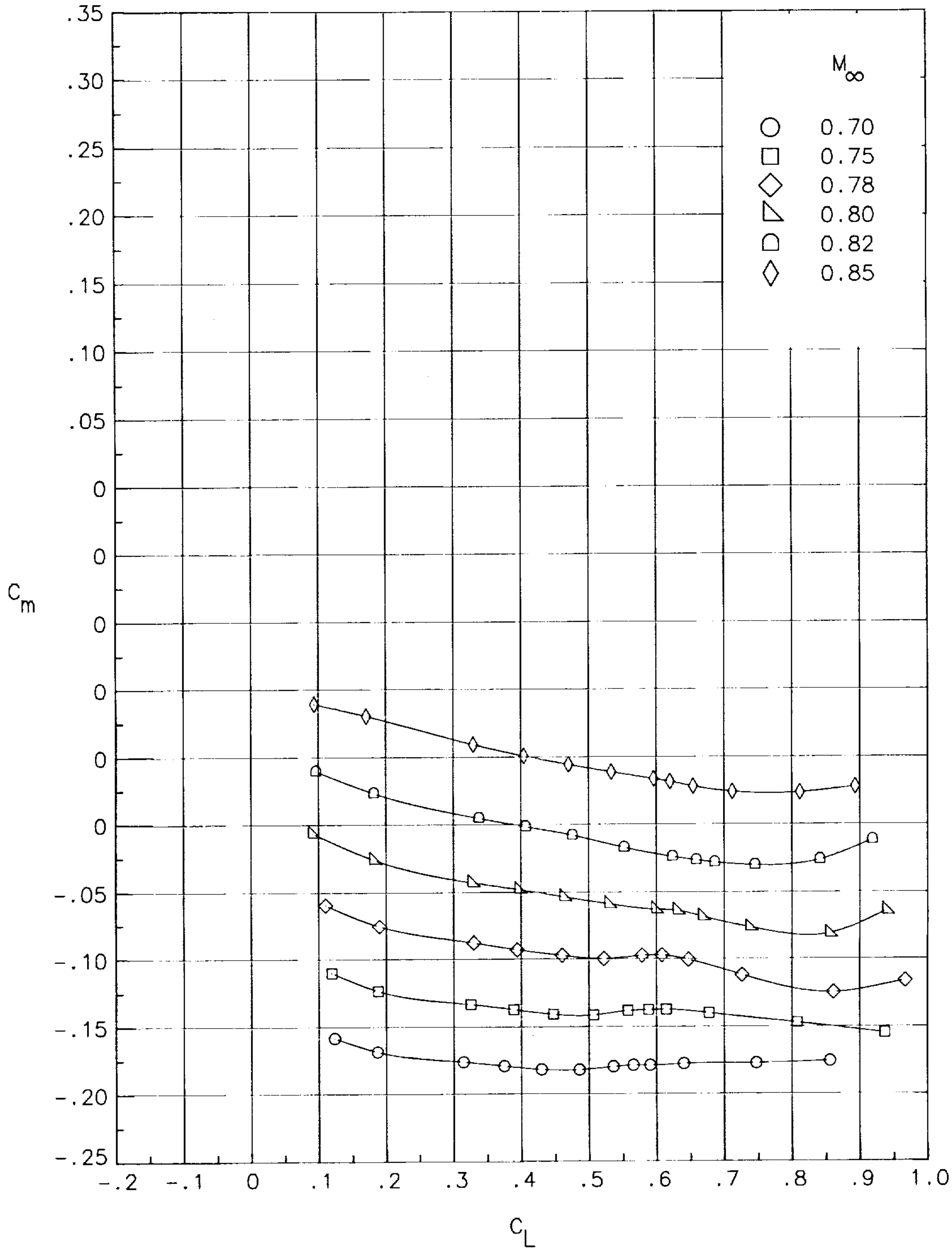

(c) Variation of pitching-moment coefficient with lift coefficient.
Figure 14. Continued.

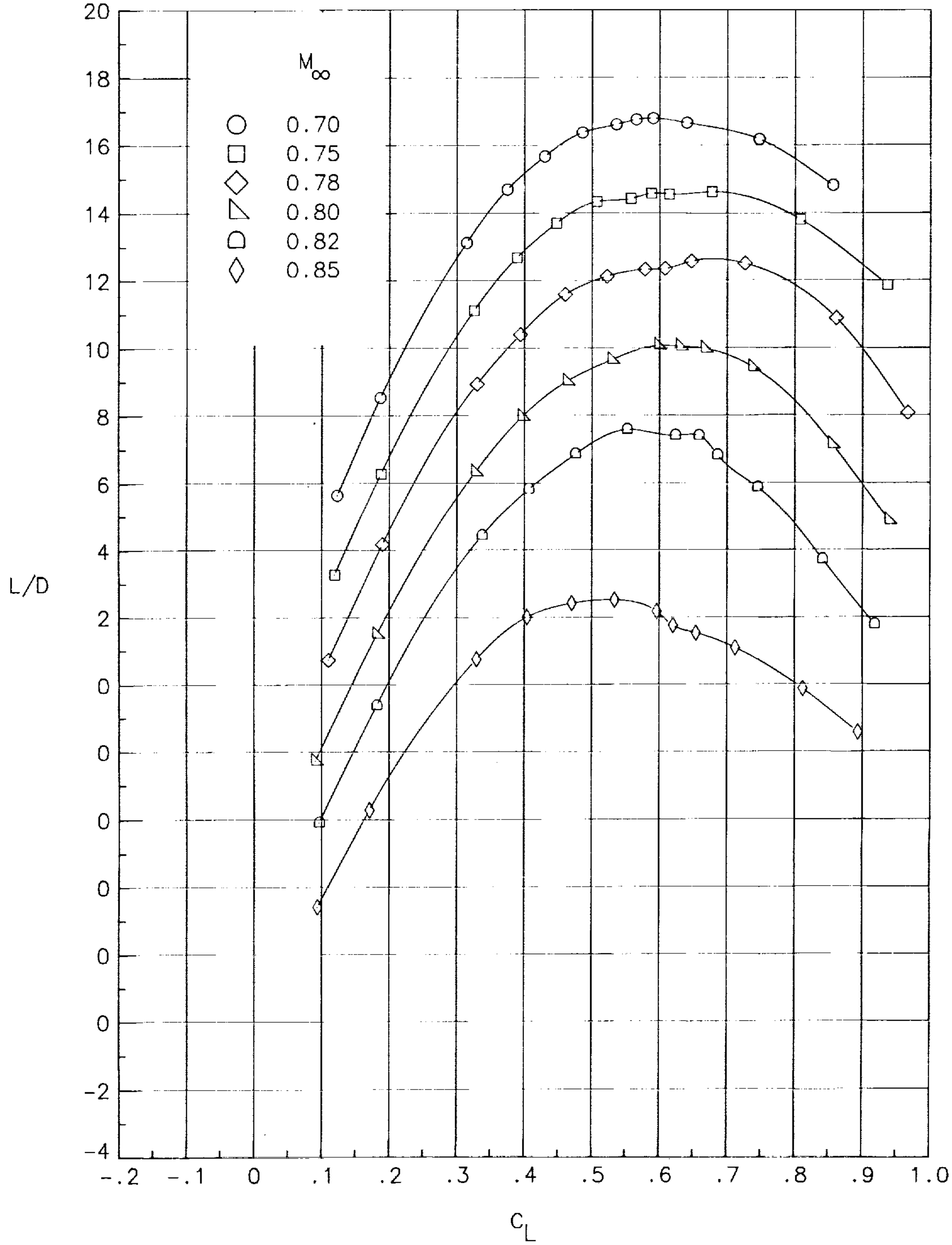

(d) Variation of lift-drag ratio with lift coefficient.

Figure 14. Concluded.

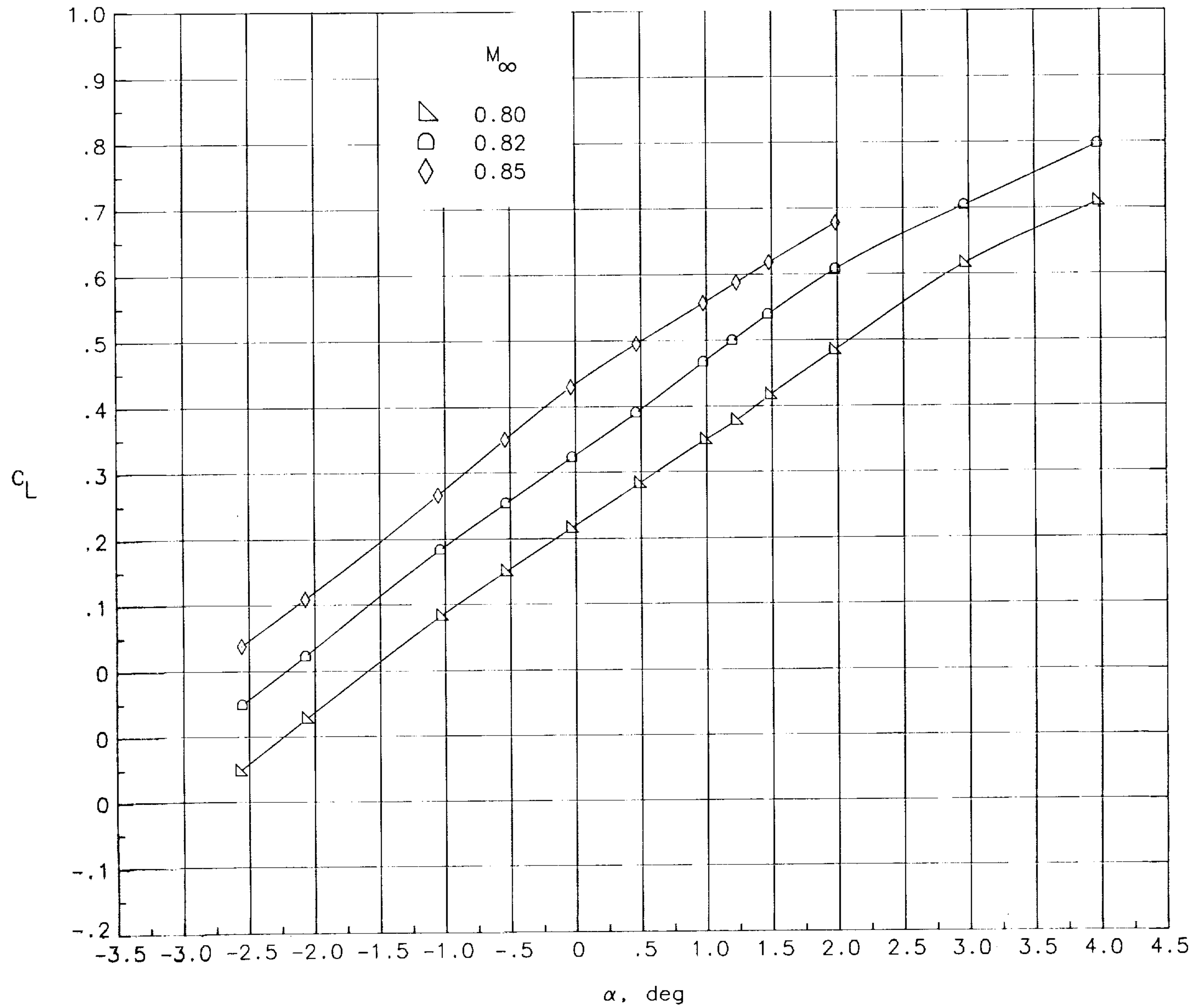

(a) Variation of lift coefficient with angle of attack.

Figure 15. Longitudinal aerodynamic characteristics for wing-body configuration with 2° toed-in D-nacelles at $x/c = 0.736$ and $\eta = 0.328$ and with long-cone antishock bodies at FS 31.2.

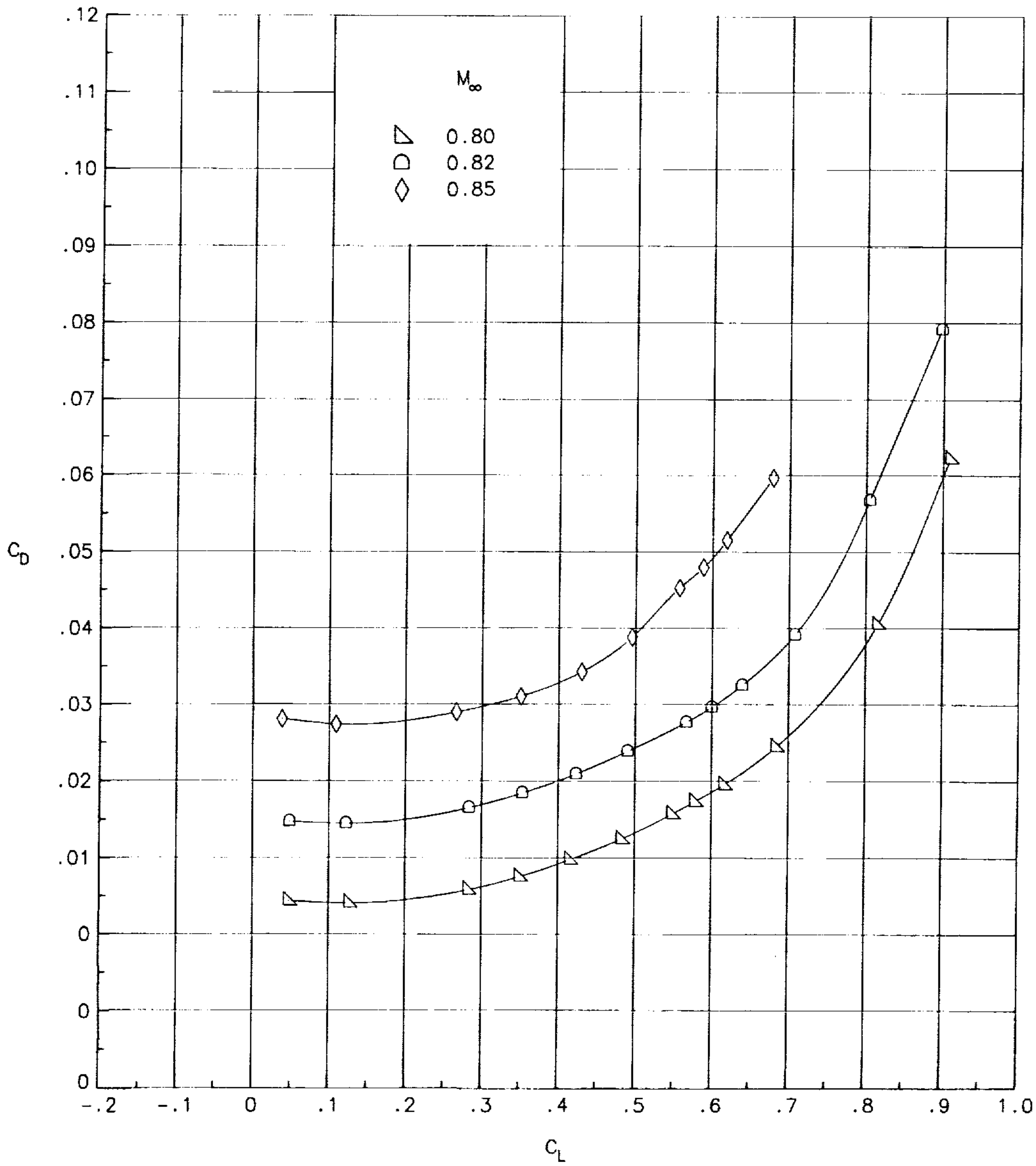

(b) Variation of drag coefficient with lift coefficient.

Figure 15. Continued.

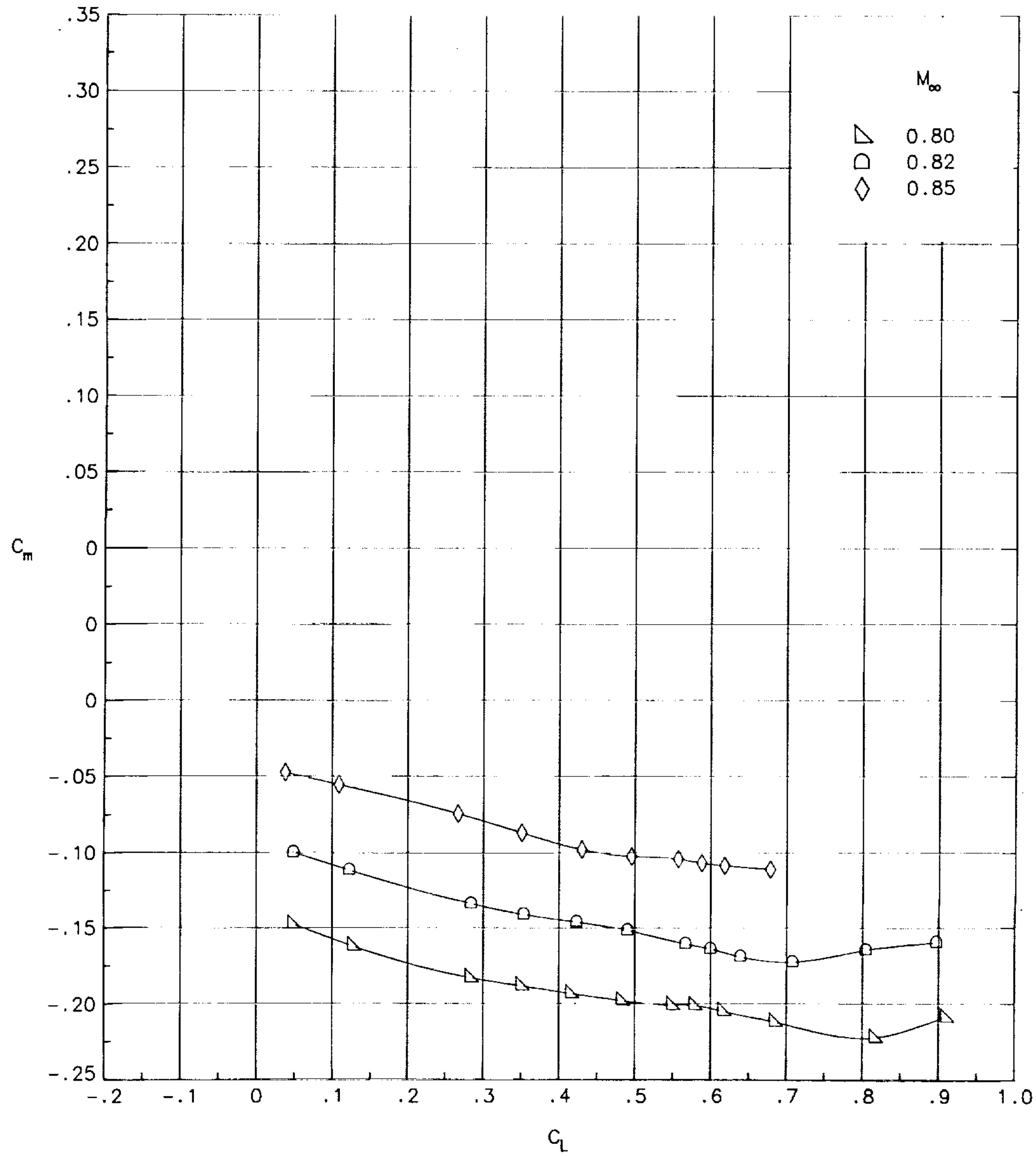

(c) Variation of pitching-moment coefficient with lift coefficient.

Figure 15. Continued.

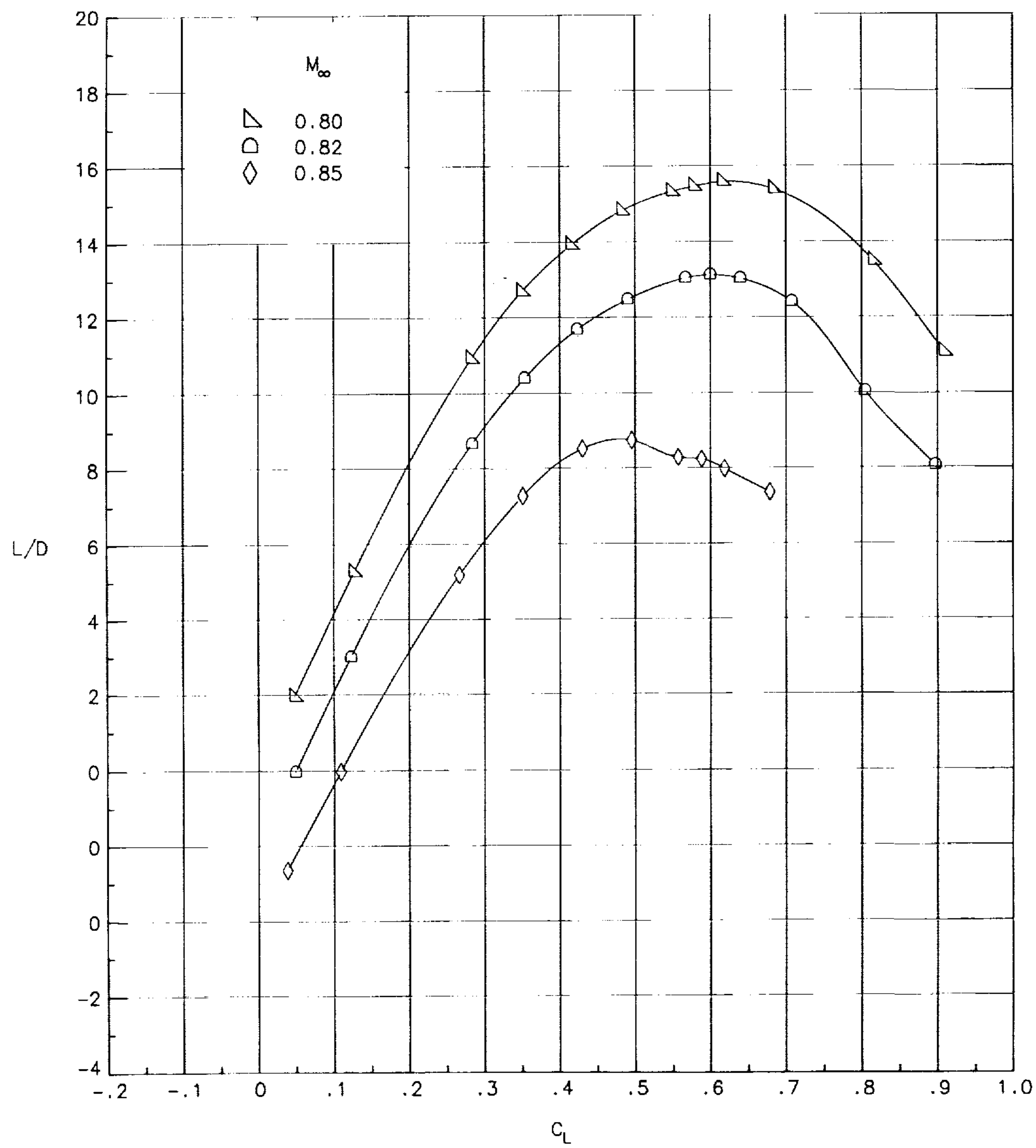

(d) Variation of lift-drag ratio with lift coefficient.

Figure 15. Concluded.

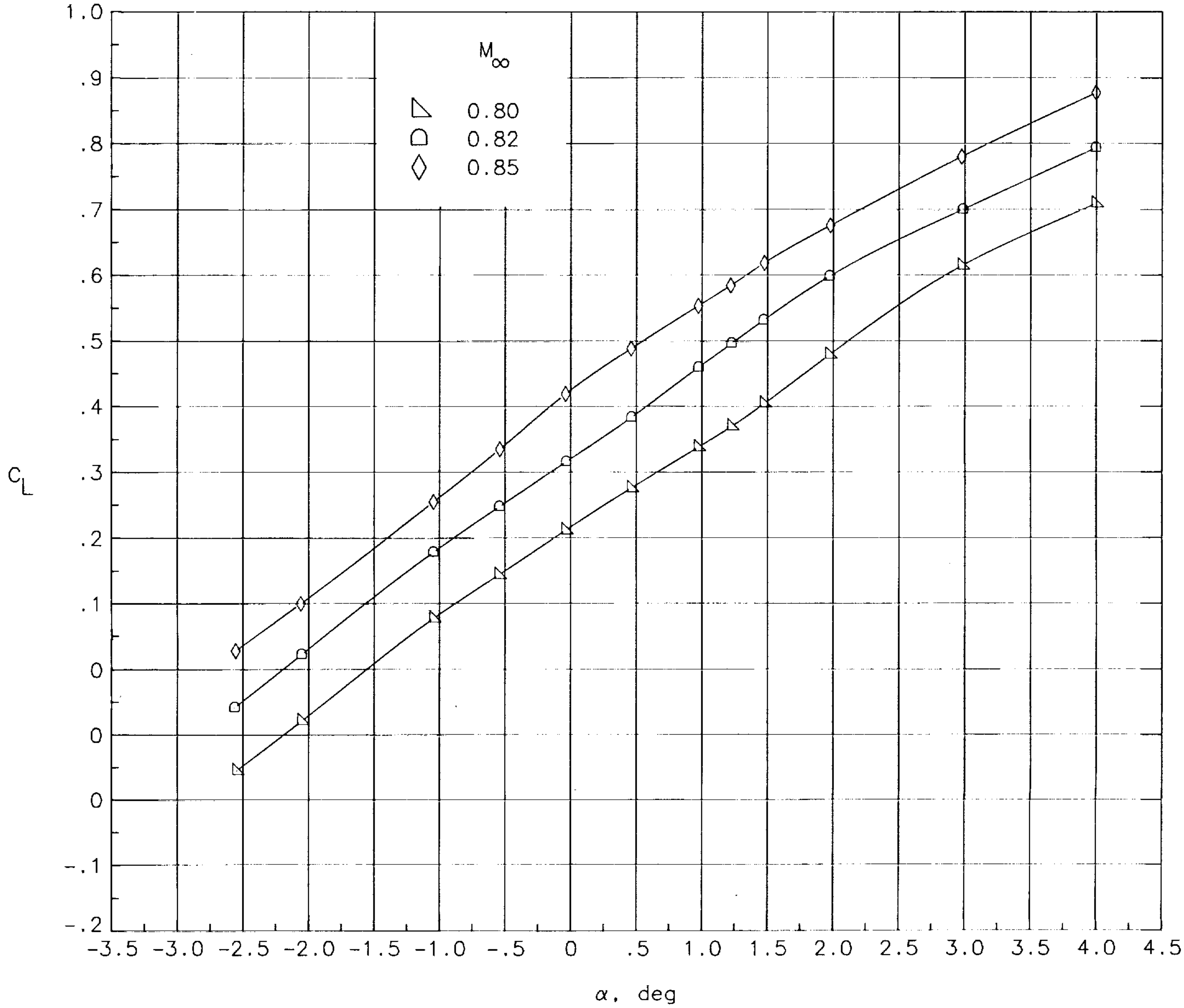

(a) Variation of lift coefficient with angle of attack.

Figure 16. Longitudinal aerodynamic characteristics for wing-body configuration with 2° toed-in D-nacelles at $x/c = 0.736$ and $\eta = 0.328$ and with long-cone antishock bodies at FS 30.2.

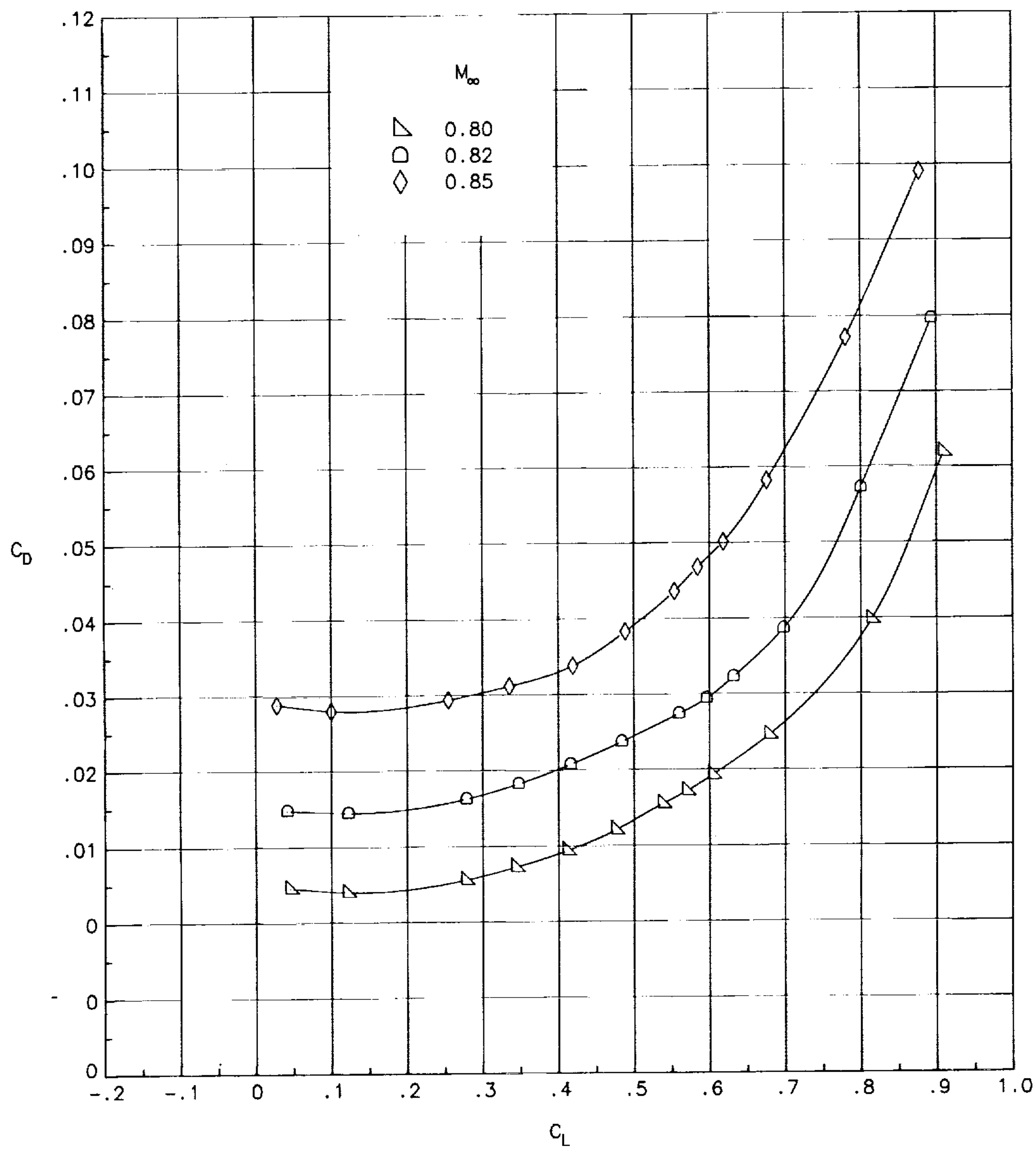

(b) Variation of drag coefficient with lift coefficient.

Figure 16. Continued.

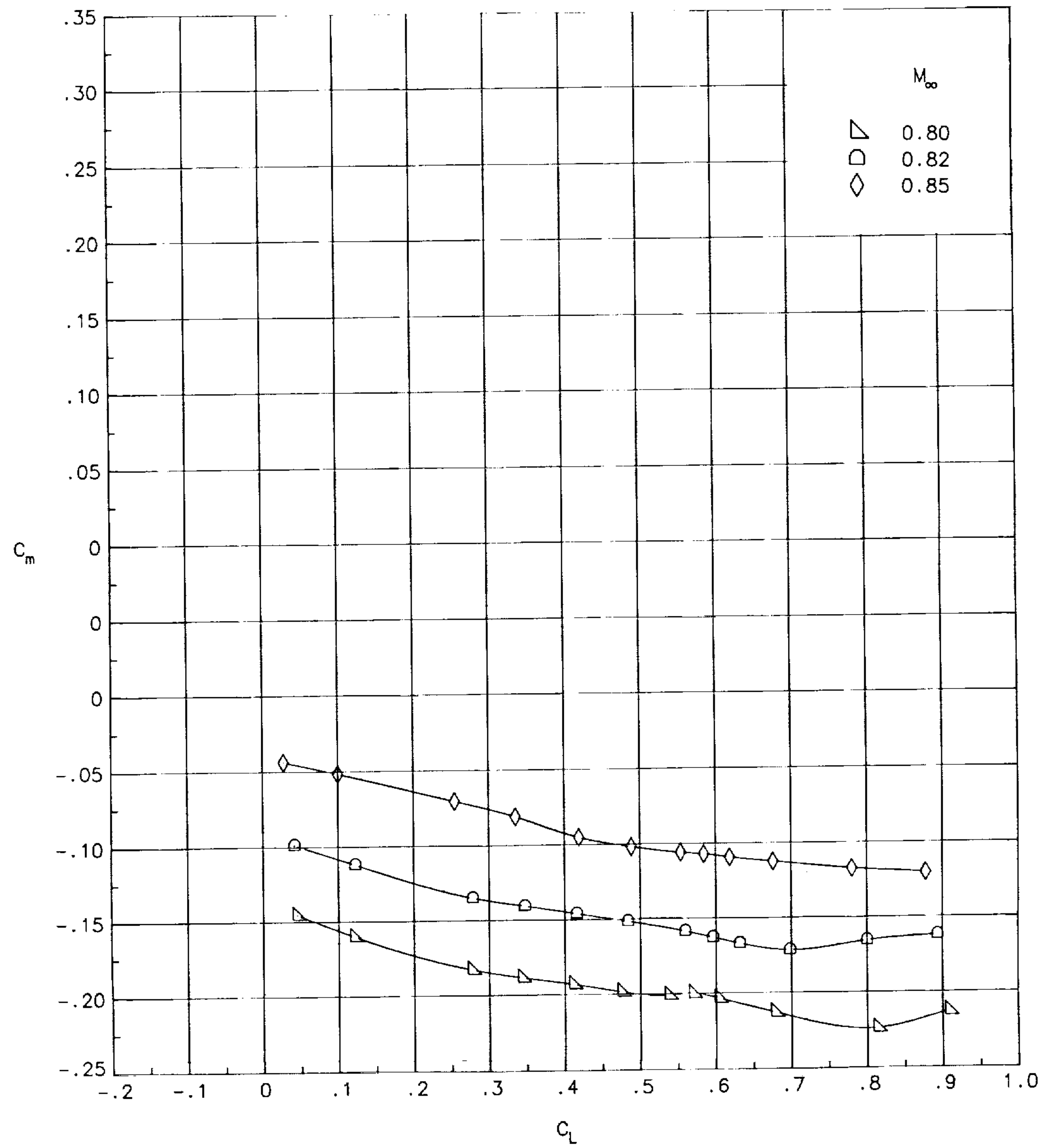

(c) Variation of pitching-moment coefficient with lift coefficient.

Figure 16. Continued.

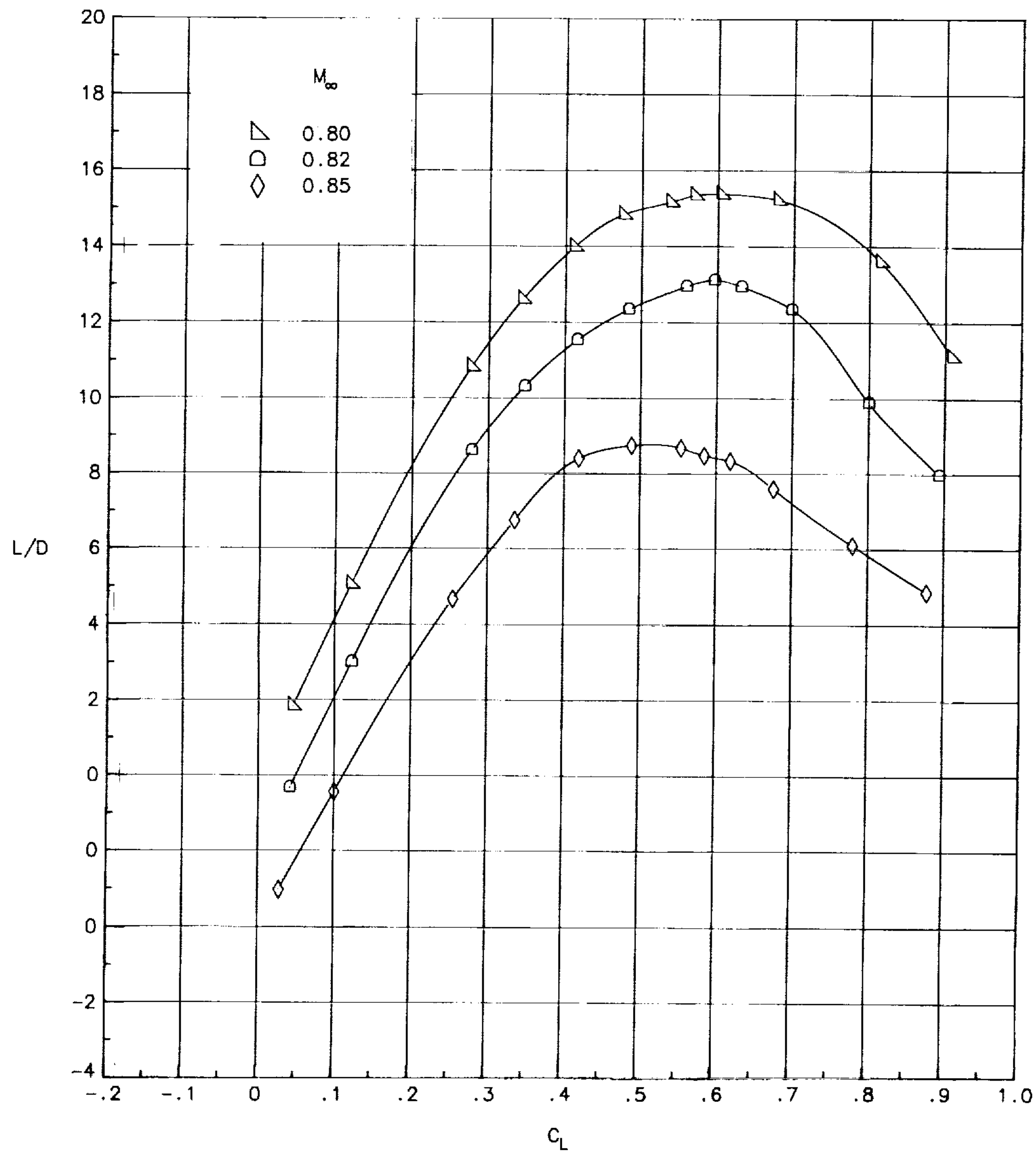

(d) Variation of lift-drag ratio with lift coefficient.

Figure 16. Concluded.

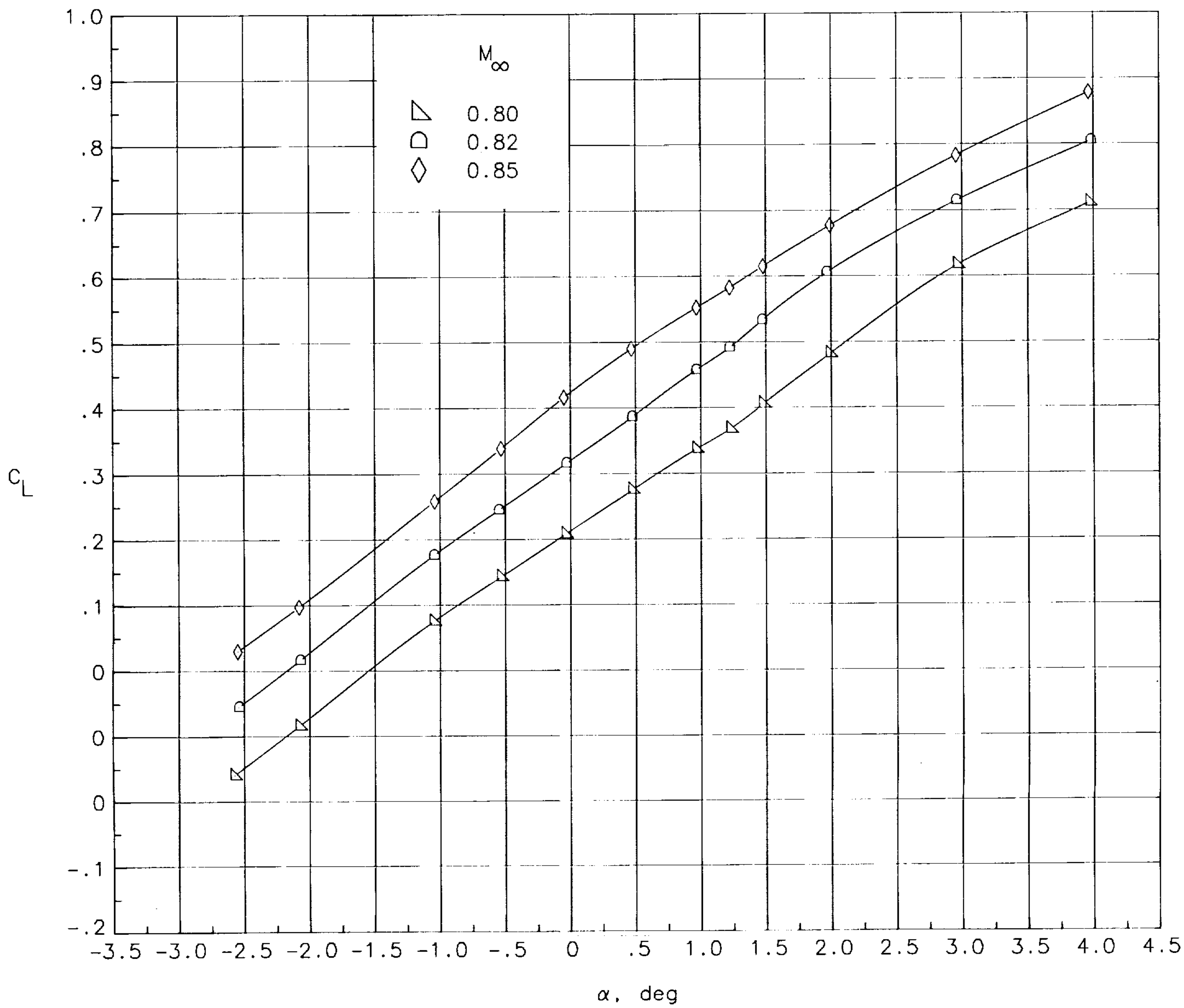

(a) Variation of lift coefficient with angle of attack.

Figure 17. Longitudinal aerodynamic characteristics for wing-body configuration with 2° toed-in D-nacelles at $x/c = 0.736$ and $\eta = 0.328$ and with long-cone antishock bodies at FS 30.2 faired to nacelle exits.

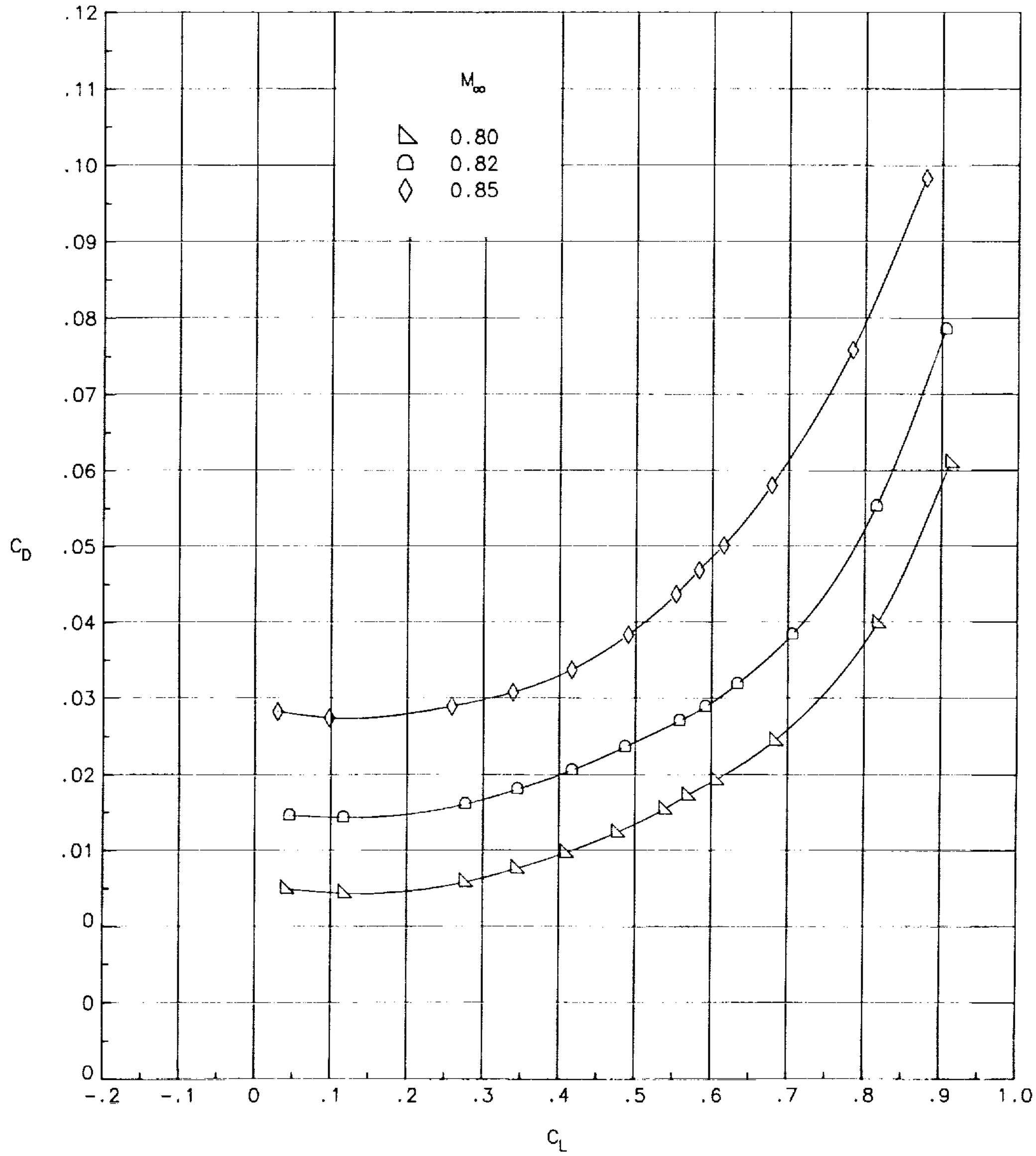

(b) Variation of drag coefficient with lift coefficient.

Figure 17. Continued.

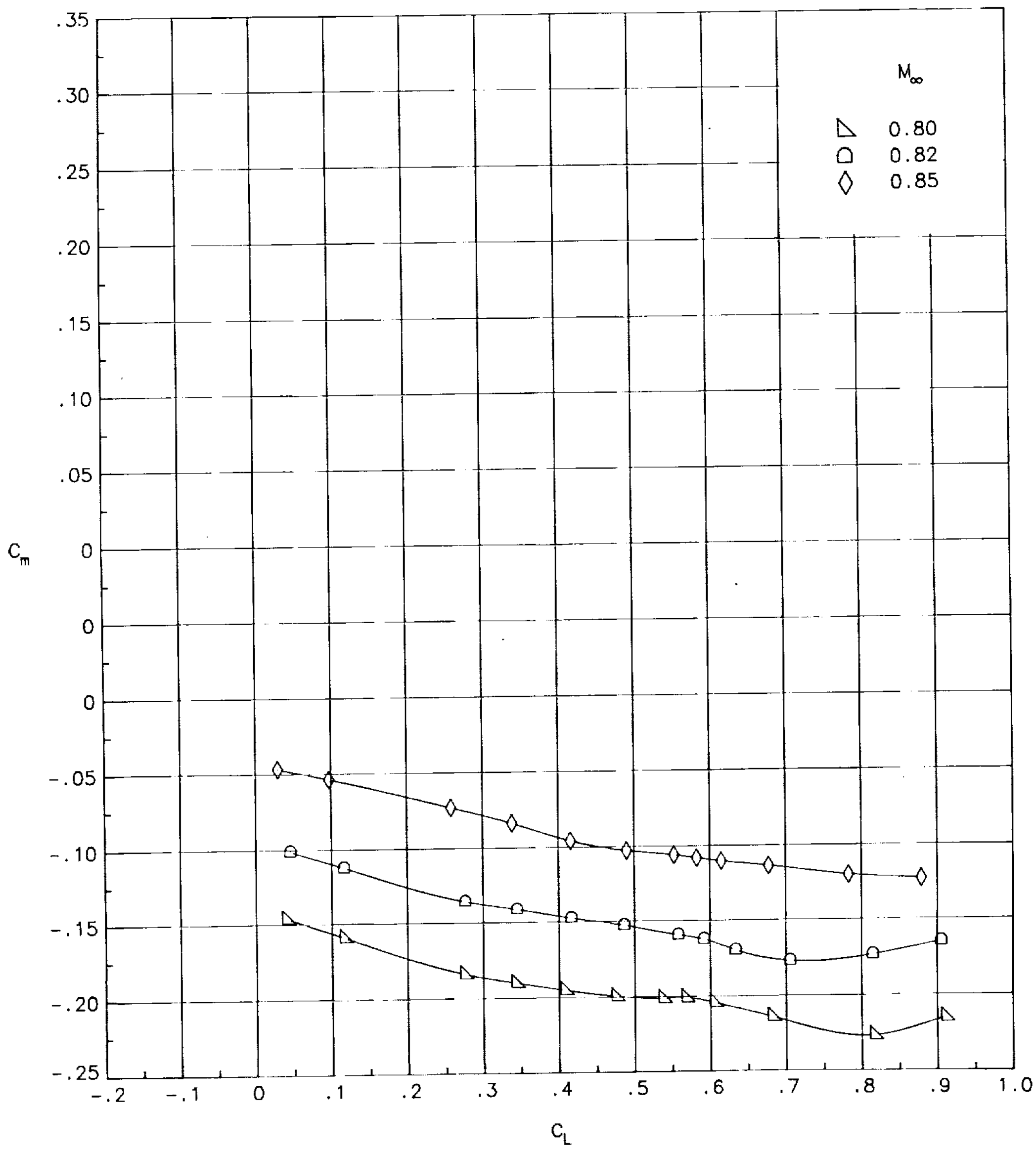

(c) Variation of pitching-moment coefficient with lift coefficient.

Figure 17. Continued.

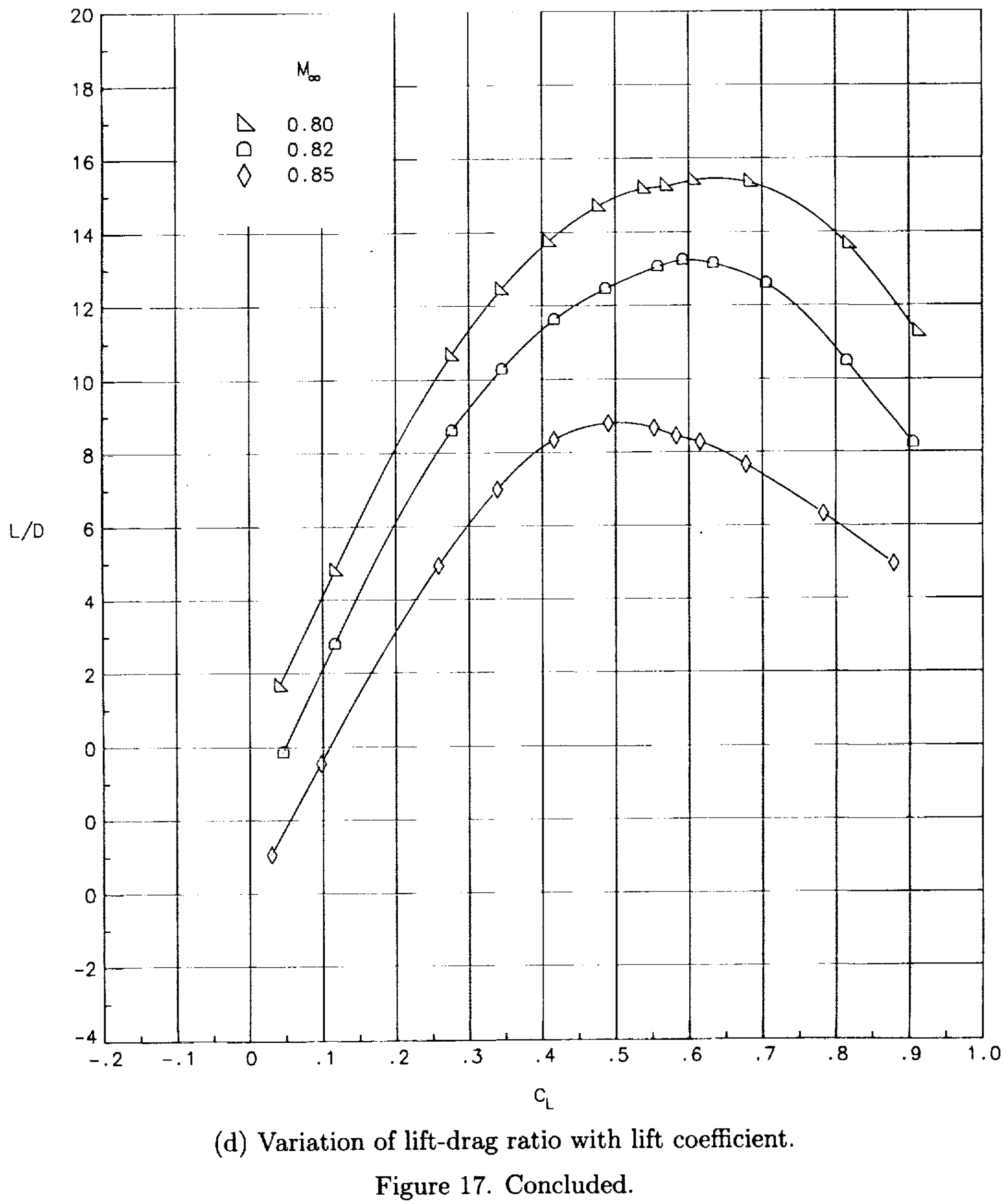

(d) Variation of lift-drag ratio with lift coefficient.

Figure 17. Concluded.

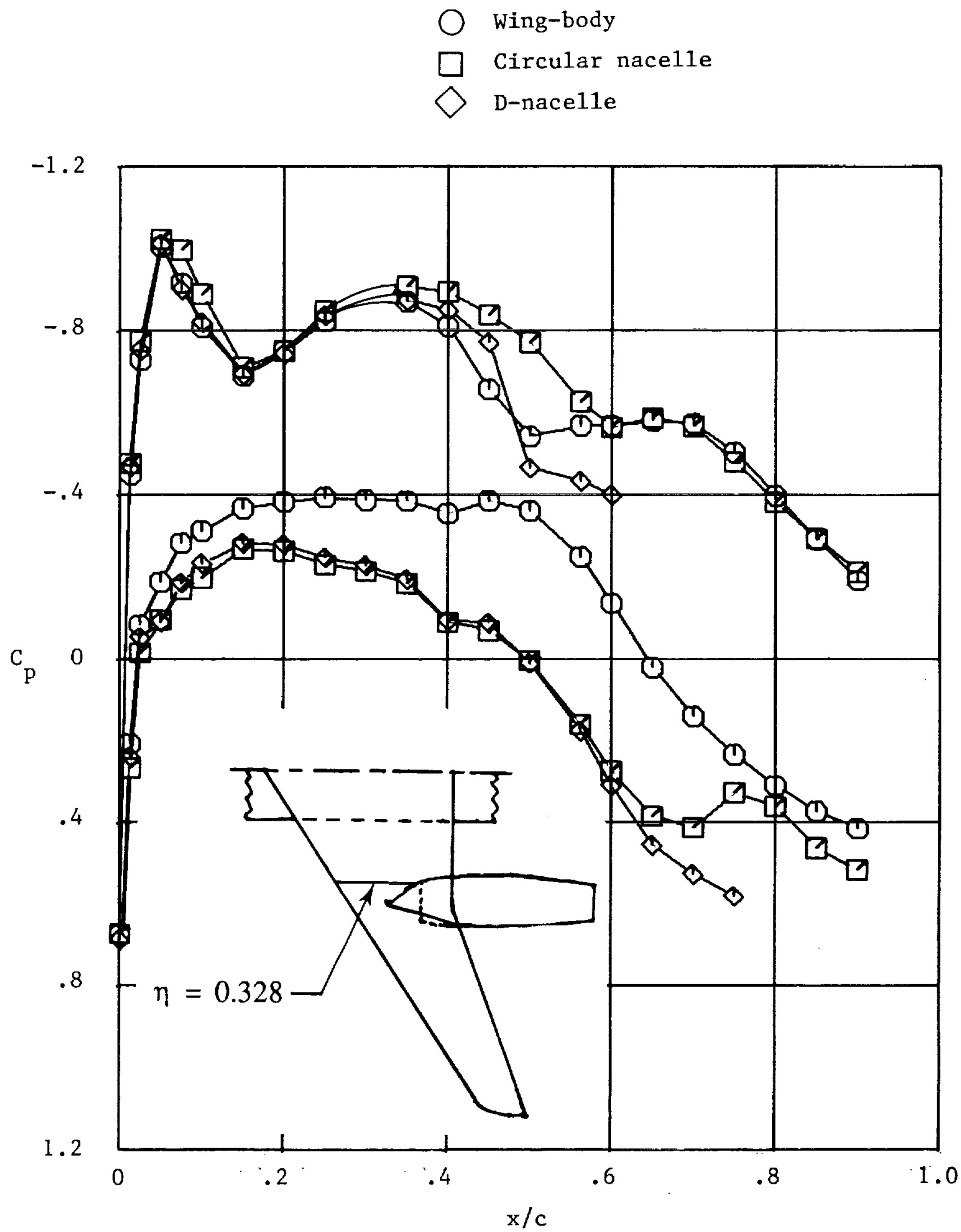

(a) $\eta = 0.328$.

Figure 18. Effect of aft-mounted nacelles on wing chordwise pressure-coefficient distributions.

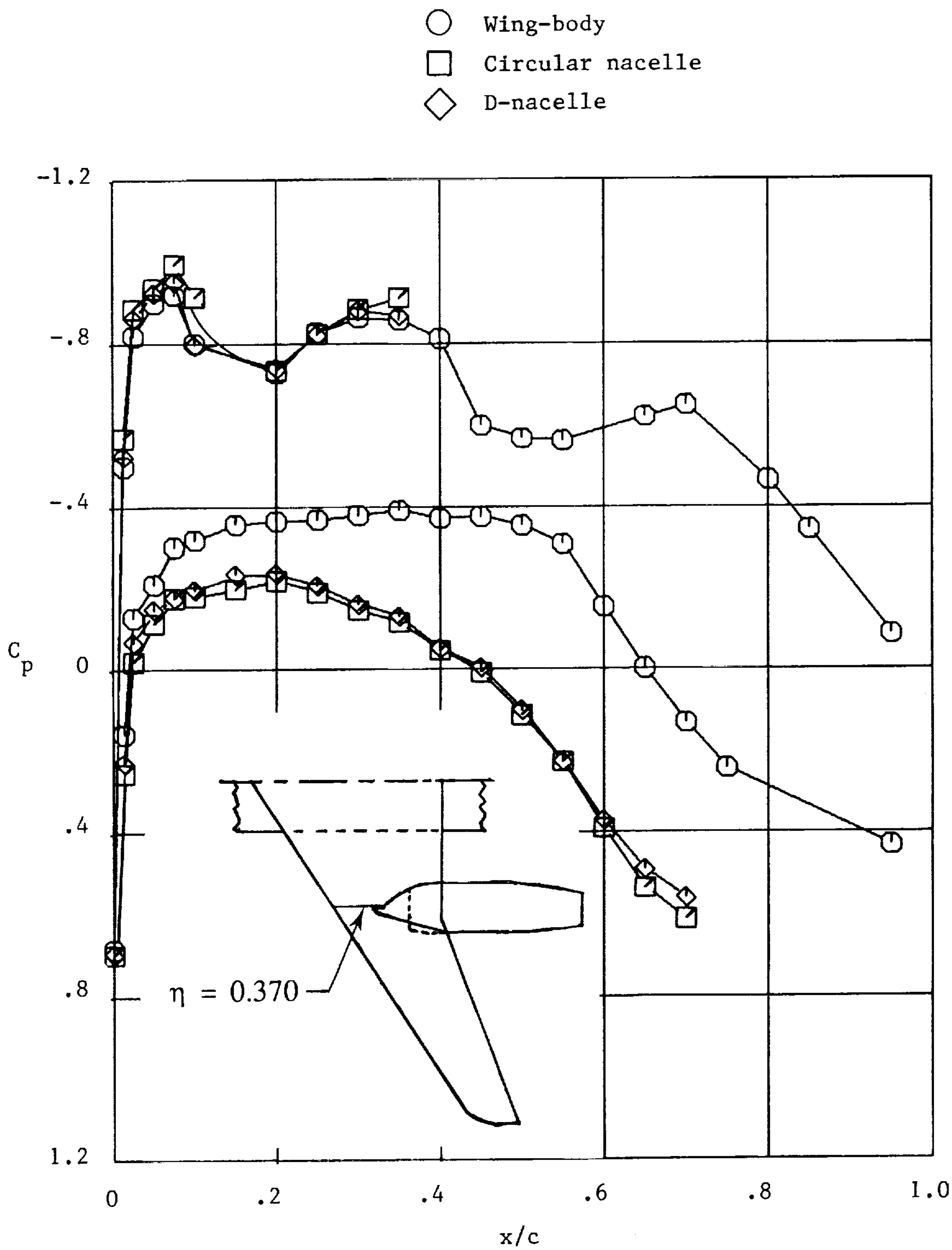

(b) $\eta = 0.370$.

Figure 18. Continued.

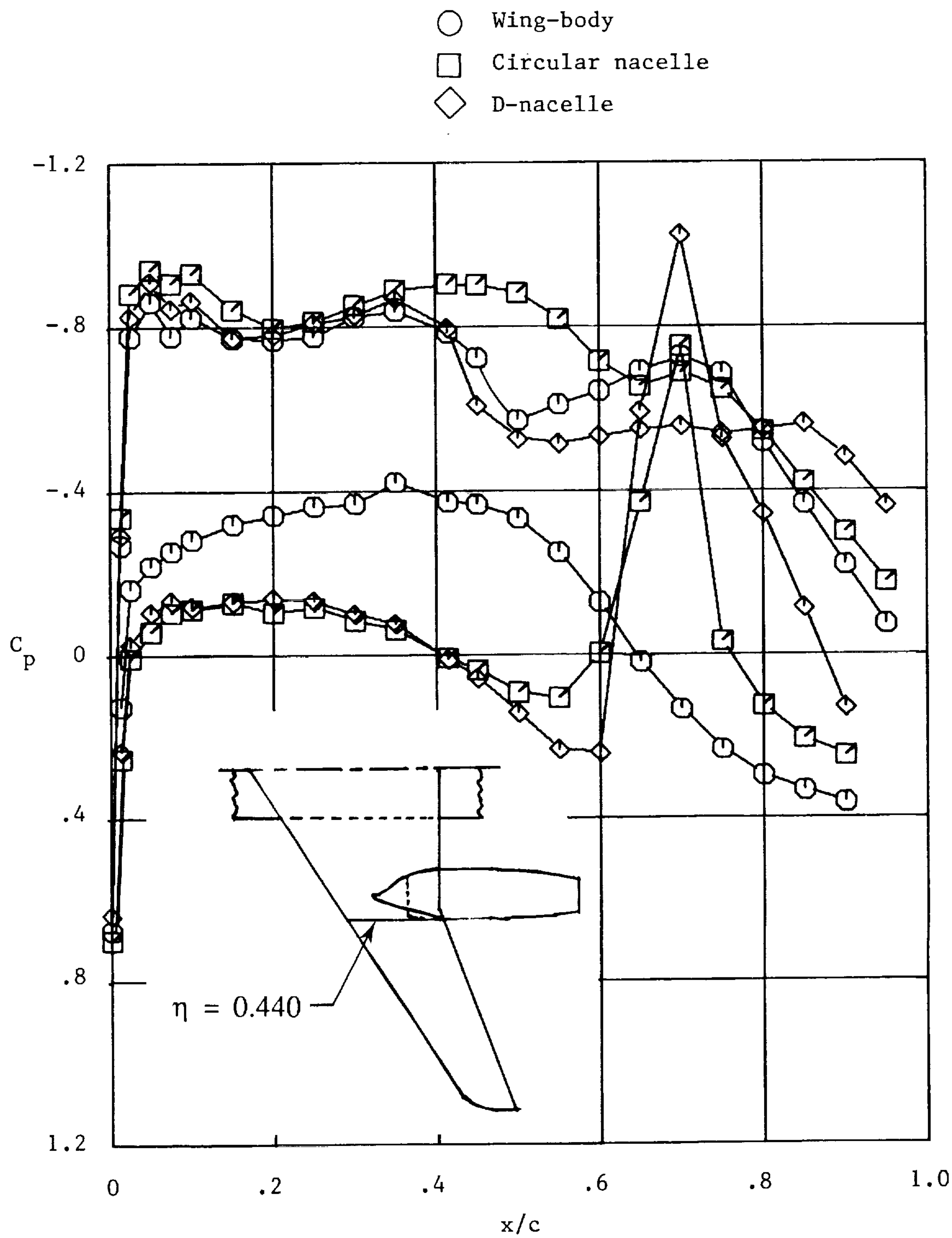

(c) $\eta = 0.440$.

Figure 18. Concluded.

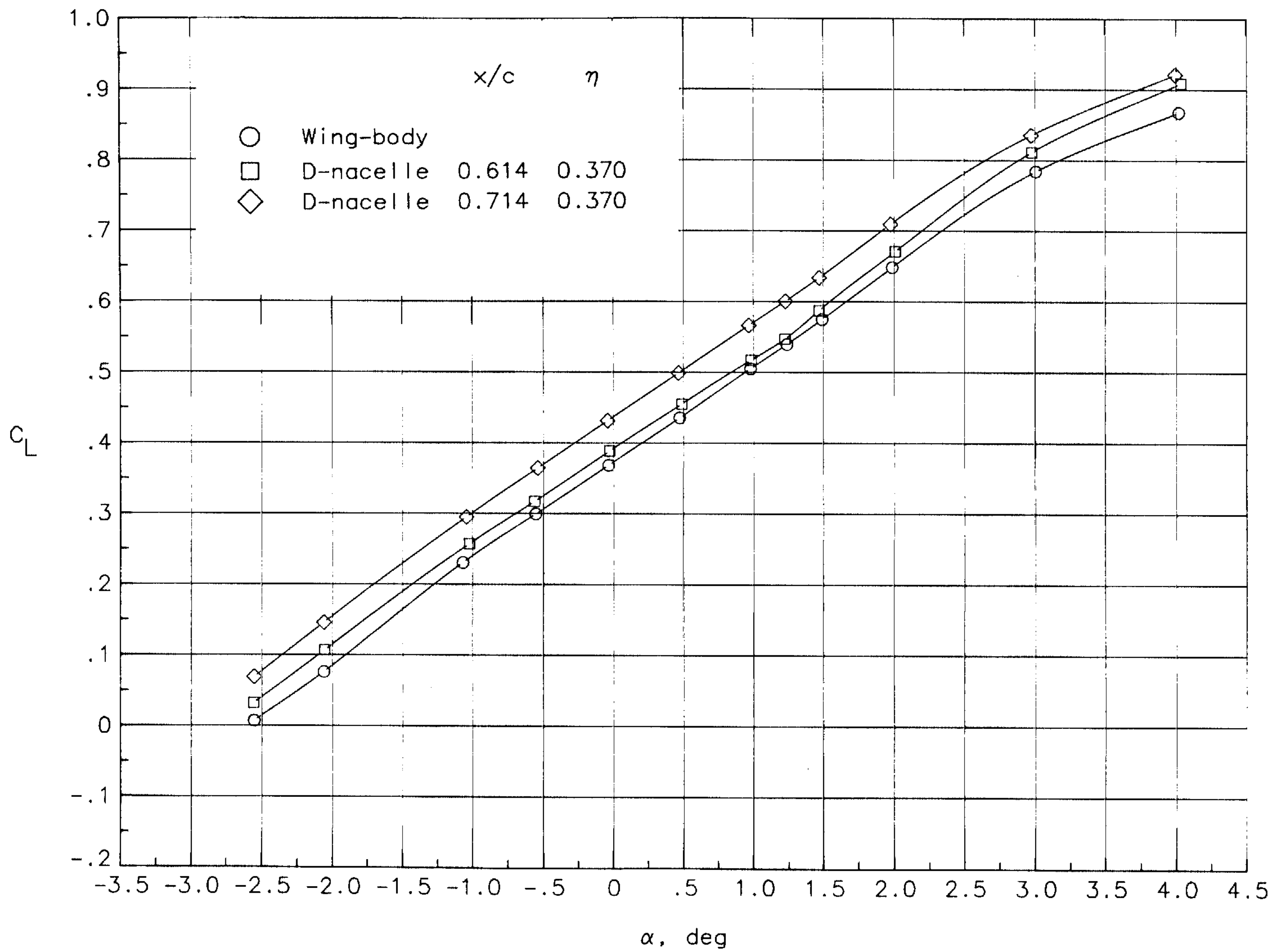

(a) Variation of lift coefficient with angle of attack.

Figure 19. Effect of D-nacelle chordwise location. $M_\infty = 0.80$.

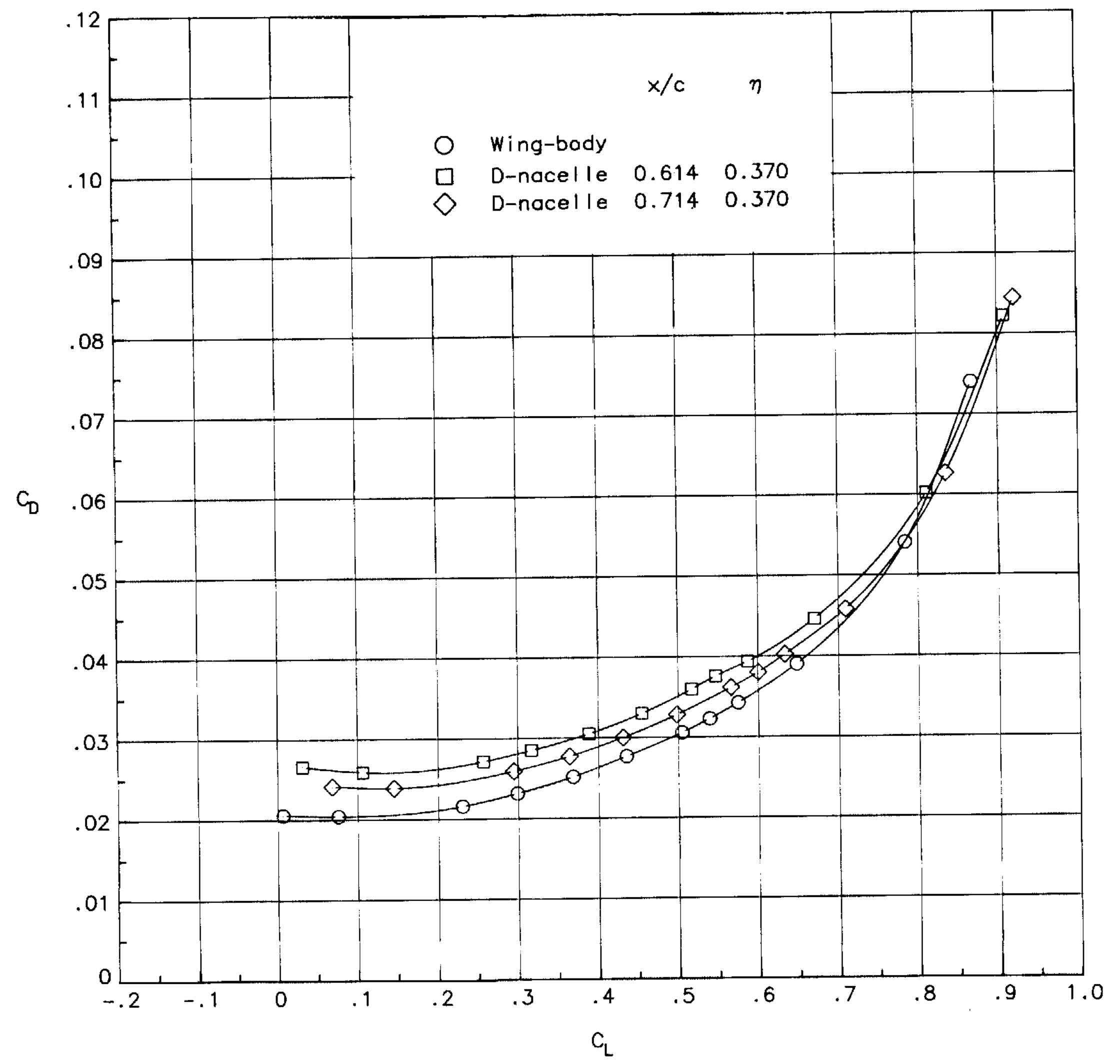

(b) Variation of drag coefficient with lift coefficient.

Figure 19. Continued.

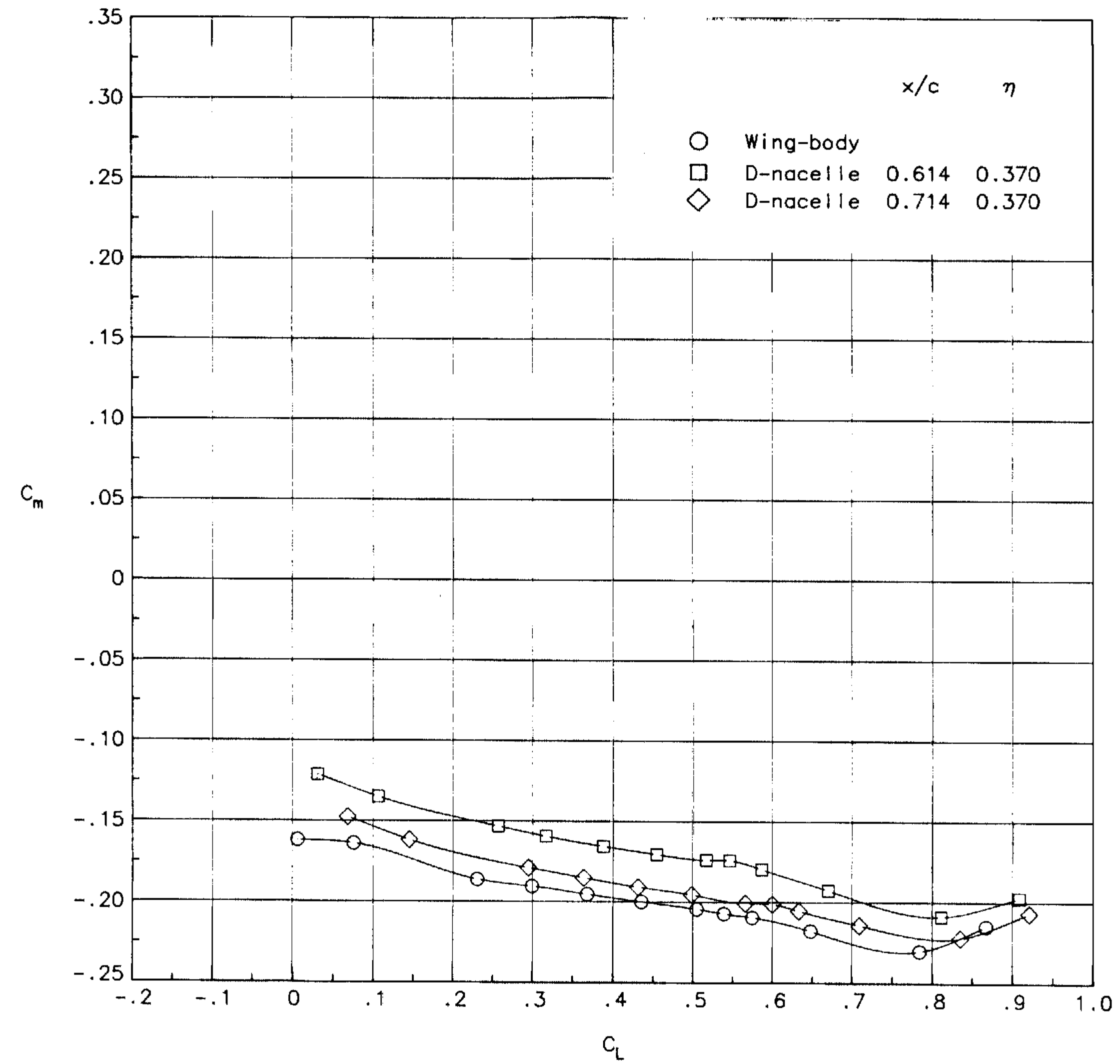

(c) Variation of pitching-moment coefficient with lift coefficient.

Figure 19. Continued.

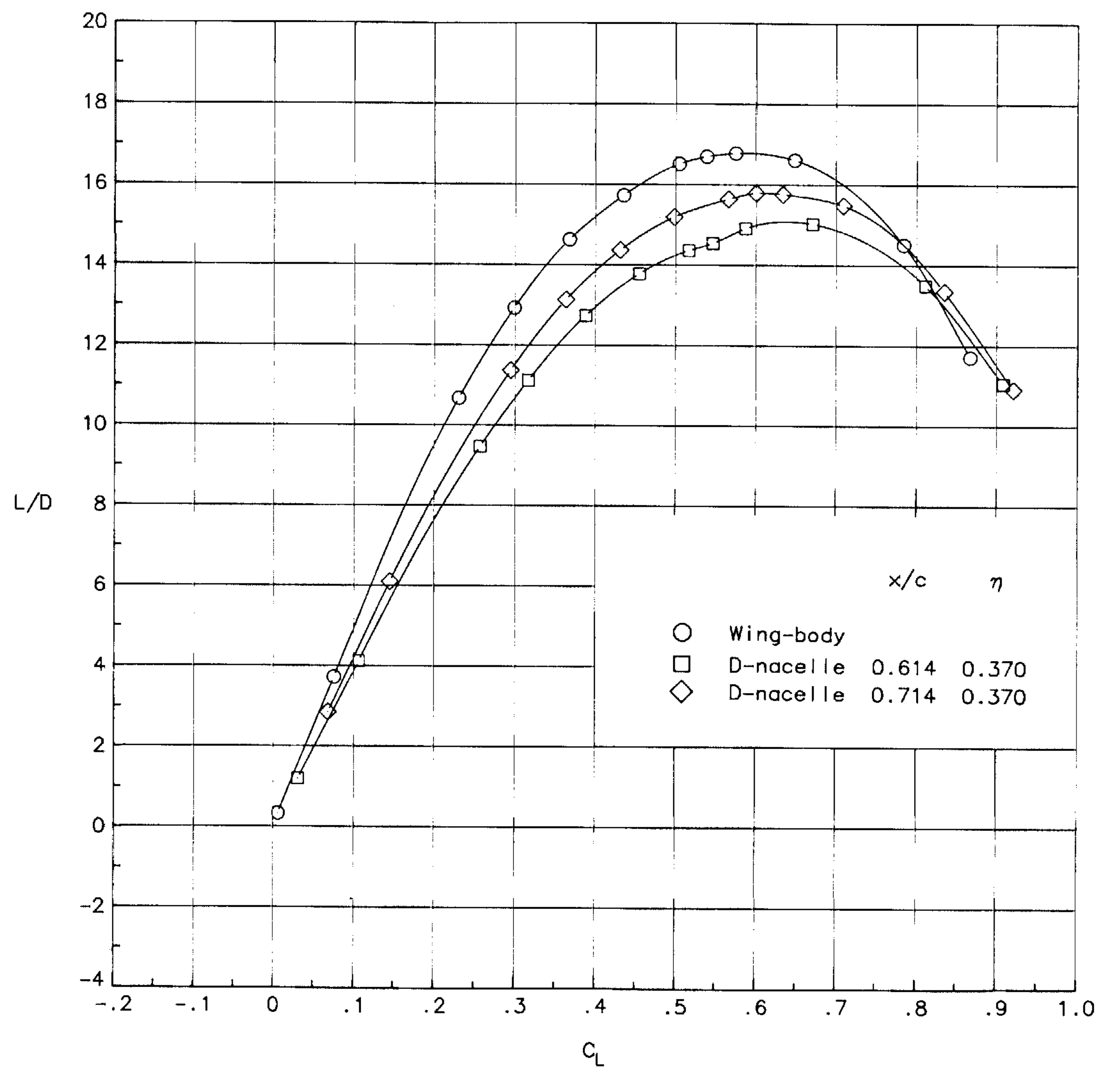

(d) Variation of lift-drag ratio with lift coefficient.

Figure 19. Concluded.

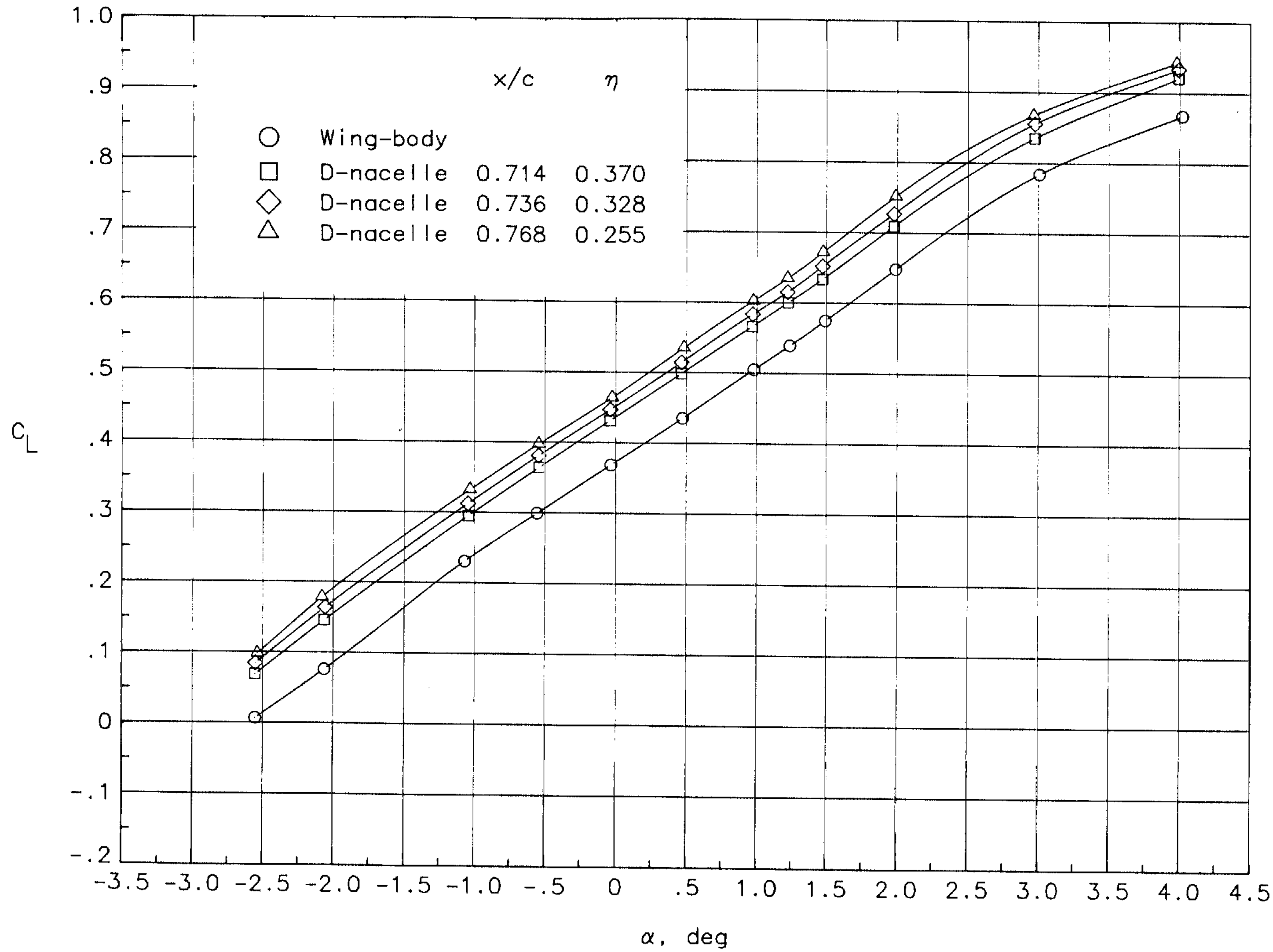

(a) Variation of lift coefficient with angle of attack.

Figure 20. Effect of D-nacelle spanwise location. $M_\infty = 0.80$.

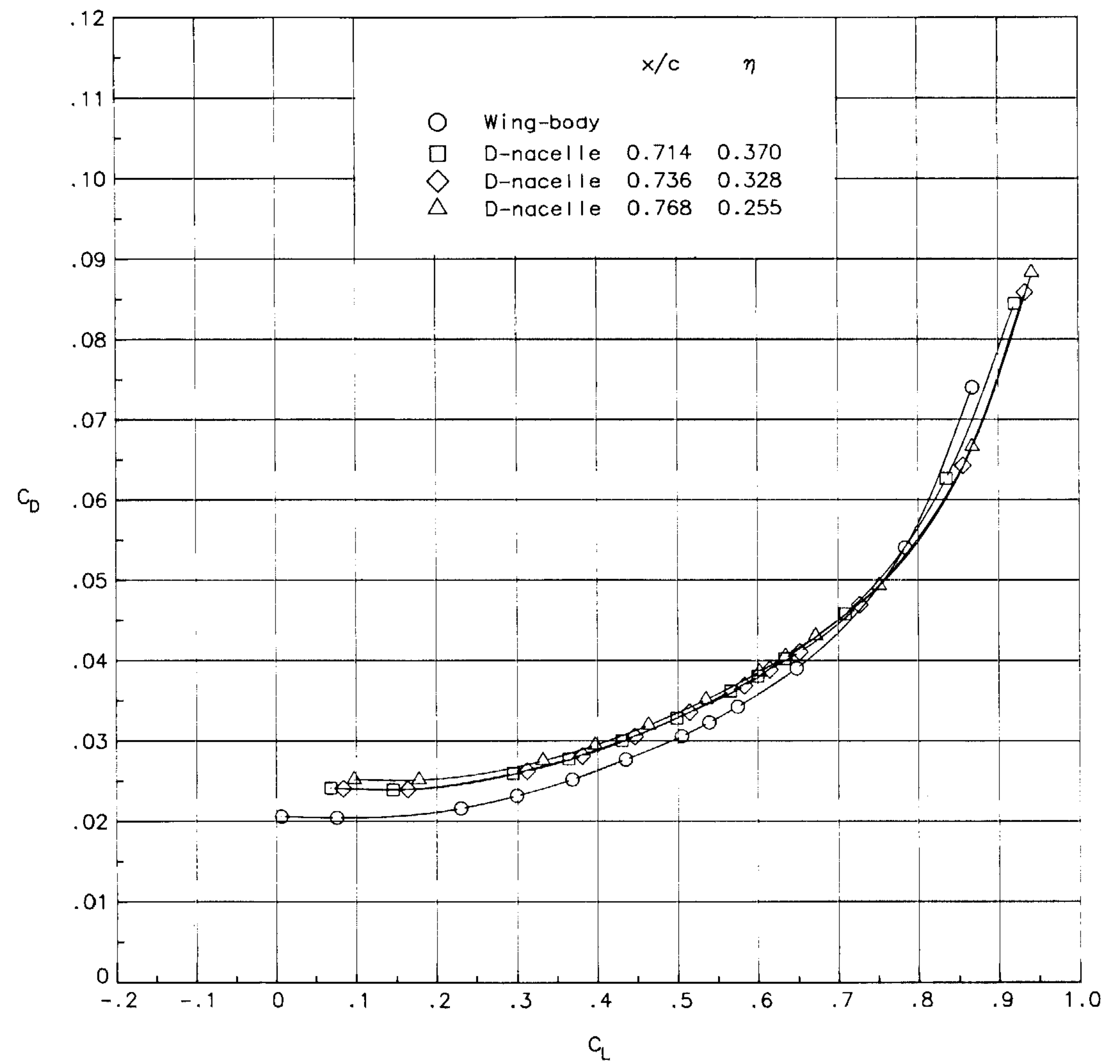

(b) Variation of drag coefficient with lift coefficient.

Figure 20. Continued.

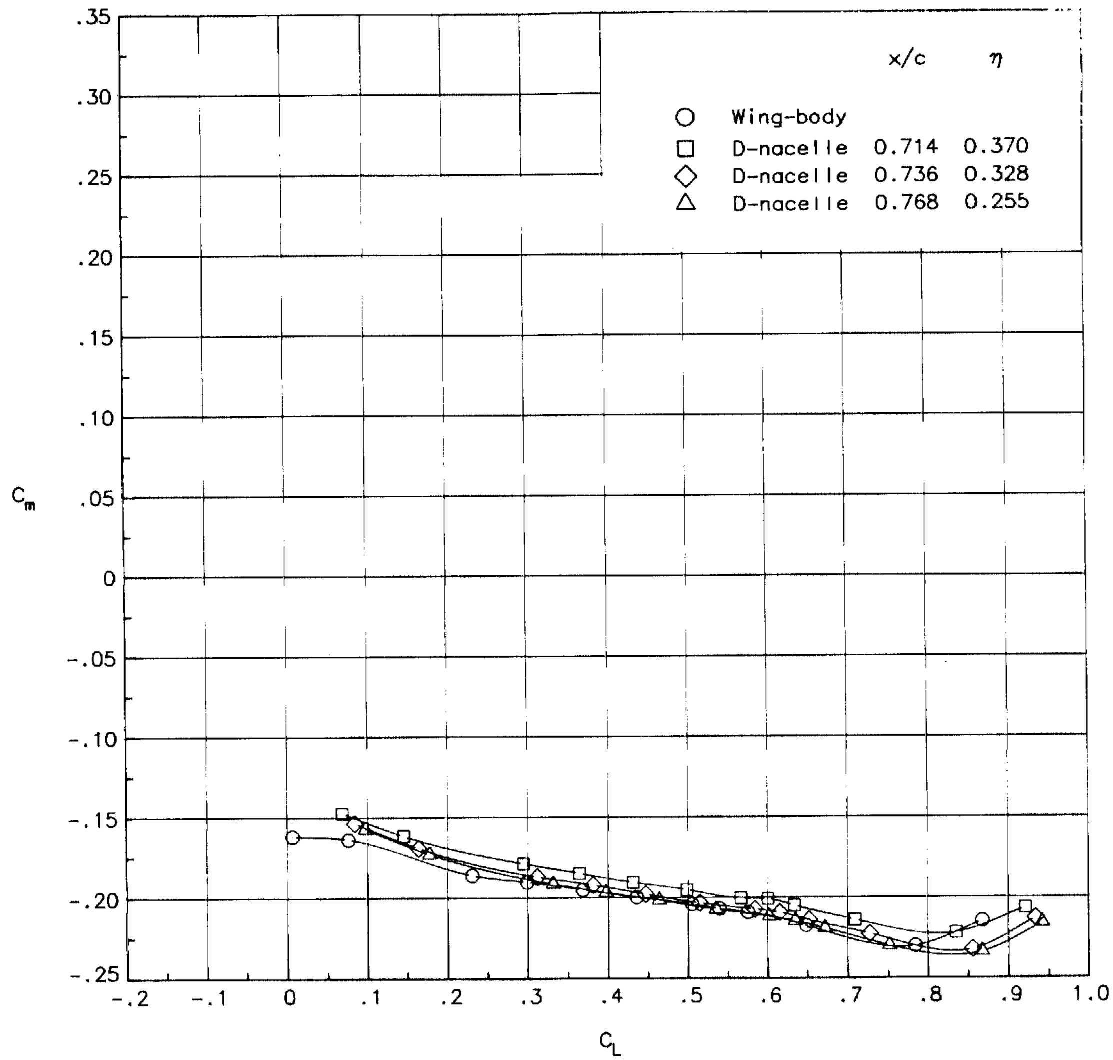

(c) Variation of pitching-moment coefficient with lift coefficient.

Figure 20. Continued.

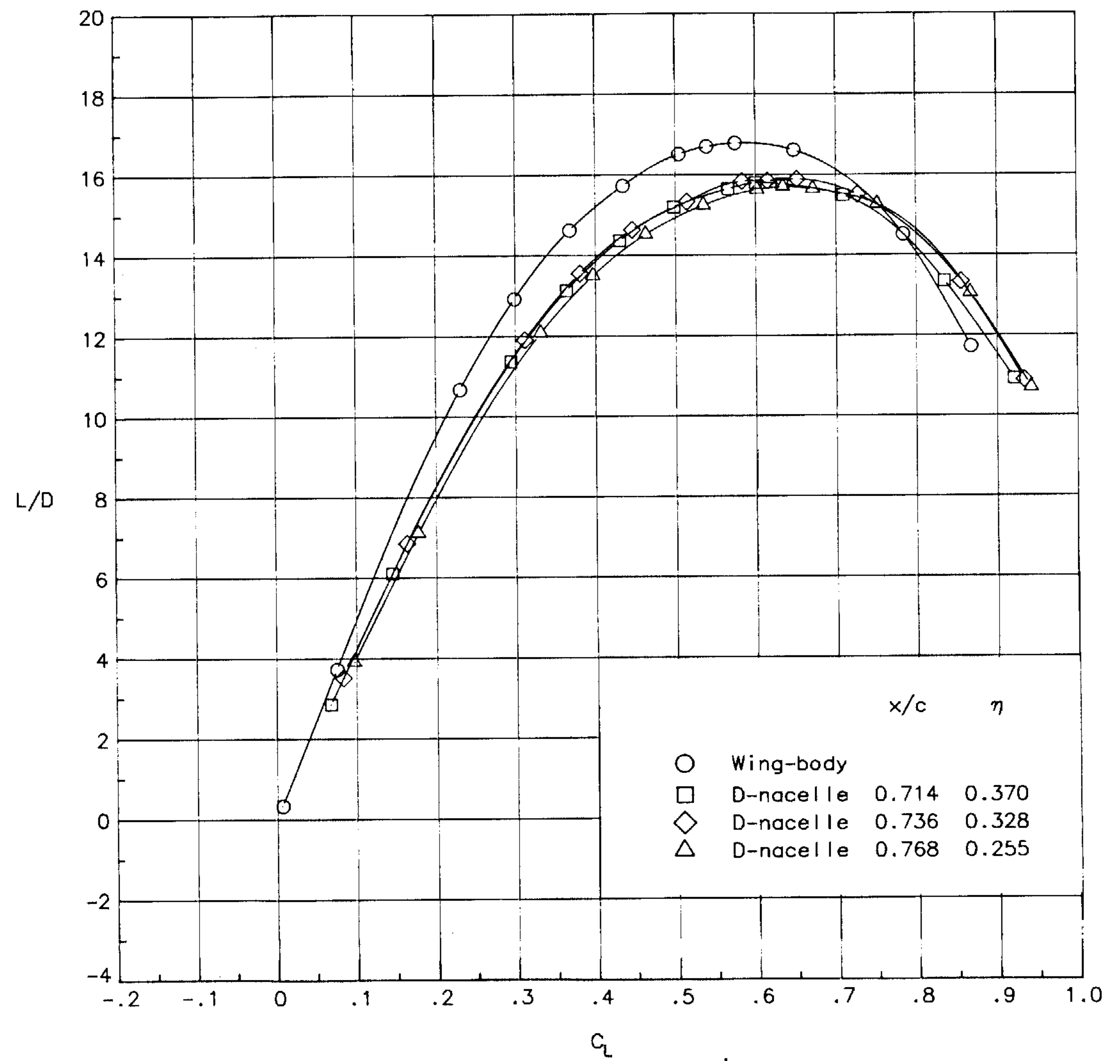

(d) Variation of lift-drag ratio with lift coefficient.

Figure 20. Concluded.

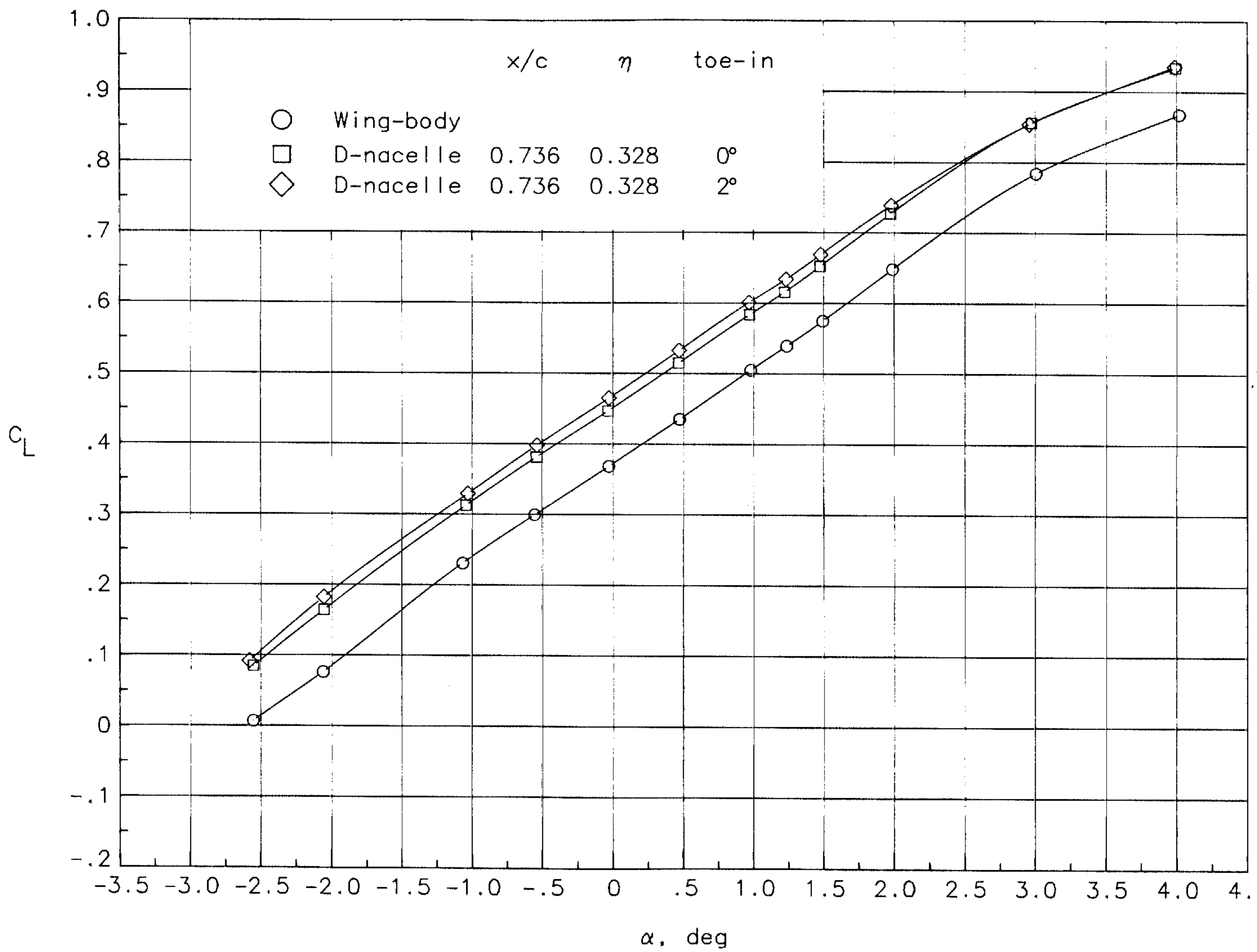

(a) Variation of lift coefficient with angle of attack.

Figure 21. Effect of D-nacelle toe-in. $M_\infty = 0.80$.

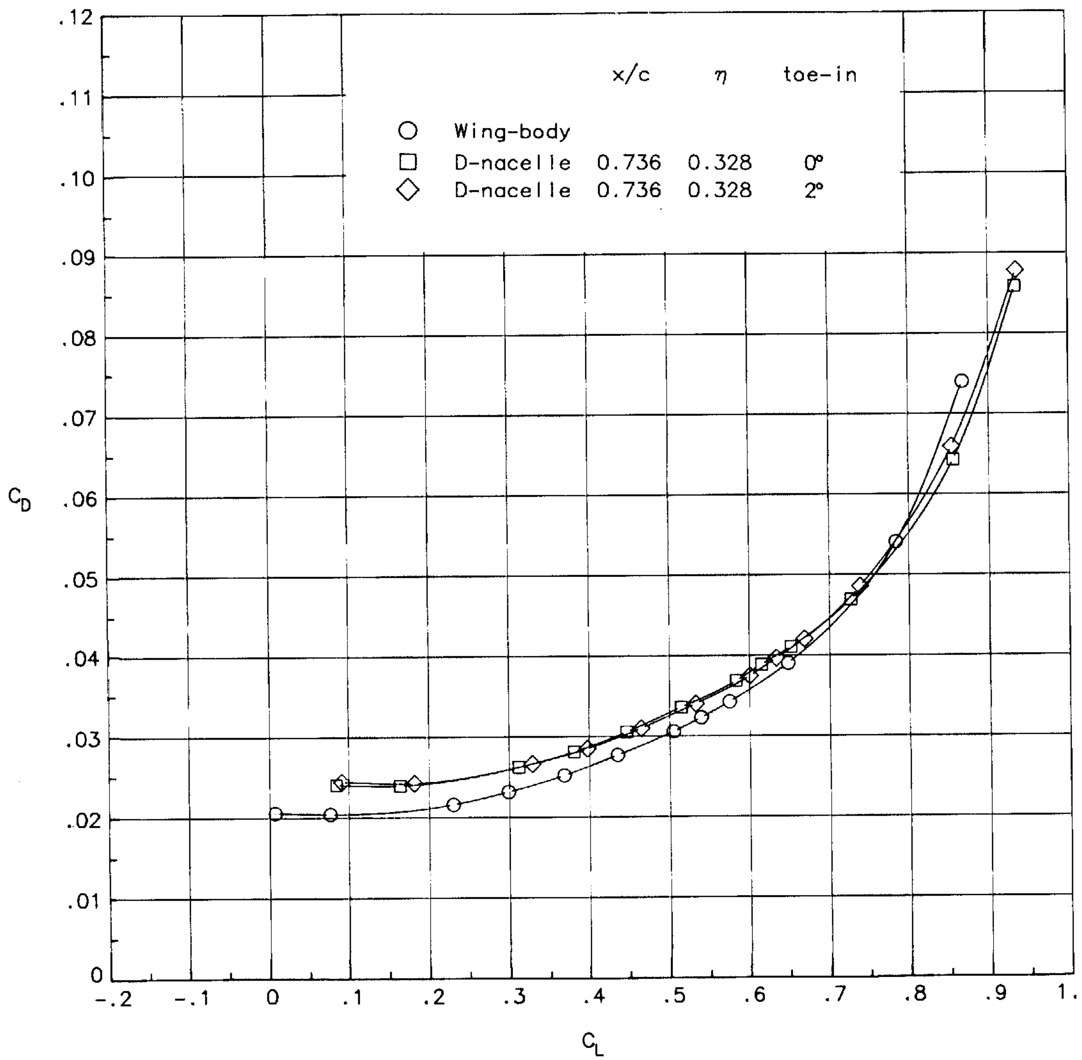

(b) Variation of drag coefficient with lift coefficient.

Figure 21. Continued.

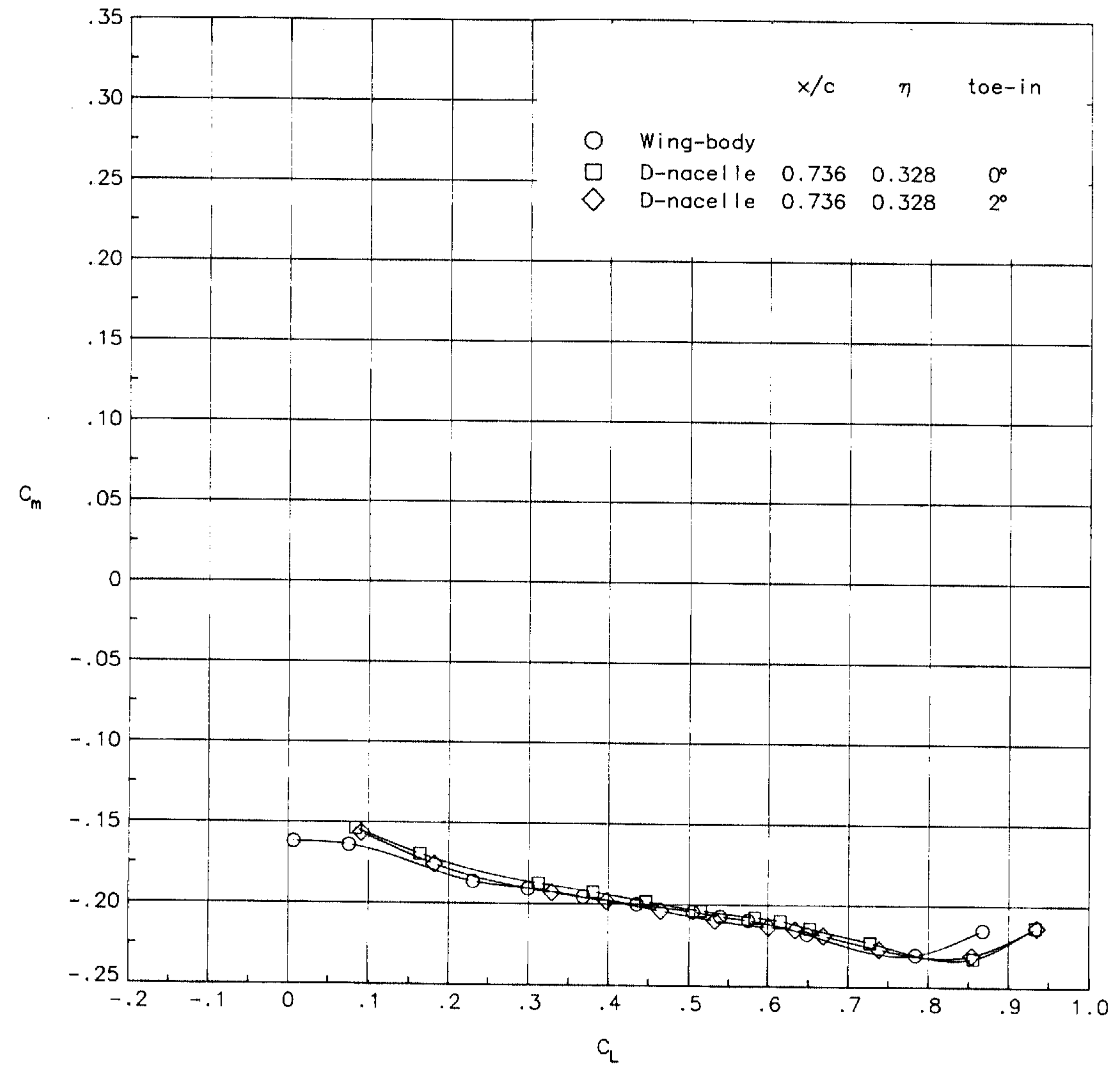

(c) Variation of pitching-moment coefficient with lift coefficient.

Figure 21. Continued.

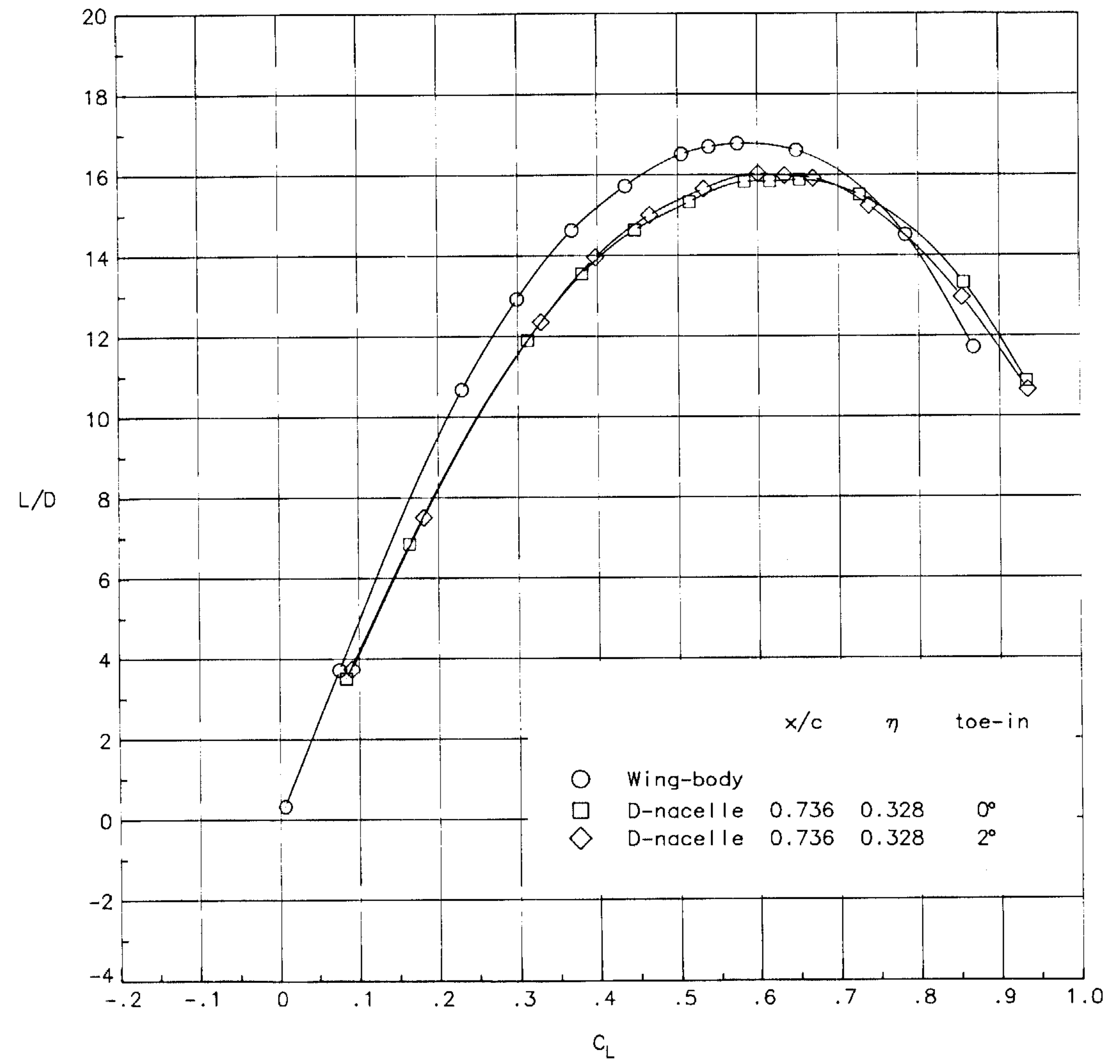

(d) Variation of lift-drag ratio with lift coefficient.

Figure 21. Concluded.

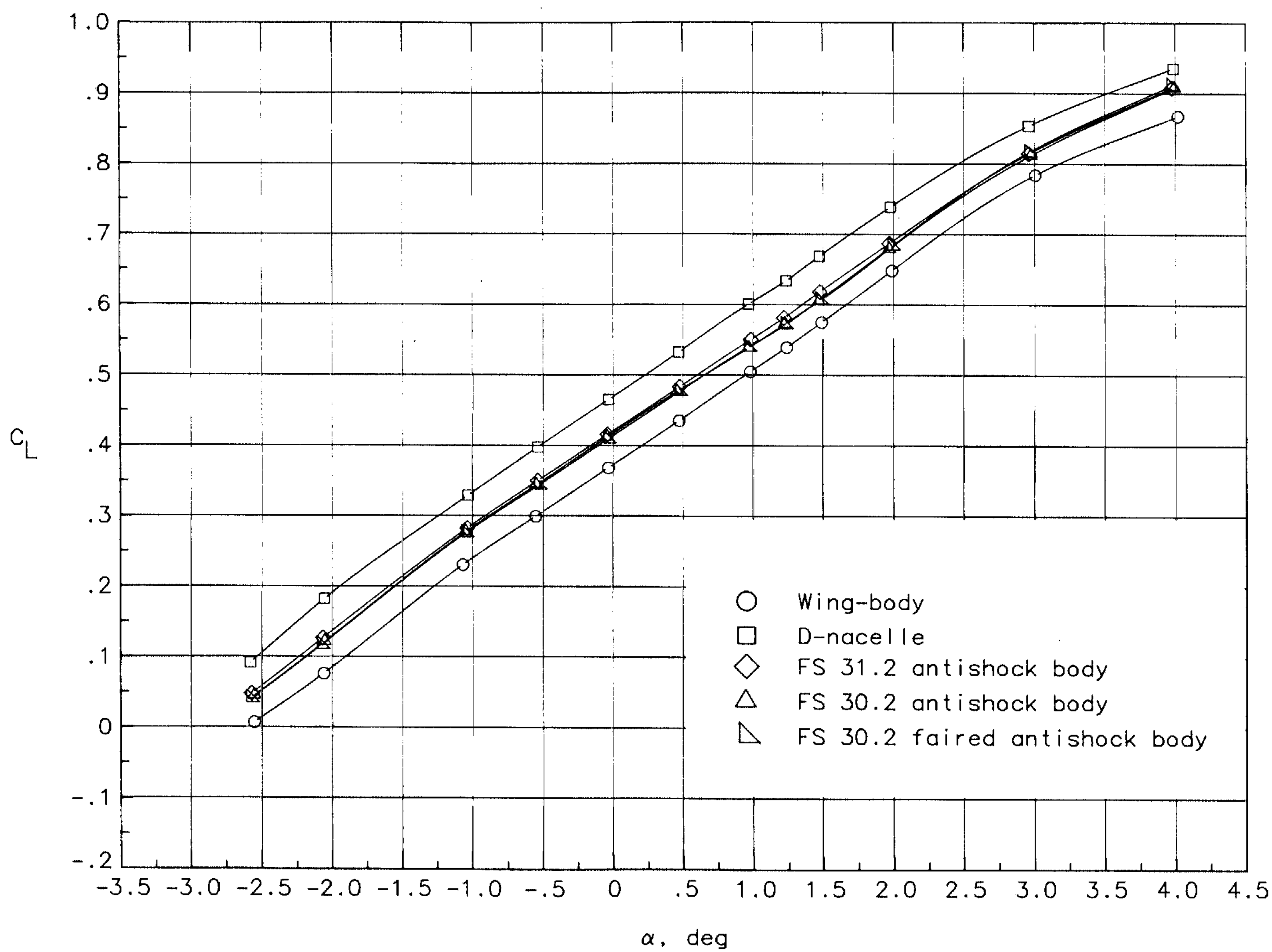

(a) Variation of lift coefficient with angle of attack.

Figure 22. Effect of long-cone antishock bodies mounted on 2° toed-in D-nacelles at $x/c = 0.736$ and $\eta = 0.328$. $M_\infty = 0.80$.

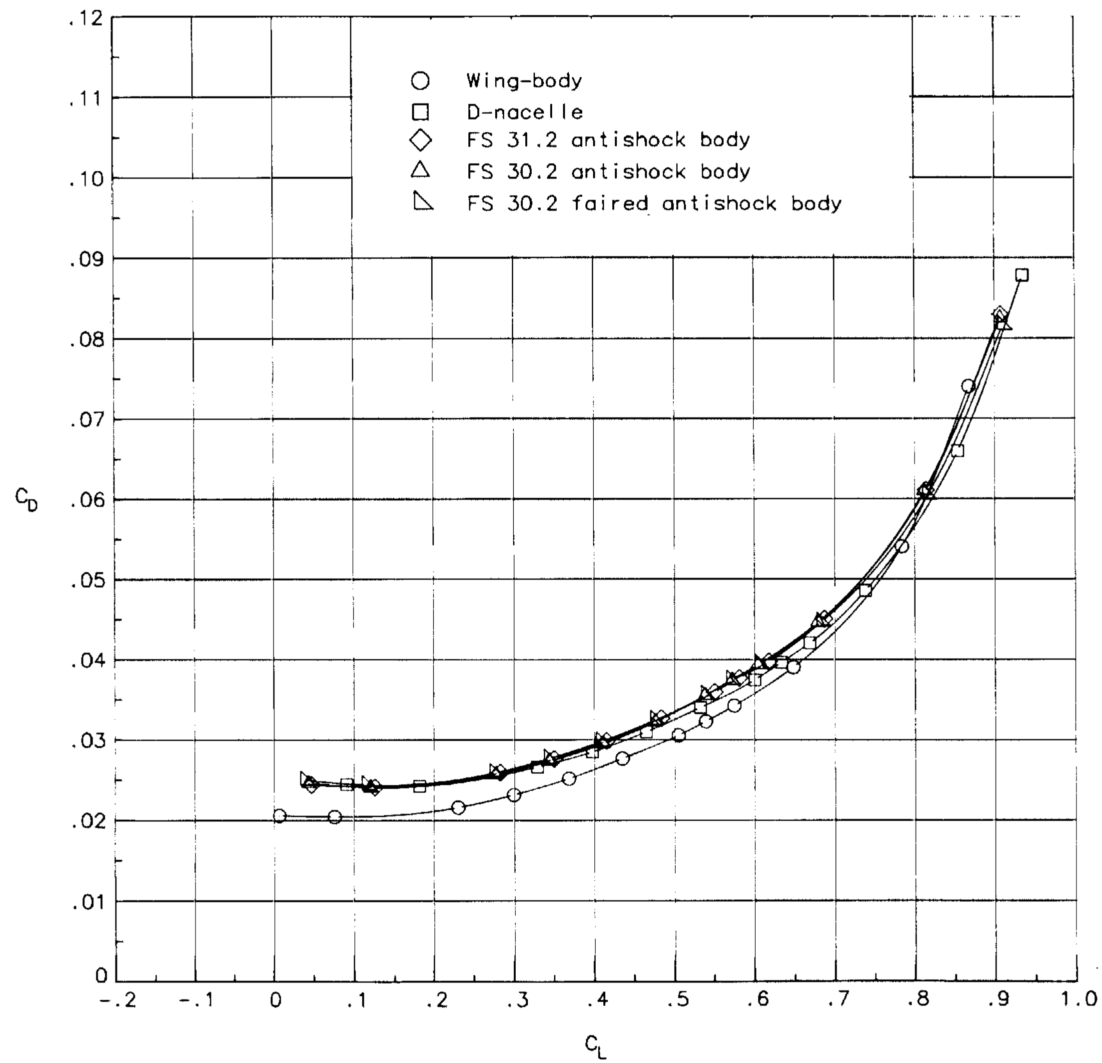

(b) Variation of drag coefficient with lift coefficient.

Figure 22. Continued.

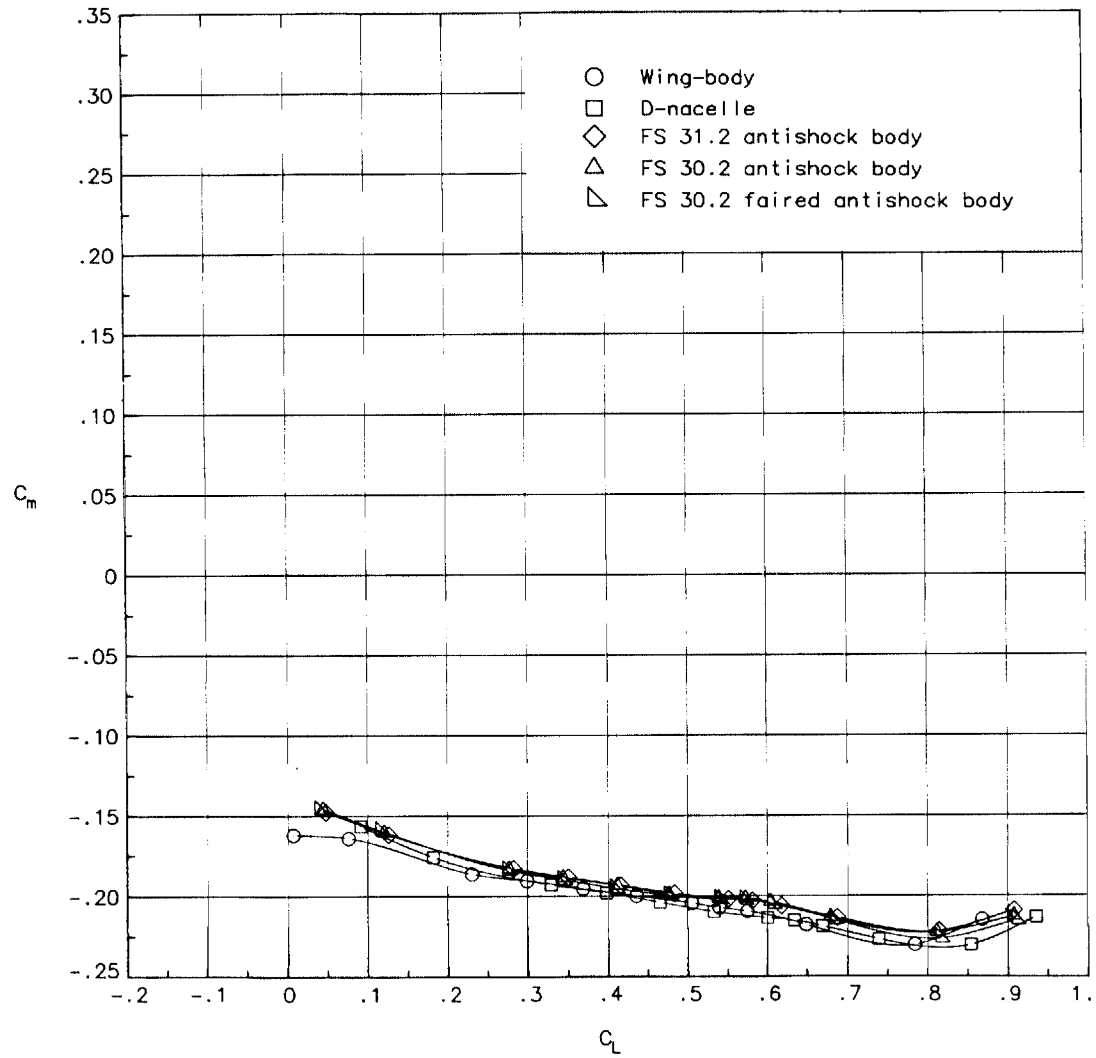

(c) Variation of pitching-moment coefficient with lift coefficient.

Figure 22. Continued.

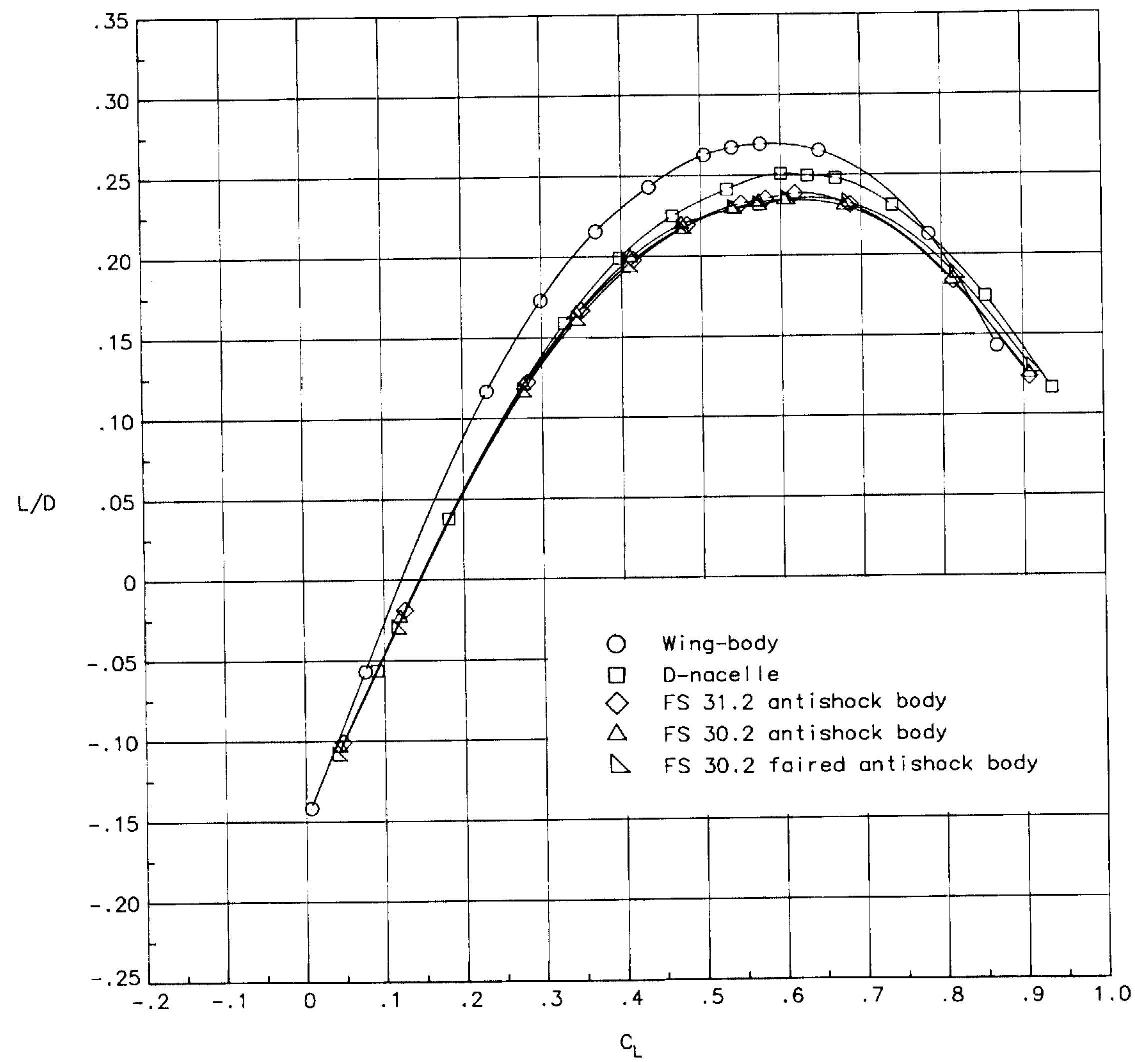

(d) Variation of lift-drag ratio with lift coefficient.

Figure 22. Concluded.

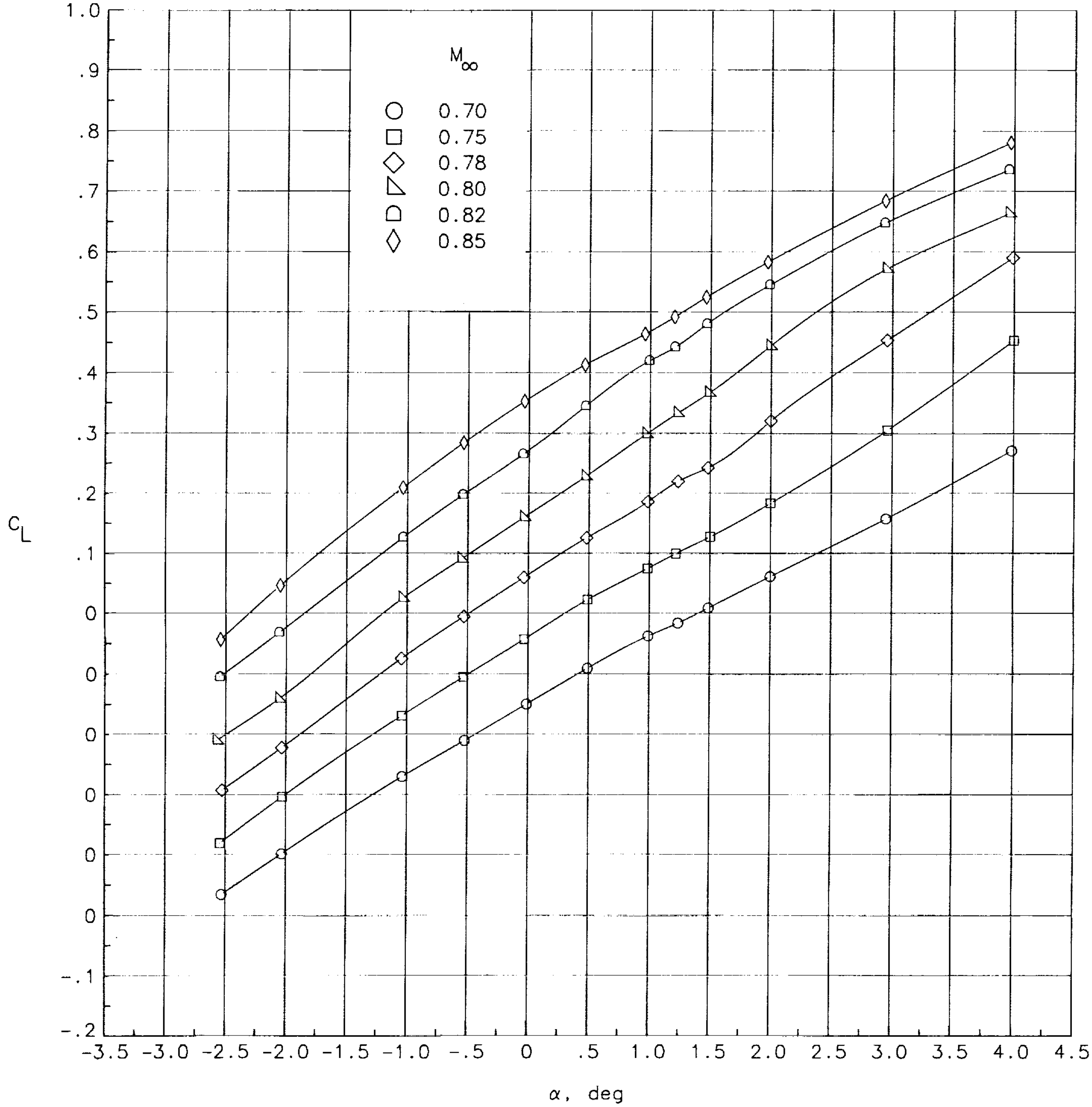

(a) Variation of lift coefficient with angle of attack.

Figure 23. Longitudinal aerodynamic characteristics for wing-body configuration (second wind-tunnel entry).

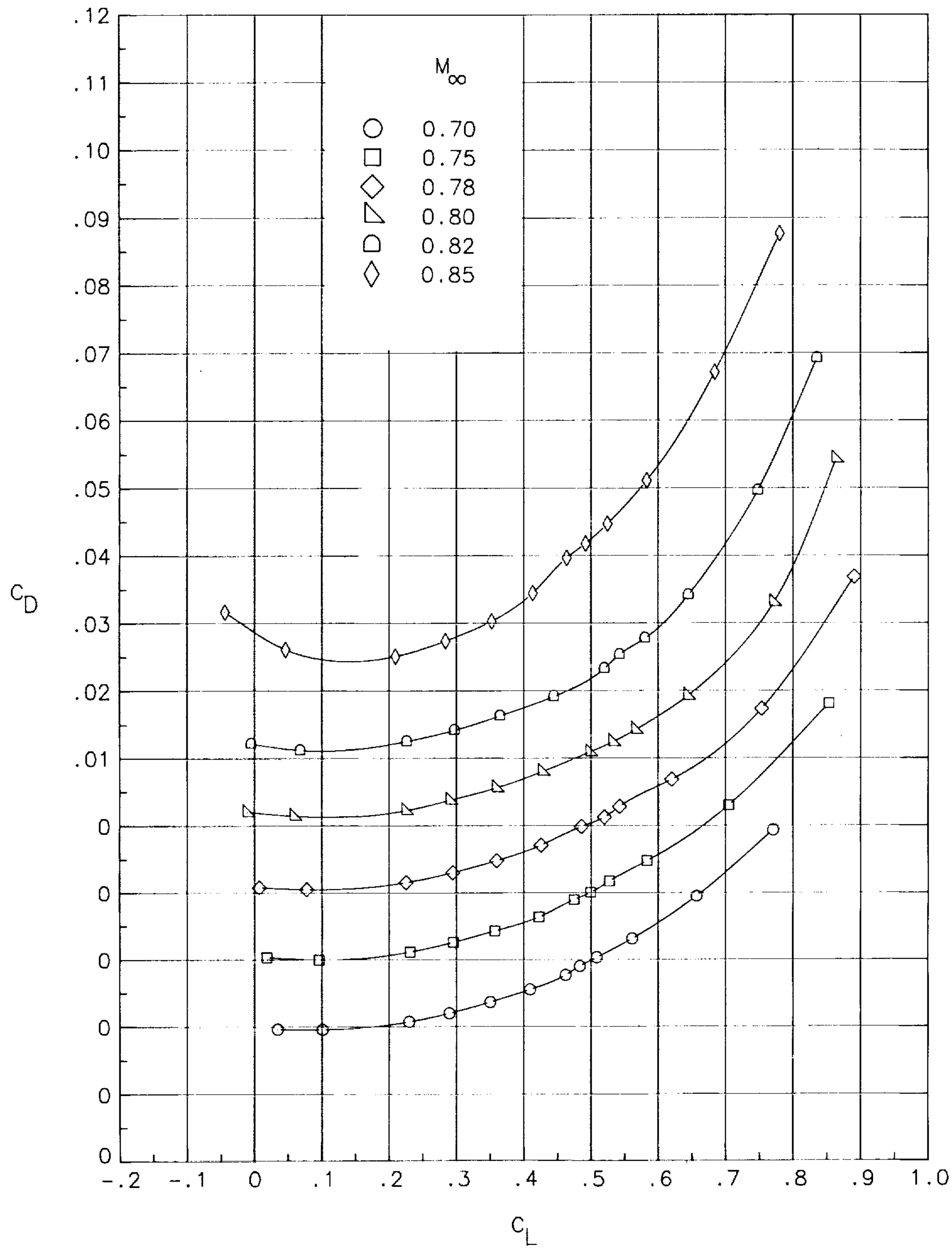

(b) Variation of drag coefficient with lift coefficient.

Figure 23. Continued.

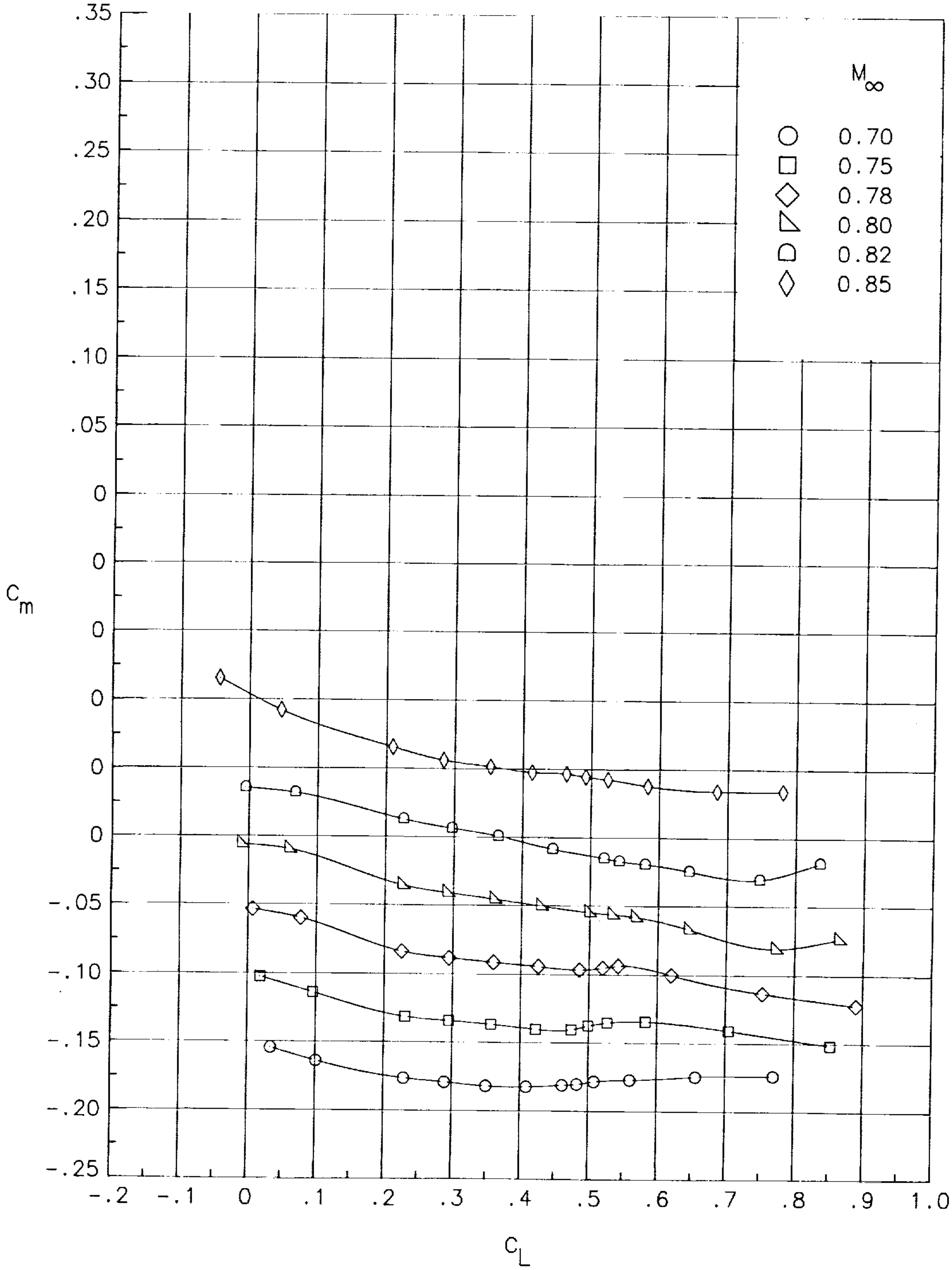

(c) Variation of pitching-moment coefficient with lift coefficient.

Figure 23. Continued.

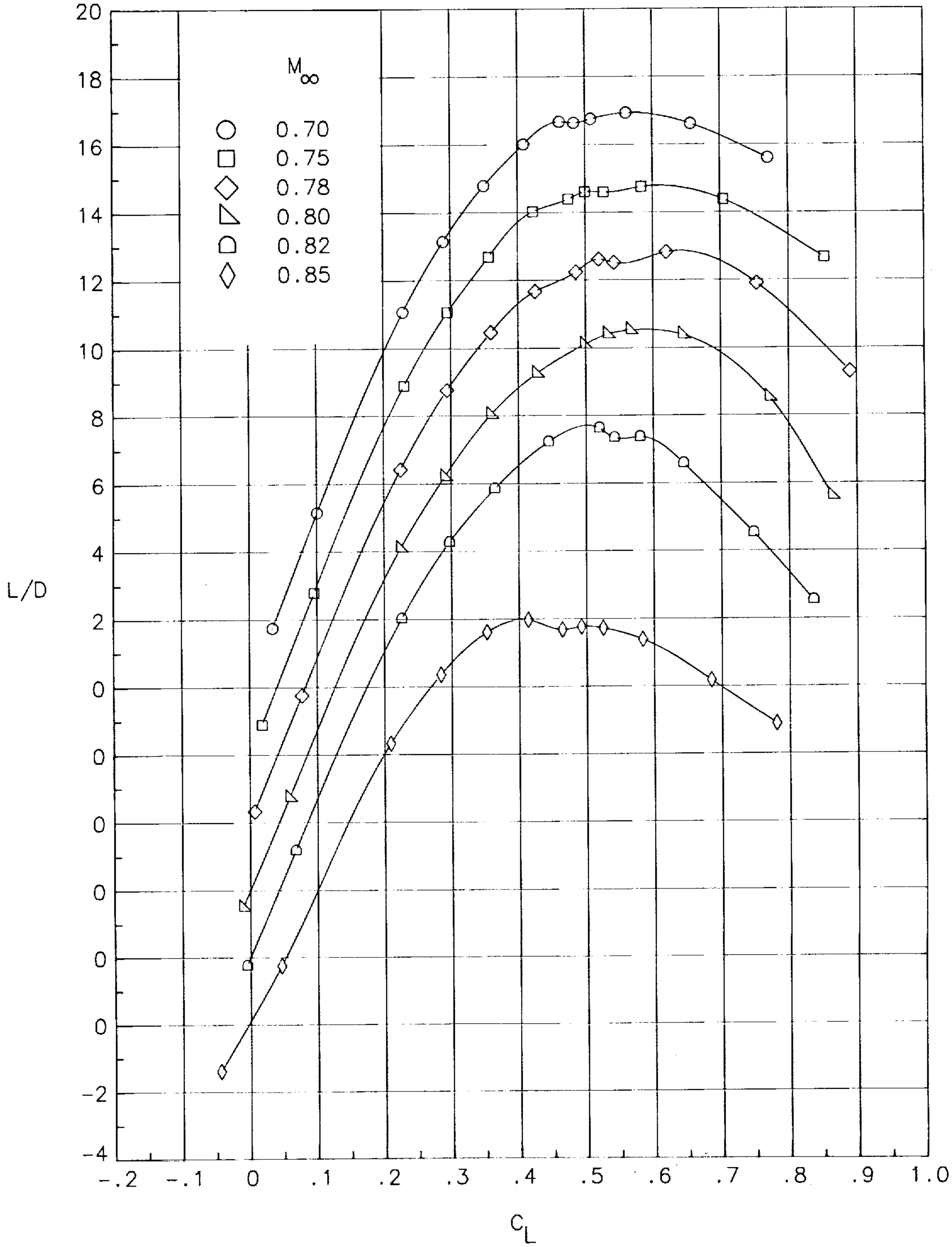

(d) Variation of lift-drag ratio with lift coefficient.

Figure 23. Concluded.

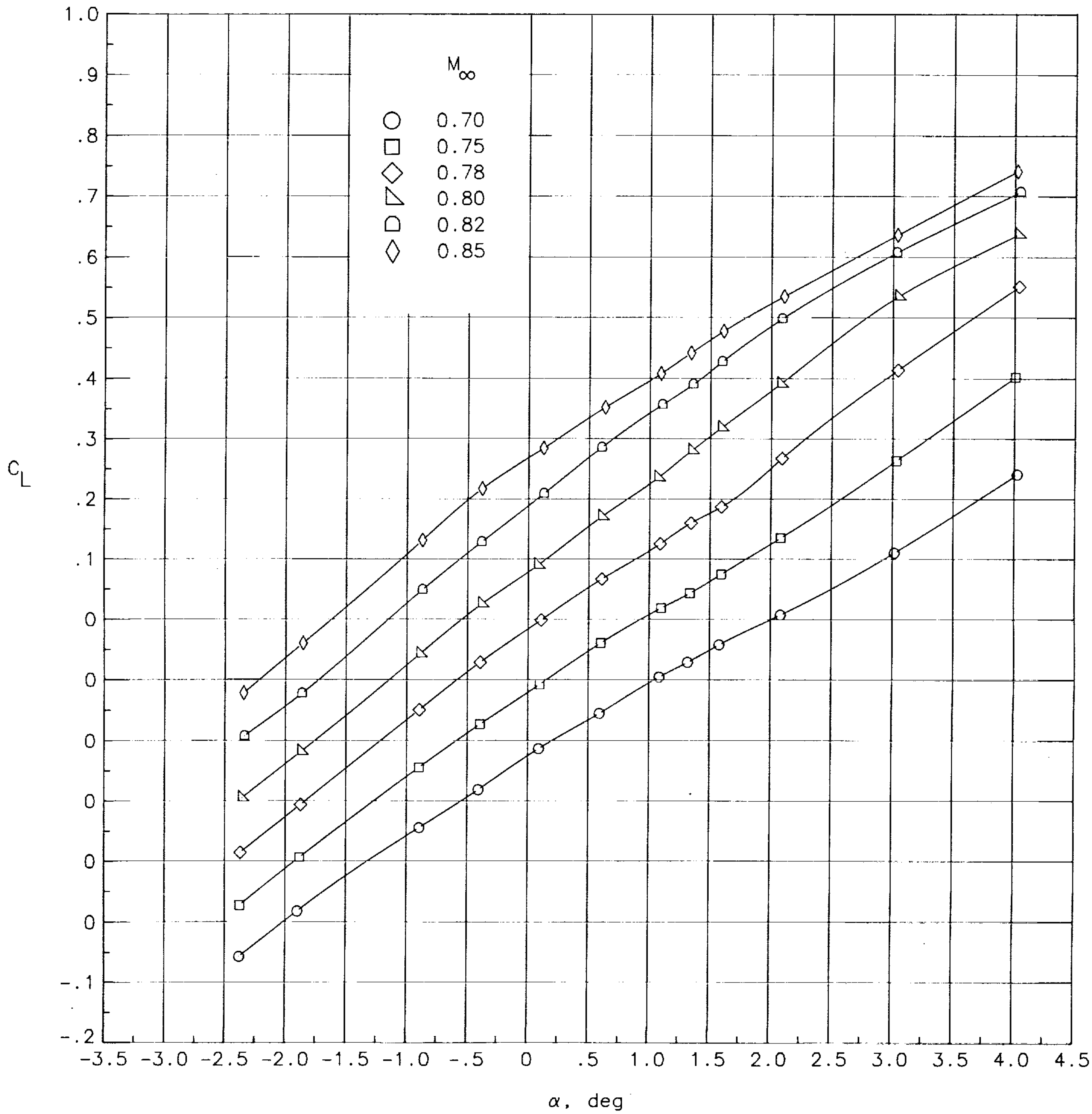

(a) Variation of lift coefficient with angle of attack.

Figure 24. Longitudinal aerodynamic characteristics for wing-body/T-tail configuration (second wind-tunnel entry).

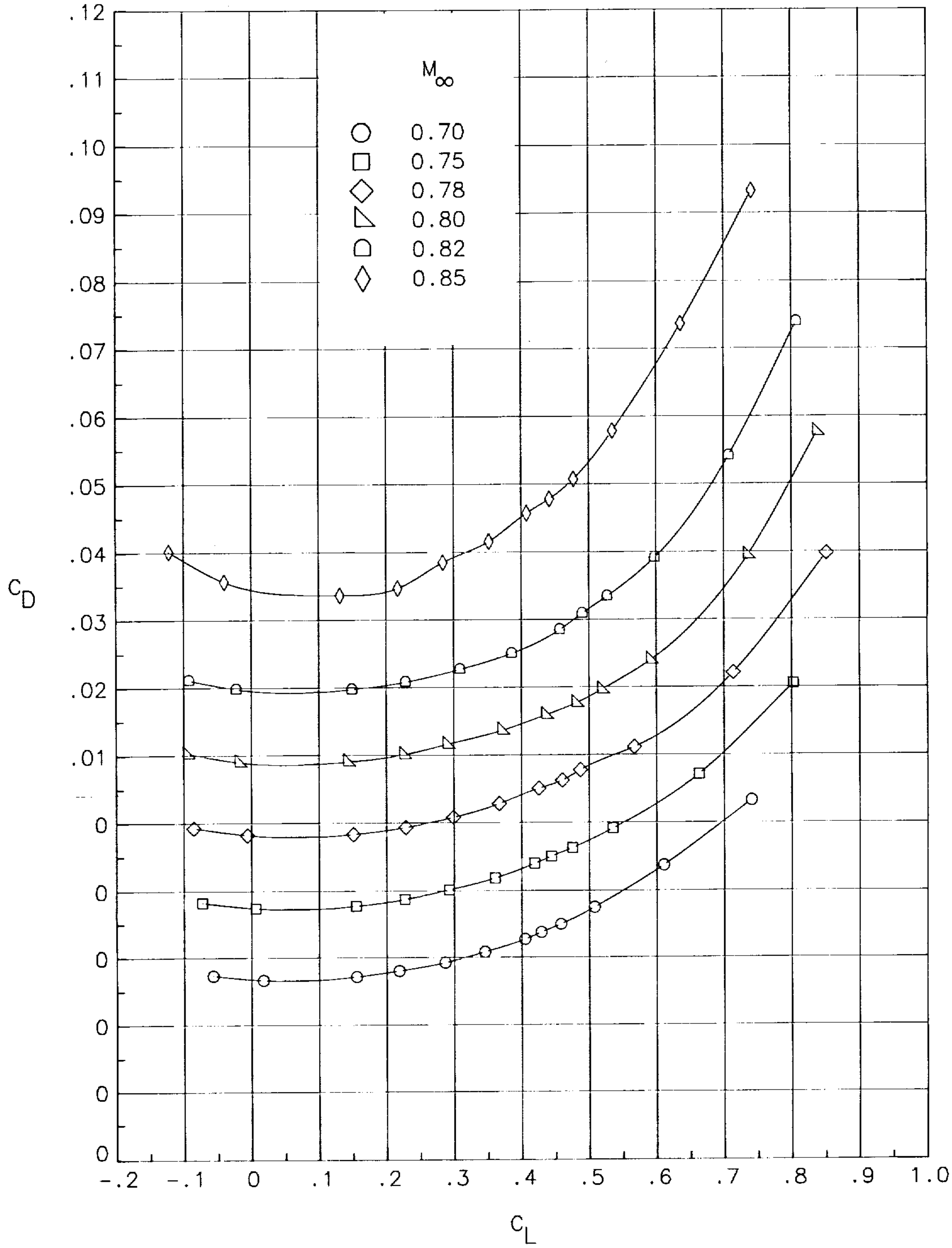

(b) Variation of drag coefficient with lift coefficient.

Figure 24. Continued.

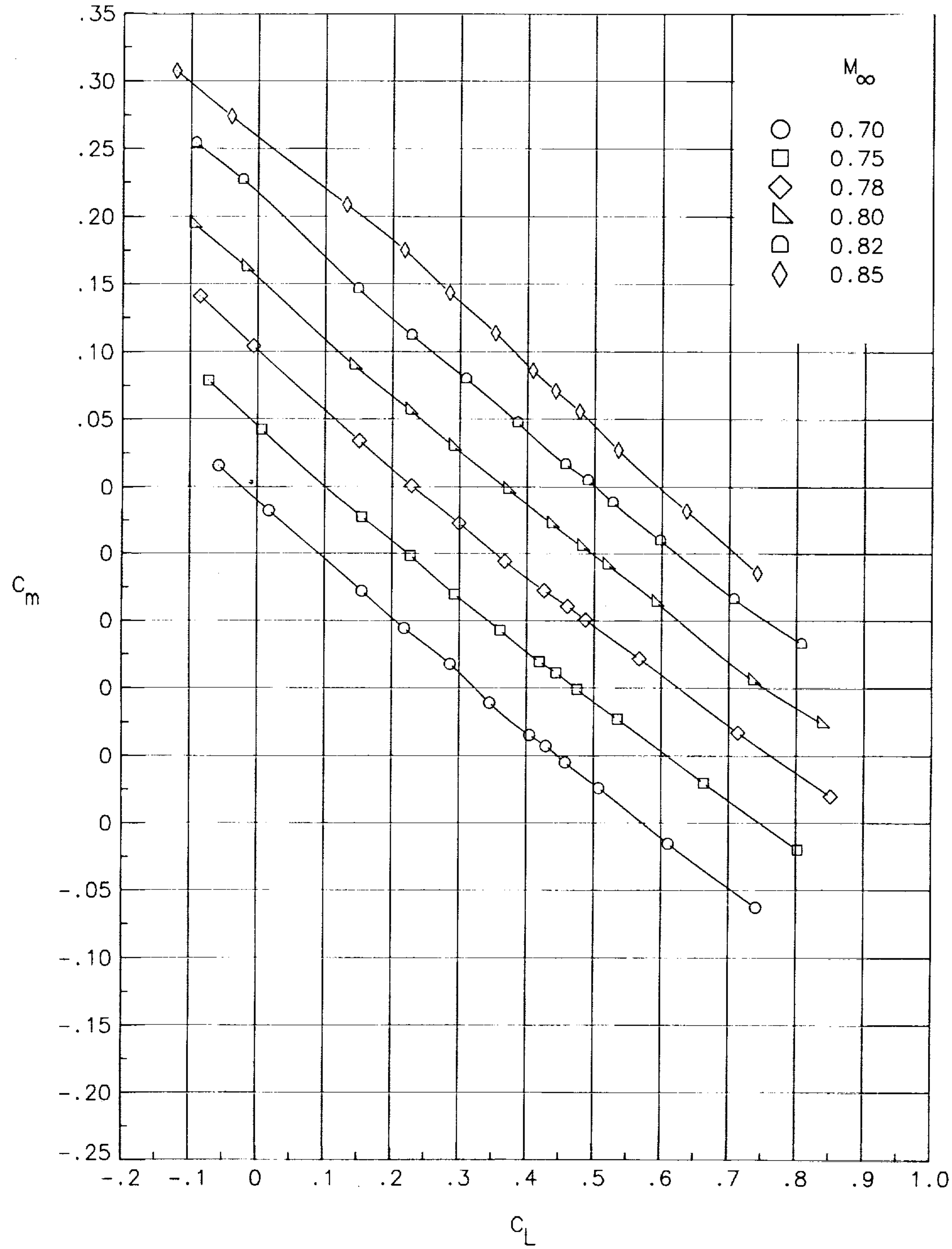

(c) Variation of pitching-moment coefficient with lift coefficient.

Figure 24. Continued.

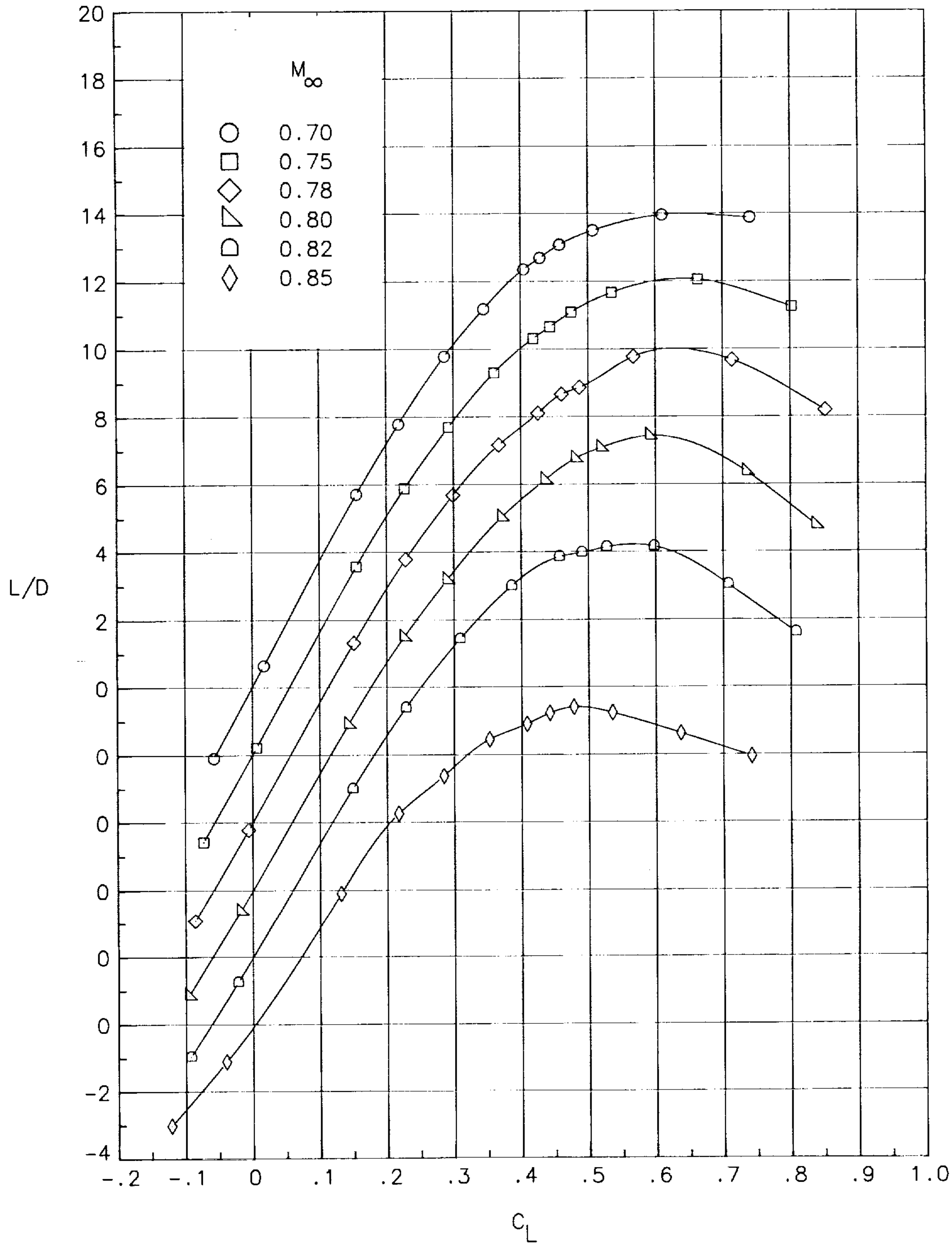

(d) Variation of lift-drag ratio with lift coefficient.

Figure 24. Concluded.

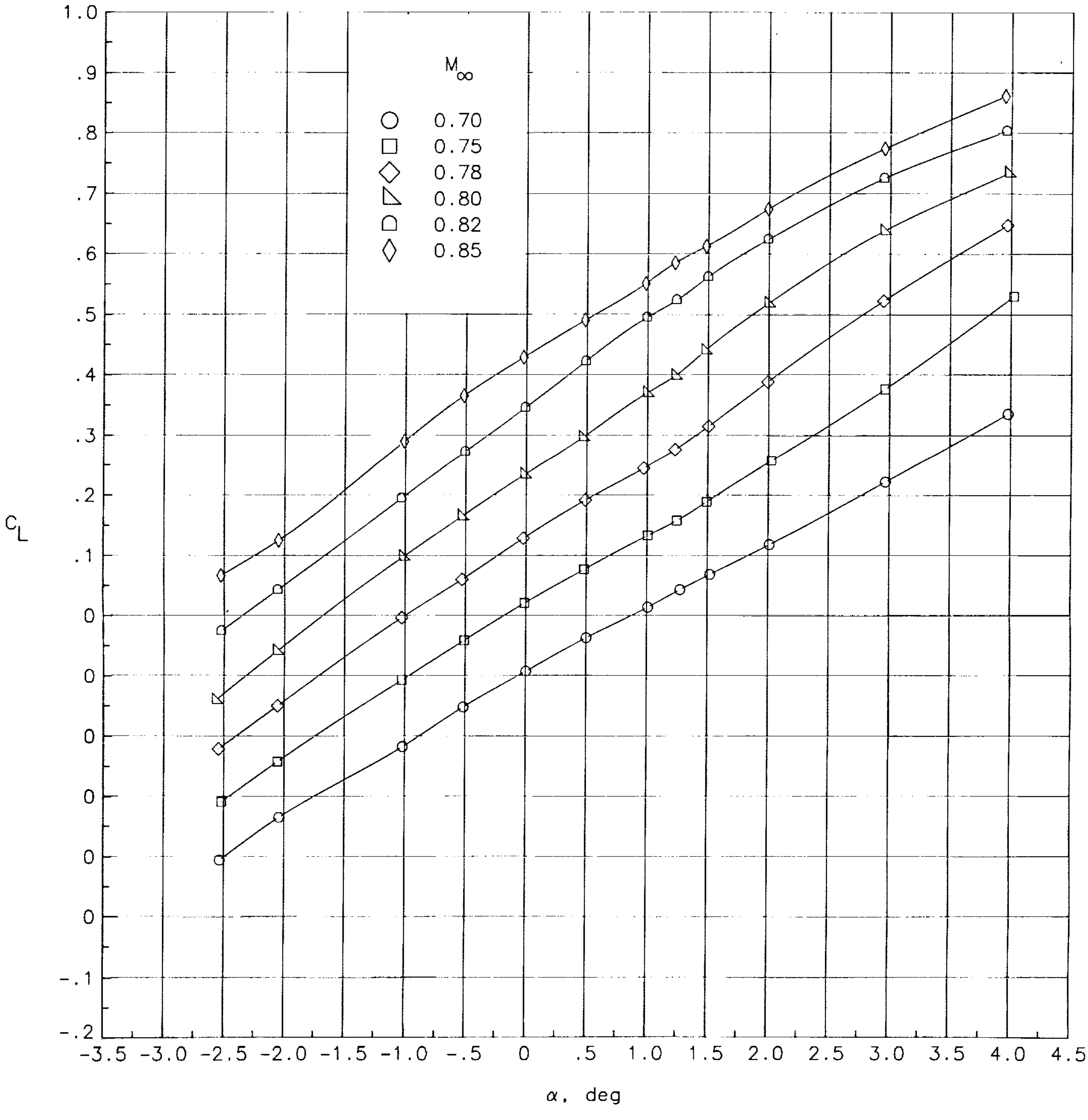

(a) Variation of lift coefficient with angle of attack.

Figure 25. Longitudinal aerodynamic characteristics for wing-body configuration with D-nacelles at $x/c = 0.714$ and $\eta = 0.370$ (second wind-tunnel entry).

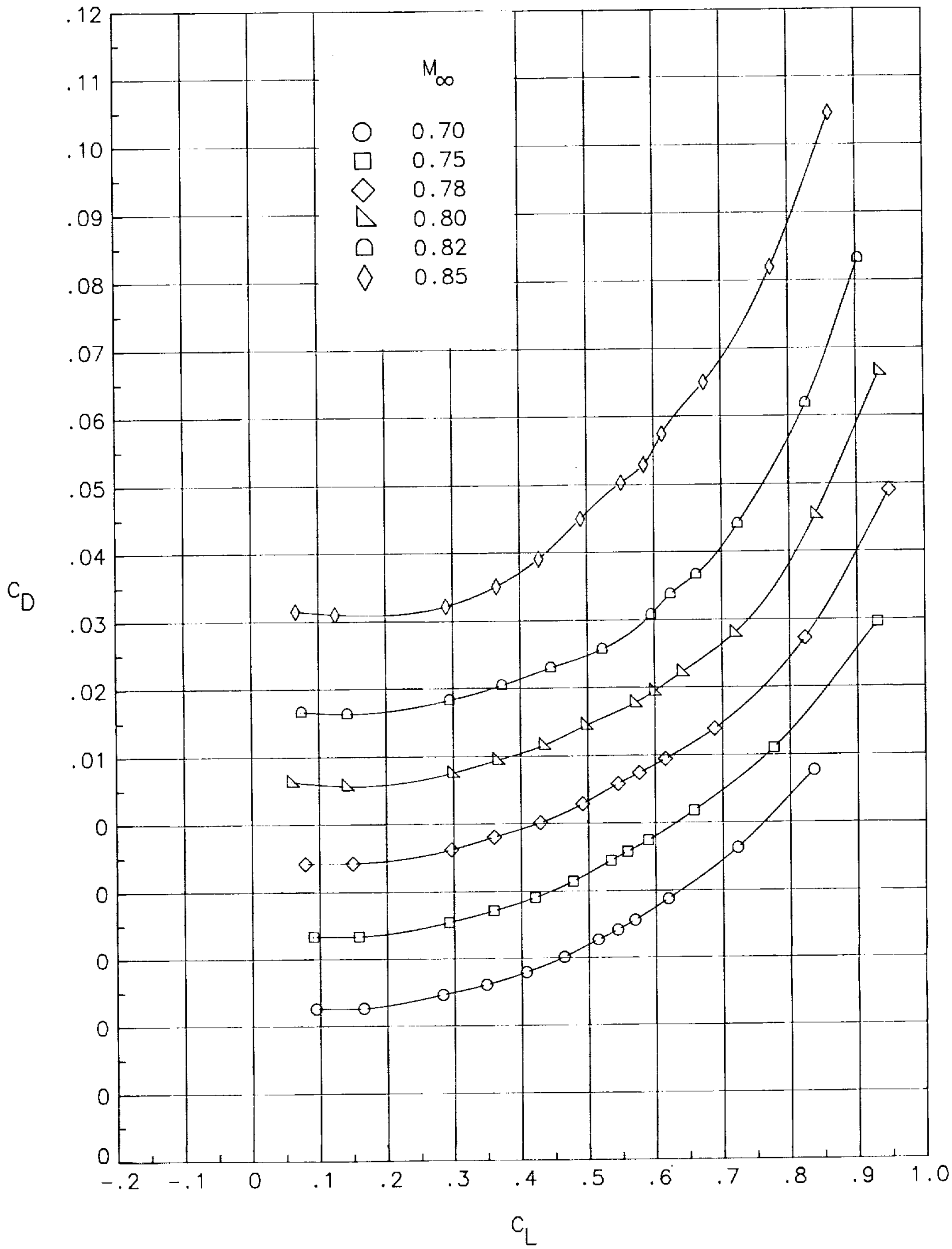

(b) Variation of drag coefficient with lift coefficient.

Figure 25. Continued.

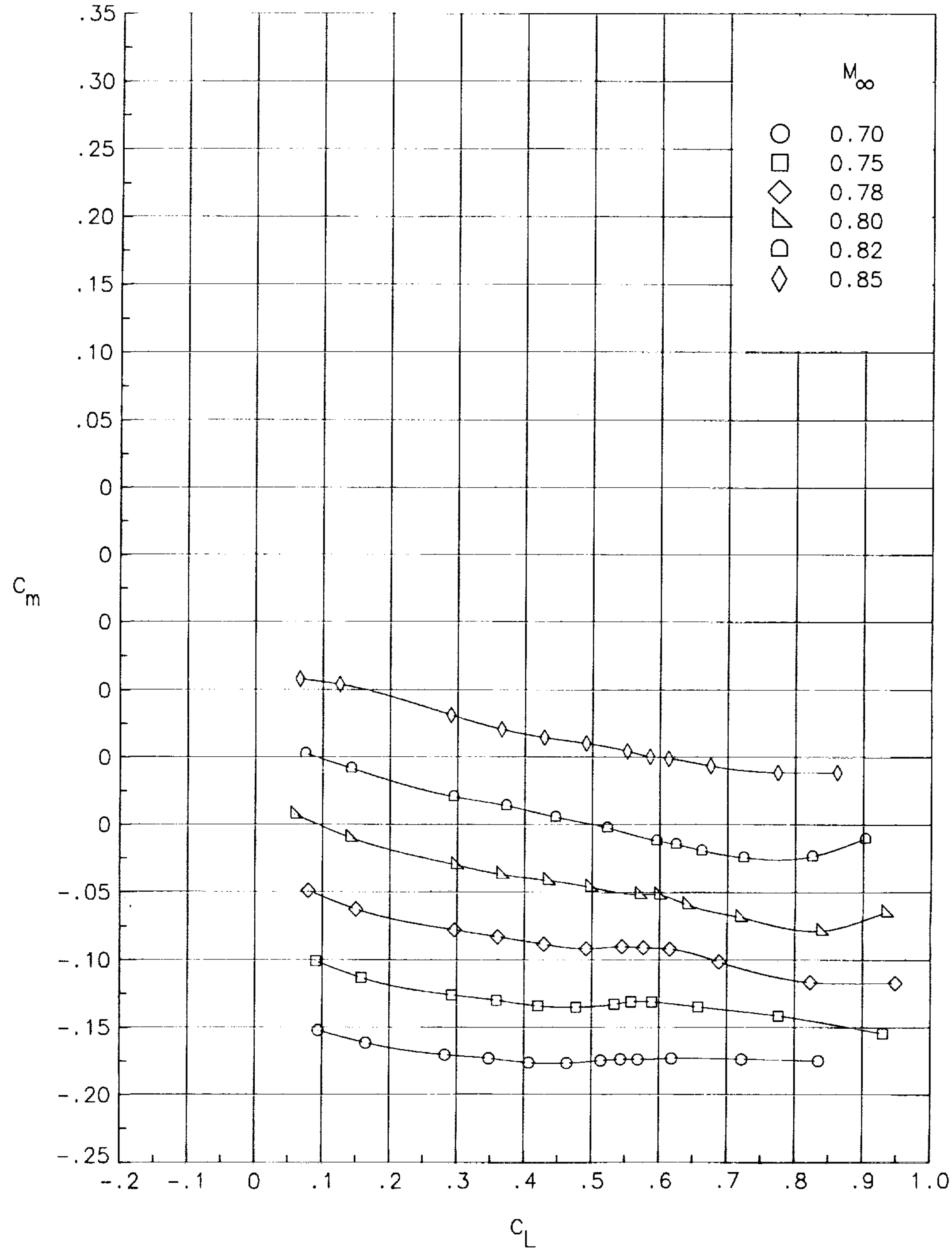

(c) Variation of pitching-moment coefficient with lift coefficient.

Figure 25. Continued.

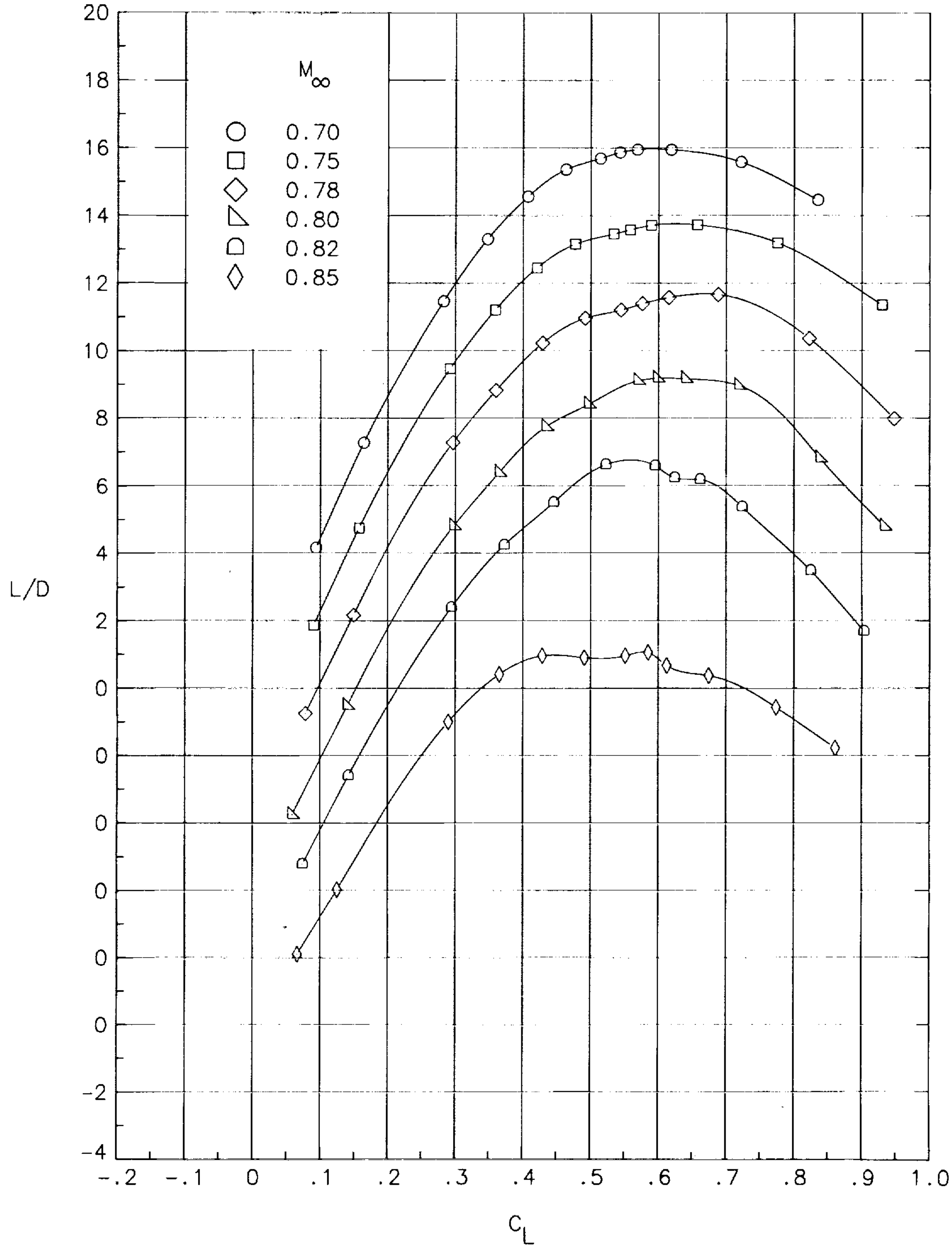

(d) Variation of lift-drag ratio with lift coefficient.

Figure 25. Concluded.

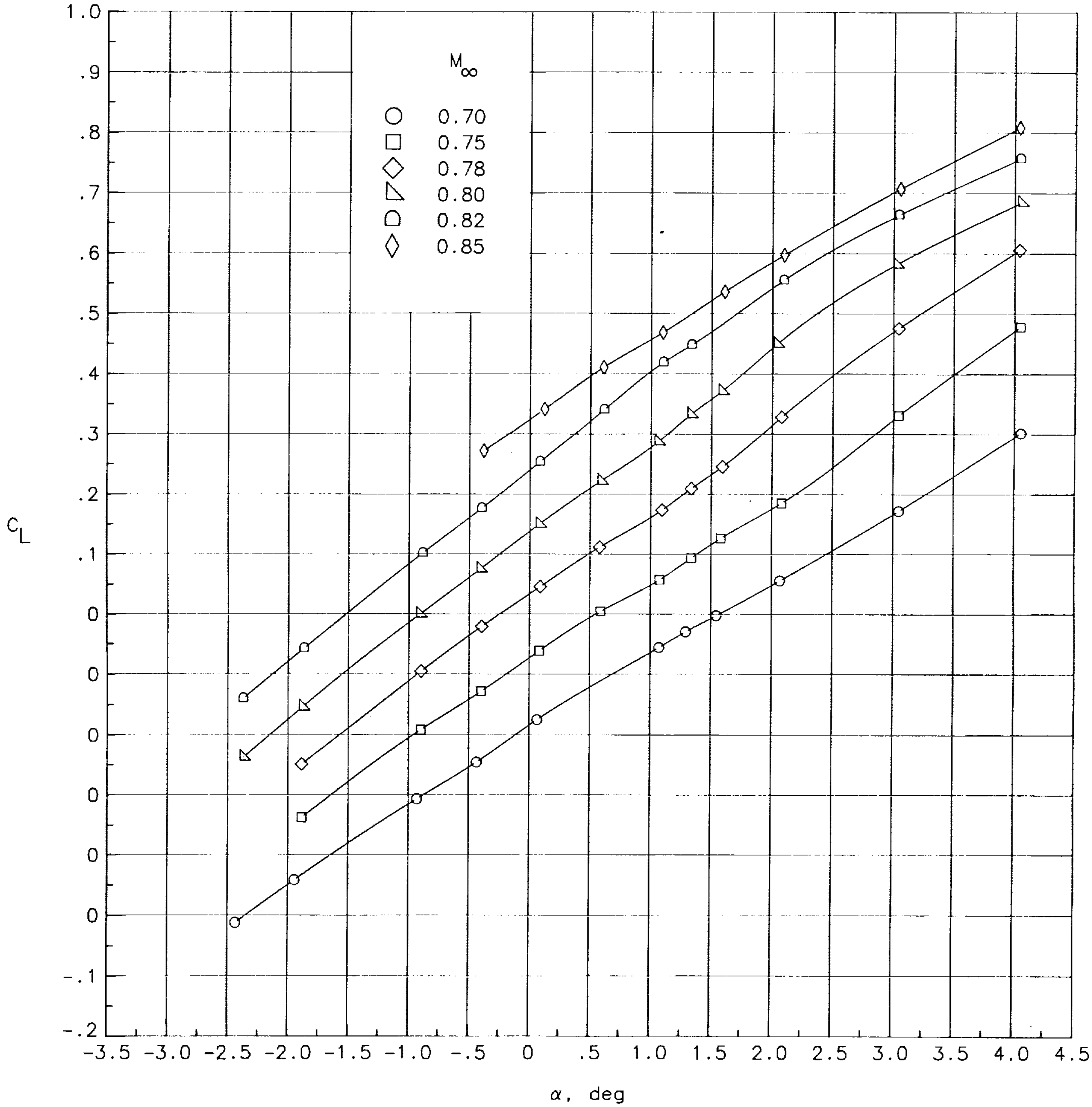

(a) Variation of lift coefficient with angle of attack.

Figure 26. Longitudinal aerodynamic characteristics for wing-body/T-tail configuration with D-nacelles at $x/c = 0.714$ and $\eta = 0.370$ (second wind-tunnel entry).

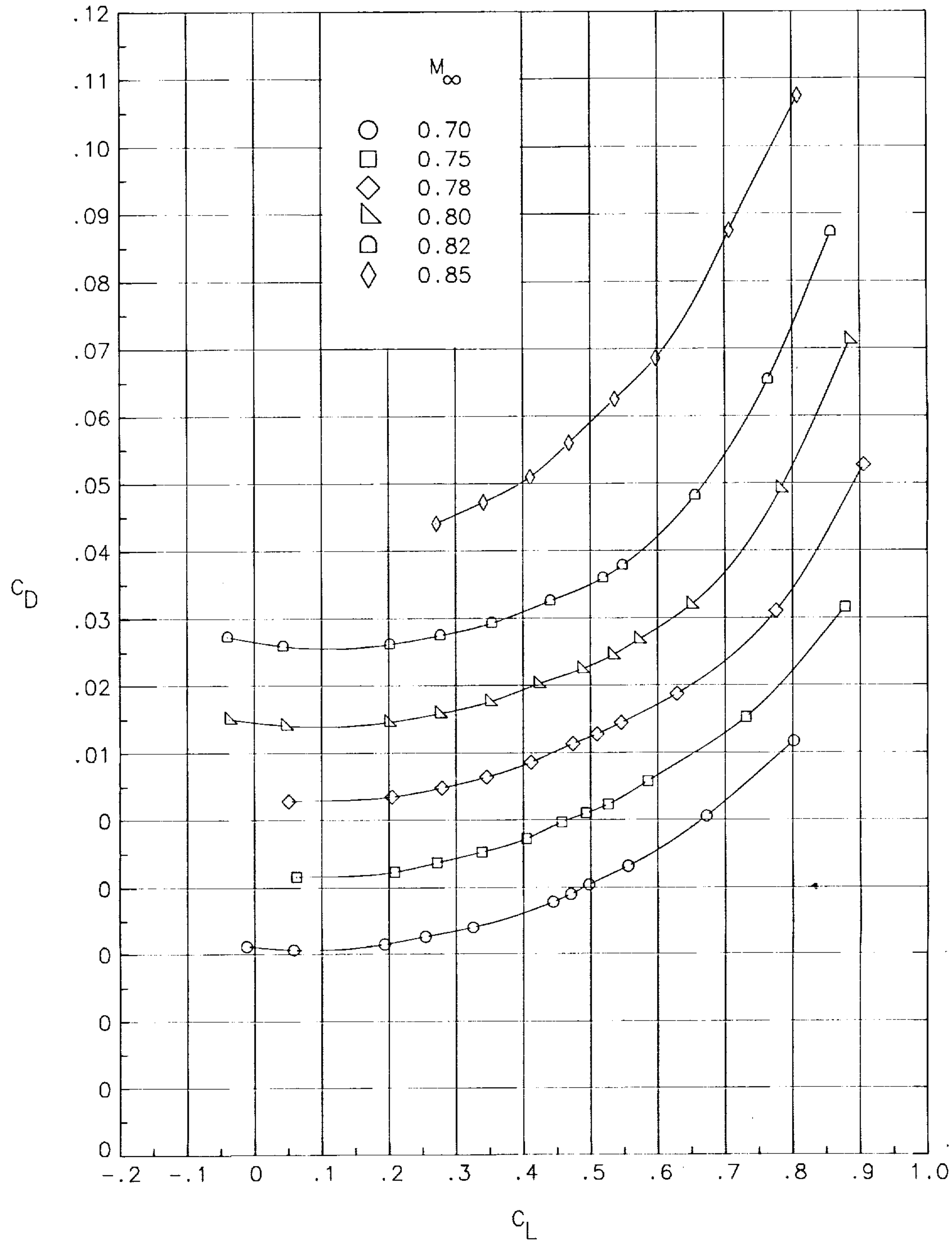

(b) Variation of drag coefficient with lift coefficient.

Figure 26. Continued.

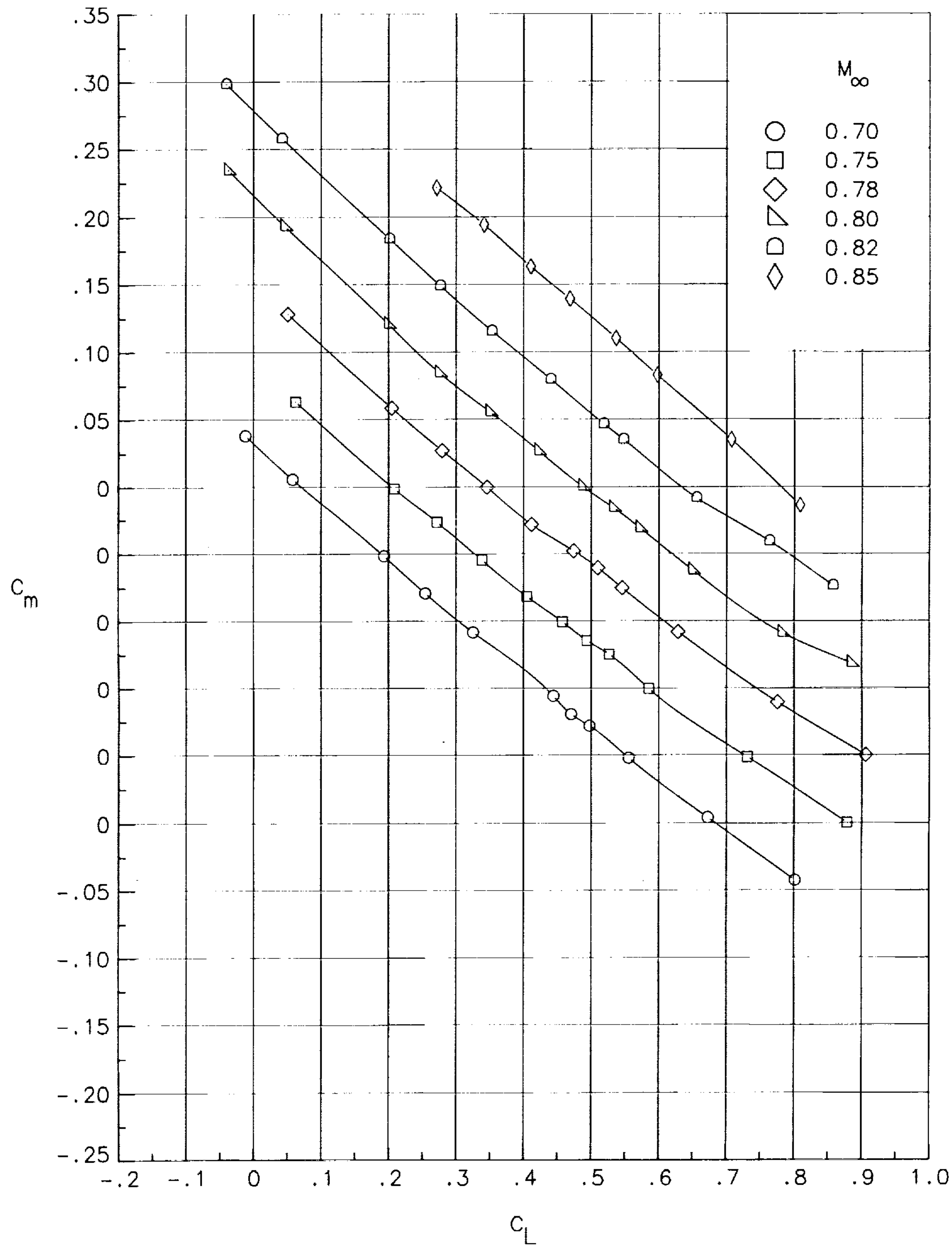

(c) Variation of pitching-moment coefficient with lift coefficient.

Figure 26. Continued.

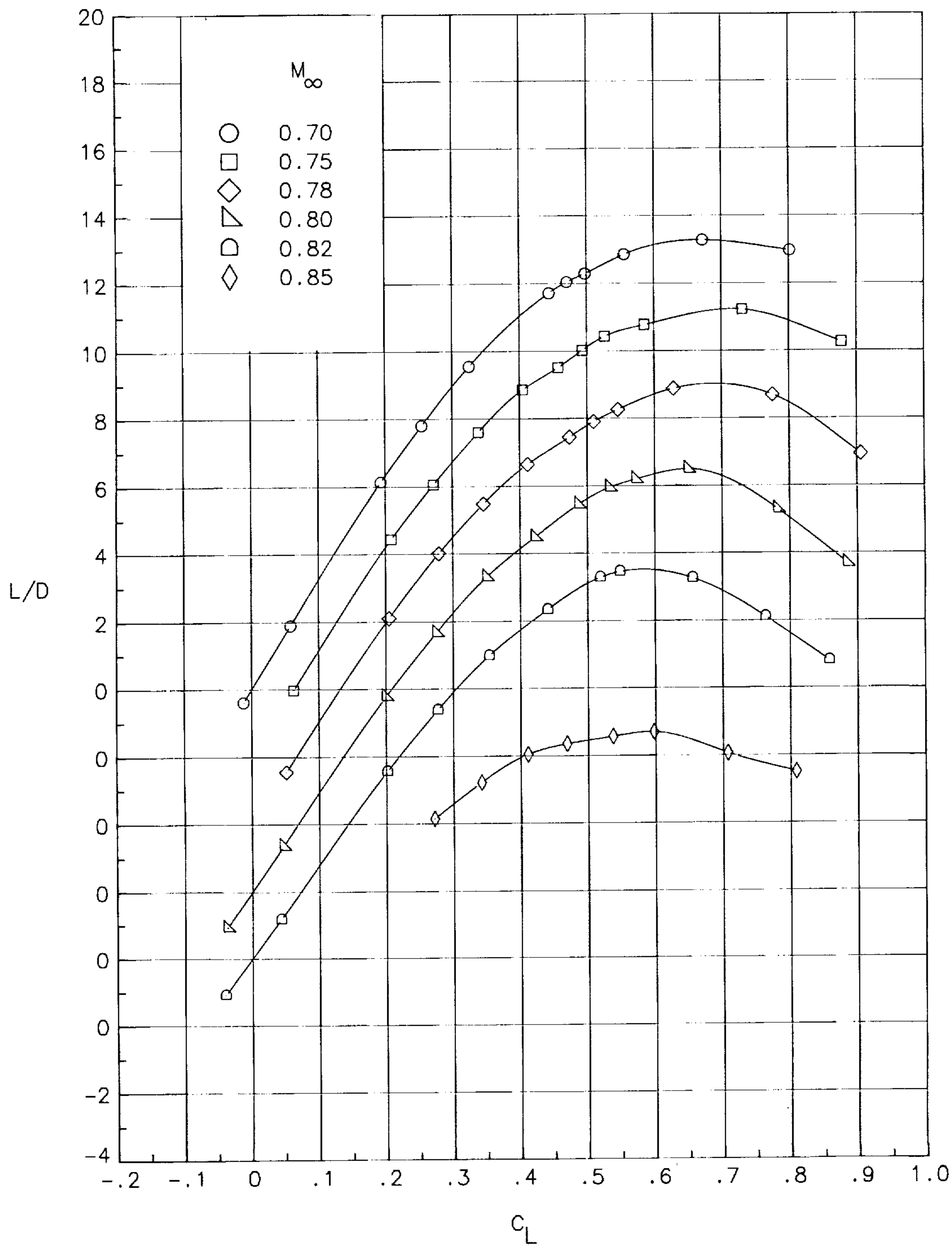

(d) Variation of lift-drag ratio with lift coefficient.

Figure 26. Concluded.

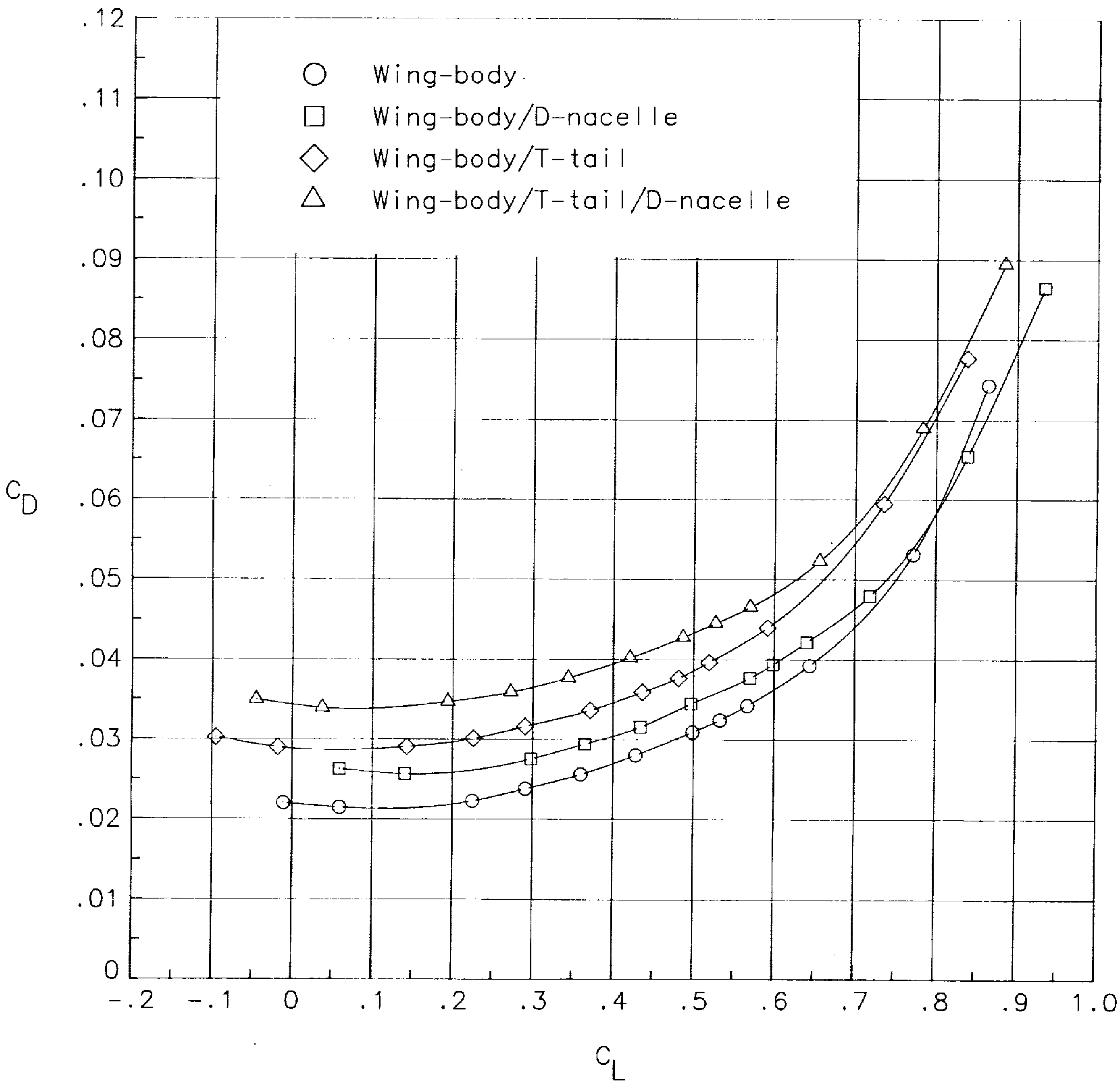

Figure 27. Effect of T-tail on nacelle installation drag coefficient. $M_\infty = 0.80$.

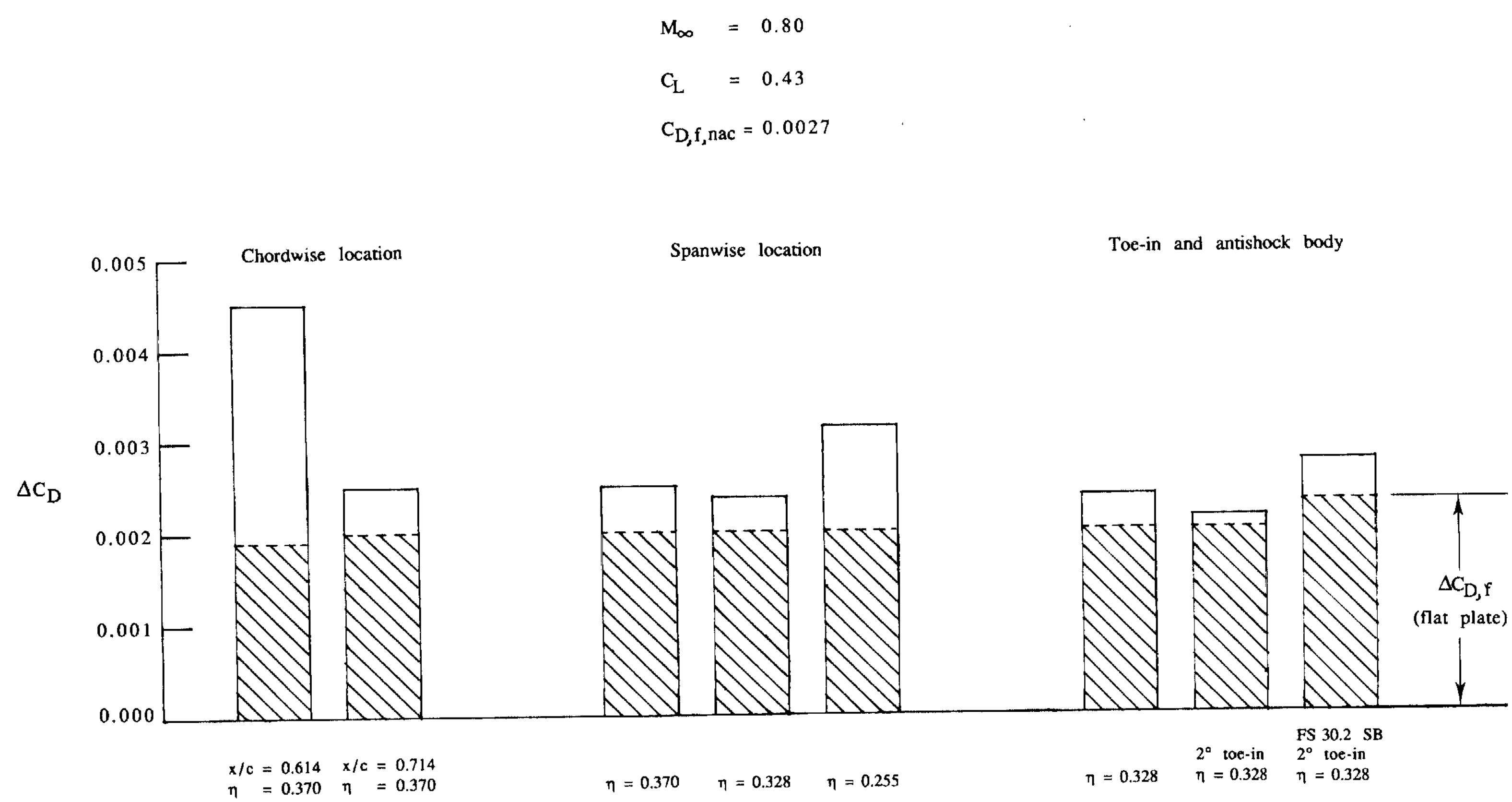

Figure 28. Comparison of installed drag coefficients for various configurations (T-tail not installed).

NASA National Aeronautics and Space Administration

Report Documentation Page

1. Report No.	2. Government Accession No.	3. Recipient's Catalog No.
NASA TP-3047		

4. Title and Subtitle
Effect of Location of Aft-Mounted Nacelles on Longitudinal Aerodynamic Characteristics of a High-Wing Transport Airplane

5. Report Date
December 1990

6. Performing Organization Code

7. Author(s)
William K. Abeyounis and James C. Patterson, Jr.

8. Performing Organization Report No.
L-16743

9. Performing Organization Name and Address
NASA Langley Research Center
Hampton, VA 23665-5225

10. Work Unit No.
505-62-41-05

11. Contract or Grant No.

12. Sponsoring Agency Name and Address
National Aeronautics and Space Administration
Washington, DC 20546-0001

13. Type of Report and Period Covered
Technical Paper

14. Sponsoring Agency Code

15. Supplementary Notes
William K. Abeyounis: Langley Research Center, Hampton, Virginia.
James C. Patterson, Jr.: Vigyan Research Associates, Inc., Hampton, Virginia.

16. Abstract
As part of a propulsion/airframe integration program at Langley Research Center, tests have been conducted in the Langley 16-Foot Transonic Tunnel to determine the longitudinal aerodynamic effects of installing flow-through, mixed-flow engine nacelles at several aft underwing positions on a high-wing transport airplane. Nacelles with D-shaped inlets were used in the tests. Some configurations with antishock bodies and with nacelle toe-in were also tested. Data were obtained for a free-stream Mach number range from 0.70 to 0.85 and for a model angle-of-attack range from −2.5° to 4.0°.

17. Key Words (Suggested by Authors(s))
Propulsion integration
Transport airplane
Wing-body/nacelle interference
D-shaped nacelles
Antishock bodies

18. Distribution Statement
Unclassified—Unlimited

Subject Category 02

19. Security Classif. (of this report)	20. Security Classif. (of this page)	21. No. of Pages	22. Price
Unclassified	Unclassified	96	A05

NASA FORM 1626 OCT 86 NASA-Langley, 1990

For sale by the National Technical Information Service, Springfield, Virginia 22161-2171

96